# CD4$^+$ T cell immunity against cutaneous melanoma encompasses multifaceted MHC II-dependent responses

Emma G. Bawden[1,3,21] , Teagan Wagner[1], Jan Schröder[2], Maike Effern[1,3], Daniel Hinze[3], Lewis Newland[1,3], Grace H. Attrill[4,5,6], Ariane R. Lee[1], Sven Engel[1], David Freestone[1], Marcela de Lima Moreira[1], Elise Gressier[1], Nathan McBain[1], Annabell Bachem[1], Ashraful Haque[1], Ruining Dong[2,7], Angela L Ferguson[5,6,8,9], Jarem J. Edwards[4,5,6], Peter M. Ferguson[4,5,10,11], Richard A. Scolyer[4,5,6,10,11], James S. Wilmott[4,5,6], Christopher M. Jewell[12,13,14,15], Andrew G. Brooks[1], David E Gyorki[16,17], Umaimainthan Palendira[4,5,6], Sammy Bedoui[1], Jason Waithman[18,19], Katharina Hochheiser[1,17], Michael Hölzel[3,20], Thomas Gebhardt[1,20,21]

[1]Department of Microbiology and Immunology, The University of Melbourne at the Peter Doherty Institute for Infection and Immunity, Melbourne, Victoria, Australia.

[2]Computational Sciences Initiative, Department of Microbiology and Immunology, The Peter Doherty Institute for Infection and Immunity, University of Melbourne, Melbourne, Australia.

[3]Institute of Experimental Oncology (IEO), Medical Faculty, University Hospital Bonn, University of Bonn, Bonn 53105, Germany.

[4]Melanoma Institute Australia, The University of Sydney, Sydney, New South Wales, Australia.

[5]Faculty of Medicine and Health, The University of Sydney, Sydney, New South Wales, Australia.

[6]Charles Perkins Centre, The University of Sydney, Sydney, New South Wales, Australia.

[7]Department of Clinical Pathology and Centre for Cancer Research, The University of Melbourne, Melbourne, Victoria, Australia

[8]Centenary Institute, The University of Sydney, Sydney, New South Wales, Australia.

[9]Infection, Immunity and Inflammation theme, School of Medical Sciences, The Charles Perkins Centre, The University of Sydney, Sydney, New South Wales, Australia.

[10]Department of Tissue Oncology and Diagnostic Pathology, Royal Prince Alfred Hospital, Sydney, Australia

[11]NSW Health Pathology, Sydney, Australia

[12]Fischell Department of Bioengineering, University of Maryland; College Park, MD, USA.

[13]United States Department of Veterans Affairs, VA Maryland Health Care System; Baltimore, MD, USA.

[14]Robert E. Fischell Institute for Biomedical Devices; College Park, MD, USA.

[15]Marlene and Stewart Greenebaum Cancer Center; Baltimore, MD, USA.

[16]Division of Cancer Surgery, Peter MacCallum Cancer Centre and Sir Peter MacCallum Department of Oncology, University of Melbourne

[17]Peter MacCallum Cancer Centre Melbourne, Melbourne, Victoria, Australia.

[18]Telethon Kids Institute, University of Western Australia, Perth, Western Australia, Australia.

[19]School of Biomedical Sciences, University of Western Australia, Perth, Western Australia, Australia.

[20]Co-senior authors

[21]Corresponding authors: gebhardt@unimelb.edu.au or emma.bawden@unimelb.edu.au

## Abstract

While CD4$^+$ T cells conventionally mediate anti-tumour immunity by providing help to CD8$^+$ T cells, recent clinical studies have implied an important role for cytotoxic CD4$^+$ T cells in cancer immunity. Using an orthotopic melanoma model, we provide a detailed account of antitumoural CD4$^+$ T cell responses and their regulation by MHC II in skin. Intravital imaging revealed prominent interactions of CD4$^+$ T cells with tumour debris-laden MHC II$^+$ host antigen-presenting cells (APCs) that accumulated around tumour cell nests, although direct recognition of MHC II$^+$ melanoma cells alone could also promote CD4$^+$ T cell control. CD4$^+$ T cells stably suppressed or eradicated tumours even in the absence of other lymphocytes by employing TNFα and Fas ligand (FasL), but not perforin-mediated cytotoxicity. IFNɣ was critical for protection, acting both directly on melanoma cells and via induction of nitric oxide synthase in myeloid cells. Our results illustrate multifaceted and context-specific aspects of MHC II-dependent CD4$^+$ T cell immunity against cutaneous melanoma, emphasizing modulation of this axis as a potential avenue for immunotherapies.

**One-sentence summary**: Tumour-suppressive CD4$^+$ T cells control melanoma through a multitude of context-specific helper and effector functions.

## Introduction

T cells are key mediators of cancer immunity[1–3], with $CD8^+$ T cells being widely considered the main effectors because they can directly recognise and kill cancer cells. Nevertheless, $CD8^+$ T cells ultimately become dysfunctional or exhausted as a result of chronic antigen stimulation in the tumour microenvironment (TME)[4]. Moreover, resistance to $CD8^+$ T cell attack can arise from cancer immunoediting, which may culminate in loss of tumour antigens, loss of MHC I antigen presentation machinery, or loss of responsiveness to effector cytokines such as IFNɣ and TNFα[5,6]. $CD4^+$ T cells exert antitumoural activities that are both synergistic and complementary to those of $CD8^+$ T cells[7–11]. $CD4^+$ T cells are restricted to MHC II and thus recognise tumour antigens that are distinct from those targeted by MHC I-restricted $CD8^+$ T cells[12]. Notably, MHC II genotypes exert a profound impact on the mutational landscapes of evolving tumours such that driver mutations are commonly selected for inefficient presentation on MHC II[13], thus corroborating the clinical significance of MHC II-dependent $CD4^+$ T cell immunity in cancer.

$CD4^+$ T cell responses to cancer encompass both tumour-promoting regulatory cells ($T_{REG}$), as well as subsets of antitumoural helper and effector cells[14,15]. Antitumoural $CD4^+$ T cells provide “help” for $CD8^+$ T cell priming in the lymphoid tissues[10,16,17], as well as promote $CD8^+$ T cell recruitment[10,18] and effector function in the TME through the provision of cytokines[19–22] and reprogramming of intratumoural dendritic cells (DCs)[23]. $CD4^+$ T cells in the TME can also recruit and activate myeloid cells, leading to the production of tumouricidal mediators such as reactive oxygen species and nitric oxide (NO)[8,24–27]. Moreover, $CD4^+$ T cells transferred into tumour-bearing lymphopenic mice[28,29] and subsets of $CD4^+$ T cells in cancer patients, including melanoma-specific cells[14,15,30], express classical cytotoxic mediators such as perforin and granzymes[31–33]. Murine and human $CD4^+$ T cells are capable of directly killing autologous MHC II-expressing cancer cells *in vitro* in a manner is at least partially dependent on MHC II and the perforin-granzyme pathway[30,34,35]. This cytotoxic activity is enhanced by anti-CTLA-4 immunotherapy[35,36] and likely contributes to clinical remission after adoptive cellular therapy (ACT)[37–39]. Indeed, a recent transcriptional analysis demonstrated that a cytotoxic $CD4^+$ T cell gene signature in bladder cancer predicts response to neoadjuvant anti-PD-L1 immunotherapy[34]. Nevertheless, the mechanisms by which $CD4^+$ T cells contribute to tumour killing *in vivo* remain unclear and the functional consequences of MHC II-dependent $CD4^+$ T cell activation by cancer cells versus host APCs are incompletely understood[14,40,41].

Given the rapidly increasing appreciation of cytotoxic $CD4^+$ T cell functions in cancer and clinical immunotherapy[32,33], we set out to interrogate antitumoural $CD4^+$ T cell responses using an orthotopic melanoma model in mice[42,43]. Focusing on tumour-suppressive $CD4^+$ T cells, we demonstrate context-specific helper and effector functions, reveal the transcriptional landscape of $CD4^+$ T cells in lymph nodes (LNs) and the TME with single cell resolution, and dissect the functional significance of MHC II expression by melanoma cells and host APCs. We illustrate multifaceted and potent effector activities by $CD4^+$ T cells that promote tumour destruction or long-term suppression in immune-competent and lymphocyte-deficient hosts.

## Results

### ***CD4$^+$ T cells protect against epicutaneous B16.gD melanoma challenge.***

To study CD4$^+$ T cell immunity to melanoma, we employed an epicutaneous (e.c.) inoculation model[42] in conjunction with B16.F10 cells engineered to express the full-length glycoprotein D (gD) from herpes simplex virus (HSV), hereafter referred to as B16.gD. We chose gD as a model neoantigen as it contains an epitope ($gD_{315\text{-}327}$) recognised by TCR-transgenic CD4$^+$ T cells (gDT-II)[44]. Accordingly, gDT-II recognised B16.gD *in vitro*, provided that the latter were precultured with IFNɣ to induce expression of MHC II (Fig.S1a). Coculture with B16.gD, but not ovalbumin-expressing B16.Ova, induced gDT-II production of TNFα and to a lesser degree IFNɣ (Fig.S1b). Similar levels of cytokine production were seen after coculture with *in vitro* generated DCs pulsed with B16.gD lysates (Fig.S1b). Localised transfer of B16.gD onto lightly abraded skin of wildtype (WT) C57BL/6 mice resulted in protracted and variable tumour growth kinetics with reduced incidence of outgrowing tumours compared to subcutaneous inoculation (Fig.1a,b), as described for other B16 lines[43]. Nascent tumours expanded in the dermal layer of skin with involvement of the epidermis from where the B16.gD initially invaded (Fig.S1c). On average ~60% of mice developed progressing tumours, although this was variable between experiments (Fig.1c). The majority of mice with progressing tumours also developed metastases in tumour-draining brachial LNs (Fig.S1d,e).

To test if immune responses to gD impacted melanoma outcomes, we infected mice with HSV-1 on the skin to induce anti-gD immunity and more than 16wks later challenged them with either B16.gD or B16.Ova on ipsilateral flanks. HSV-1-immune mice harbouring gD-specific memory CD4$^+$ T cells[44] were completely protected from tumour outgrowth, whereas age-matched control mice or mice challenged with B16.Ova displayed tumour incidences within the expected range (Fig.1d-f). To address the contribution of CD4$^+$ T cells to gD-specific protection, we enhanced the frequency of melanoma-specific CD4$^+$ T cells in naïve mice by transfer of naïve gDT-II (i.v., $1\times10^4$) prior to challenge with B16.gD (Fig.1g). This resulted in a significant reduction in tumour incidence (Fig.1h,i) and protection from development of metastases in tumour-bearing mice (Fig.S2a). Thus, pre-existing gD-specific immunity in HSV-memory mice, or elevated frequency of gD-specific naive CD4$^+$ T cells, profoundly restrained tumour development in an antigen-dependent manner.

Depletion of CD8$^+$ T cells with anti-CD8α antibody (Ab) partially impaired the protection afforded by gDT-II transfer (Fig.1j). Furthermore, full protection required the ability of gDT-II to infiltrate peripheral tissues as gDT-II.*Fut7*$^{-/-}$, which lack the enzyme fructosyltransferase 7 that is necessary for CD4$^+$ T cell skin migration[45], provided only an intermediate level of protection relative to controls (Fig.1k). Of note, in mice that received gDT-II.*Fut7*$^{-/-}$, LN metastasis was reduced both in frequency and severity compared with non-transferred controls (Fig.S2b), implying that gDT-II were functional and afforded protection in LNs. We also observed impaired resistance to challenge with luciferase-expressing B16.gD (B16.gD.Luc) in mice lacking CD40 (*Cd40*$^{-/-}$, Fig.1l), a key molecule in the functional crosstalk between CD4$^{+}$ T cells with DCs, B cells or myeloid cells[17]. Combined, these results support CD8$^{+}$ T cell-dependent helper functions of gDT-II and further demonstrate a role for tumour-infiltrating gDT-II in localised tumour protection.

### ***Tumour-specific CD4$^{+}$ T cells infiltrate melanoma tumours despite muted priming in LNs.***

To gain more insights into melanoma-specific CD4$^{+}$ T cell responses, we tracked gDT-II using flow cytometry and intravital 2-photon microscopy. Brachial LNs were the major site of CD4$^{+}$ T cell priming early post-inoculation (p.i.) of tumour cells (Fig.S2c,d). Of note, the rate of gDT-II division in LNs of B16.gD-challenged mice was considerably slower compared to mice subjected to skin infection with HSV-1 (Fig.S2d), known to induce strong gDT-II priming[46]. Such signs of relatively muted activation extended to decreased expression levels of activation markers CD44 and the IL-2 receptor α-chain, CD25, in dividing gDT-II from B16.gD-challenged mice (Fig.S2e). Despite this, gDT-II could be detected by flow cytometry in the brachial LN, spleen and tumours at various times p.i., albeit less frequently at later time points in tumour-free mice (Fig.S2f,g). Tumour-bearing mice also had increased numbers of gDT-II in the draining LN compared to tumour-free mice, consistent with an ongoing response to antigen (Fig.S2g).

Intravital 2-photon microscopy confirmed infiltration of GFP-expressing gDT-II into skin inoculated 1wk earlier with B16.gD engineered to express mCherry (B16.gD.*Tyr*$^{KO}$.mCherry). The extent of melanoma cell deposition and gDT-II infiltration was highly variable between mice, often also between distinct regions within an individual inoculation site (Fig.1m-o). This included multiple well-defined tumour cell nests with closely associated gDT-II infiltrates (Fig.1m and Movie S1), partly destroyed and scattered tumour cells in presence of high gDT-II numbers (Fig.1n and Movie S2), or nascent tumours surveyed by a small number of gDT-II (Fig.1o and Movie S3). The latter displayed slow gDT-II movements for more than 2.5h, likely reflecting *in situ* activation[47]. Together, our results show that despite muted priming in LNs, a portion of melanoma-specific CD4$^{+}$ T cells infiltrated skin and tumours where they contributed to tumour immunity.

### ***Diverse transcriptional CD4$^{+}$ T cell states after B16.gD challenge.***

To gain deeper insights into melanoma-specific CD4$^{+}$ T cell differentiation, we used single cell RNA and paired TCR sequencing of CD44$^{hi}$CD4$^{+}$ T cells from LNs, skin inoculation sites and tumours, 8 and 20d p.i. (Fig.2a). CD44$^{lo}$CD4$^{+}$ T cells from naïve LNs served as controls. This revealed 13 clusters distinctly segregated between LNs and periphery (skin inoculation site, tumours) that, according to their expression of key transcription factors, cytokine receptors, effector molecules and migration molecules, reflected several naïve, regulatory, helper and effector differentiation states, as well as one ɣδTCR$^+$ cluster (Fig.2b,c and Fig.S3a,b). Parallel TCR sequencing identified 20 families with identical α/β-chain TCR pairings that each consisted of ≥8 copies. These expanded TCR clones mapped to clusters representing $T_{REG}$, $T_{H}17$, and $T_{FH}$ cells in LNs, as well as $T_{REG}$, $T_{H}17$, $T_{H}1$ and other effector ($T_{EFF}$) cells in skin and tumours, in addition to proliferating cells (Fig.2d,e). Individual TCR clonal families were strongly biased for either $T_{REG}$, $T_{FH}$, mixed $T_{H}17$/proliferating, or $T_{H}1$/$T_{EFF}$ differentiation states (Fig.2e,f). Supporting the assumption that expanded TCR clones represented melanoma-specific cells, the clusters they occupied displayed broad transcriptional evidence for recent activation, including elevated expression of *Cd44*, *Icos*, *Tnfrsf4* (OX40), *Tnfrsf9* (CD137), *Pdcd1* (PD-1), *Maf*, *Cd28* or *Cd69* (Fig.2g and Fig.S3b,c).

$T_{REG}$ clusters in LN and periphery expressed *Foxp3*, *Gata3*, *Prdm1* (Blimp1), *Ikzf2*, *Tox*, *Il2ra* (CD25), as well as *Il10*, *Gzmb*, *Ctla4*, *Havcr2* (Tim3), *Tigit*, *Entpd1* (CD39) alongside *Ccr1*, *Ccr2*, *Ccr3*, and *Itgae* (CD103) (Fig.2h, Fig.S3b,c and Fig.S4). Signature genes of the $T_{FH}$ cluster included *Bcl6*, *Pdcd1*, *Cd160*, *Cxcr5*, *Cd40lg*, *Il4* and *Il21*, whereas $T_{H}17$ clusters in LN and periphery were marked by expression of *Rorc*, *Id2*, *Il17a/f*, *Ccr4, Ccr6*, Cxcr6, *Il1r1*, *Il18r1* and *Il23r* (Fig.2h, Fig.S3b,c and Fig.S4). The peripheral $T_{H}1$ cluster displayed elevated but variable expression of *Ifng*, *Tnf*, *Fasl*, *Cd40lg*, *Nkg7*, *Ccl5*, *Hspa1a/b*, *Jun*, *Id3*, *Il18r1*, *Cxcr3*, *Cxcr6*, and *Itgb1*, many of which they shared with the *Id3*$^{low}$*Bcl6*$^+$ $T_{EFF}$ cluster (Fig.2h, Fig.S3b,c and Fig.S4). A minor portion of these effector cells also variously expressed additional molecules associated with classical cytotoxic activity, including *Gzma*, *Gzmb*, *Gzmk*, and *Slamf7*, whereas *Prf1* expression was rare (Fig.2h and Fig.S4). In summary, our analyses documented diverse CD4$^+$ T cell differentiation states whose expression profiles were consistent with regulatory ($T_{REG}$), helper (e.g. $T_{FH}$) and direct effector activities (e.g. $T_{H}17$, $T_{H}1$, $T_{EFF}$) in response to B16.gD challenge. Furthermore, comparison of cluster-specific gene expression profiles with those reported for CD4$^+$ T cells across a broad range of human tumours[31] revealed enrichment of murine CD4$^+$ T cell gene sets in several, presumably functionally related, human CD4$^+$ T cell clusters (Fig.S5).

### ***Tumour-specific CD4$^+$ T cells directly kill IFNɣ-primed melanoma cells in vitro.***

To probe the functional relevance of CD4$^+$ T cell-expressed effector genes identified in our transcriptional analysis (Fig.2h), we cocultured melanoma cells with *in vitro* activated gDT-II and monitored propidium iodide (PI) uptake (Fig.3a). We observed efficient dose-dependent killing of B16.gD, provided that they were precultured with IFNɣ to induce MHC II expression, as only a modest increase in PI fluorescence was seen without IFNɣ preculture (Fig.3b). The highest number of gDT-II ($5\times10^5$) resulted in almost complete killing of IFNɣ-pretreated B16.gD by 21h, as benchmarked against B16.gD that were treated with paraformaldehyde as a positive control (Fig.3b). We subsequently used an intermediate number of gDT-II ($2.5\times10^5$) to interrogate candidate molecular pathways involved in killing and calculated the level of cell death by normalising PI values in test conditions to those of B16.gD + gDT-II at the assay endpoint (maximal gDT-II killing). Killing of B16.gD was largely MHC II-dependent as shown in assays incorporating MHC II blocking Ab (Fig.3c) or using B16.gD deficient in the master regulator of MHC II expression, CIITA (B16.gD.*Ciita*$^{\mathrm{KO}}$), although modest increases in cell death were also observed under these conditions (Fig.3d and Fig.S6a). In line with this, killing was mostly antigen-specific with only minimal, yet discernible cell death observed for B16.Ova when compared to B16.gD (Fig.3e). Blocking TNF-related apoptosis-inducing ligand (TRAIL, Fig.3f) or IFNɣ (Fig.3g) during the assay had no impact on the killing of B16.gD, although IFNɣ pretreatment of B16.gD may have masked any IFNɣ effects. Perforin-deficient gDT-II (gDT-II.*Prf1*$^{-/-}$) displayed only a minor reduction in killing capacity (Fig.3h). Likewise, blockade of TNFα signalling using B16.gD.*Tnfr1*$^{\mathrm{KO}}$ resulted in only a modest reduction in cell death (Fig.3i), although further reduction in killing was observed when both perforin and TNFα pathways were blocked simultaneously (Fig.3j). Addition of anti-FasL Ab strongly reduced killing (Fig.3k) and almost complete inhibition was achieved by simultaneous interference with TNFα, perforin and FasL (Fig.3l). Thus, gDT-II employ multiple partly redundant effector pathways, predominantly FasL, with additional contributions of TNFα and perforin-dependent pathways, to directly kill melanoma cells *in vitro* (Fig.3m).

### ***Melanoma-intrinsic MHC II expression can activate CD4$^+$ T cell immunity in vivo*.**

Given the pivotal role of MHC II in CD4$^+$ T cell activation, we next sought to interrogate functional consequences of its expression by B16.gD for CD4$^+$ T cell control *in vivo*. Flow cytometric analysis demonstrated that MHC II expression by B16.gD was restricted to small tumours (<70 mm$^3$) and these tumours had higher densities of infiltrating CD4$^+$ T cells (Fig.4a–c). As expected, MHC II expression was low or absent on all B16.gD.*Ciita*$^{\mathrm{KO}}$ and CD4$^+$ T cell infiltration was reduced in these tumours regardless of volume (Fig.4d and Fig.S6b,c). This suggested that MHC II expression by melanoma cells promoted CD4$^+$ T cell accumulation, although tumour development was comparable in mice inoculated with either *Ciita*$^{\mathrm{WT}}$ or *Ciita*$^{\mathrm{KO}}$ B16.gD lines (Fig.S6d).

Next, we tested if MHC II expression by melanoma cells in otherwise MHC II-deficient hosts was sufficient to activate CD4$^+$ T cell immunity. To this end, we inoculated MHC II-deficient *I-Ab*$^{-/-}$ mice with B16.gD.*Ciita*$^{\mathrm{WT}}$ or B16.gD.*Ciita*$^{\mathrm{KO}}$ and 4d later intradermally transferred preactivated gDT-II in proximity to the inoculation site (Fig.4e). This created environments where MHC II-dependent reactivation of gDT-II would be restricted to melanoma cells that upregulated MHC II *in situ* (B16.gD.*Ciita*$^{\mathrm{WT}}$), or where complete lack of MHC II expression in hosts and melanoma cells would preclude MHC II-dependent gDT-II activation (B16.gD.*Ciita*$^{\mathrm{KO}}$). Indeed, we found that gDT-II transfer protected from tumour outgrowth in *I-Ab*$^{-/-}$ mice inoculated with B16.gD.*Ciita*$^{\mathrm{WT}}$ (Fig.4f) but had no impact on control of B16.gD.*Ciita*$^{\mathrm{KO}}$ tumours (Fig.4g). Consistent with this, gDT-II transfer resulted in considerable, yet variable, levels of MHC II expression by B16.gD.*Ciita*$^{\mathrm{WT}}$ (Fig.4h). Reciprocally, a higher portion of gDT-II in B16.gD.*Ciita*$^{\mathrm{WT}}$ tumours expressed PD-1 (Fig.4i) and fewer expressed the IL-7 receptor α-chain CD127 (Fig.4j) when compared to B16.gD.*Ciita*$^{\mathrm{KO}}$ tumours, both indicative of *in situ* activation. Finally, gDT-II caused a >10-fold increase in CD8$^{+}$ T cell densities in B16.gD.*Ciita*$^{\mathrm{WT}}$ but had no impact in this regard on B16.gD.*Ciita*$^{\mathrm{KO}}$ tumours (Fig.4k).

To further probe putative interactions between CD4$^{+}$ T cells and melanoma cells in *I-Ab*$^{-/-}$ mice, we transferred fluorescently-labelled preactivated gDT-II into skin inoculated with B16.gD.*Tyr*$^{\mathrm{KO}}$.mCherry 4d earlier and imaged the TME by intravital 2-photon microscopy 1–2wks later (Fig.S6e). This revealed TME niches where slowly moving or arresting gDT-II interacted with melanoma cells, indicative of direct antigen recognition; in other regions, gDT-II migrated rapidly, seemingly ignoring B16.gD (Fig.4l, Fig.S6f,g and Movies S4–7), which likely reflected heterogenous MHC II expression within and amongst individual tumours (Fig.4h). Combined, our results in *I-Ab*$^{-/-}$ mice indicate that direct recognition of MHC II$^{+}$ melanoma cells *in situ* could drive CD4$^{+}$ T cell activation and protective immunity (Fig.4m).

### *Host antigen-presenting cells activate protective CD4$^{+}$ T cell immunity.*

Given that MHC II expression by B16.gD was observed only in a minor portion of tumours *in vivo* and was heterogenous within individual tumours (Fig.4a), we next assessed the contribution of MHC II$^{+}$ host APCs, such as DCs and myeloid cells, to CD4$^{+}$ T cell activation. Of note, *in vitro* generated DCs pulsed with gD$_{(315\text{-}327)}$ peptide induced gDT-II killing of MHC II-deficient B16.gD.*Ciita*$^{\mathrm{KO}}$ (Fig.5a). Furthermore, DC-mediated gDT-II activation resulted in killing regardless of whether or not B16.gD.*Ciita*$^{\mathrm{KO}}$ were precultured with IFNɣ (Fig.5a), indicating that IFNɣ was not required to render melanoma cells susceptible to killing in this setting.

We next tested if host APCs were sufficient to promote CD4$^{+}$ T cell immunity *in vivo*. Indeed, transfer of naïve gDT-II conferred protection to challenge with B16.gD.*Ciita*$^{\mathrm{KO}}$ in WT mice (Fig.5b,c). In accordance, intravital 2-photon microscopy in CD11c.YFP or CD11c.YFP→B6.albino bone marrow chimeric mice (Fig.S7a) revealed tumour debris-laden CD11c$^{+}$ APCs accumulating around B16.gD.*Tyr*$^{\mathrm{KO}}$.mCherry, including direct cell-to-cell contacts (Fig.5d,e and Fig.S7b,c). Importantly, slow moving or arresting gDT-II were found to intimately interact with these APCs, which occurred both in direct proximity but also at some distance to melanoma cells (Fig.5d, Fig.S7b,c and Movies S8–10). These interaction dynamics illustrated active engagement of CD11c$^{+}$ APCs with melanoma cells and further implied APCs as important hubs for gDT-II activation in the TME (Fig.5c). Consistent with this, gDT-II motility in the TME was noticeably different to that observed for effector gDT-II infiltrating antigen-free, contralateral flanks of acutely HSV-infected CD11c.YFP mice (Fig.S7d and Movie S11). Furthermore, gDT-II in the TME spent more time in close proximity to APCs than in HSV control skin (Fig.5f), and these APC-associated gDT-II displayed reduced velocity, a decreased confinement ratio and increased time in arrest (Fig.5g).

To interrogate the phenotype of tumour debris-laden APCs, we analysed by flow cytometry tumour-derived CD45.2$^+$MHC II$^+$GFP$^{int}$ cells that presumably had ingested GFP$^+$ B16.gD (CD45.2$^-$GFP$^{hi}$) debris (Fig.5h). Most CD45.2$^+$MHC II$^+$GFP$^{int}$ cells, but not B16.gD, expressed costimulatory molecules CD80 and CD86 and a minority also expressed CD83 (Fig.5i,j). Furthermore, most expressed intermediate to high levels of PD-L1, with a portion of PD-L1$^{hi}$ cells also expressing PD-L2, consistent with a recently described phenotype of human DCs that had phagocytosed tumour material[48]. B16.gD cells expressed low to intermediate levels of PD-L1 but not PD-L2 (Fig.5i,j). The expression of costimulatory molecules by CD45.2$^+$MHC II$^+$GFP$^{int}$ APCs suggested an active role in productive activation of CD4$^+$ T cells *in situ*. In line with this, we noted highest levels of *Tbx21* transcript and T-bet protein expression in CD4$^+$ T cells from skin and tumours compared to LN (Fig.S7e-h). Analysis of additional markers revealed a broad spectrum of GFP$^{int}$ APC phenotypes, ranging from a small population of conventional MHC II$^{hi}$CD11c$^+$CD103$^+$XCR1$^+$ DC1s (<3%) and a larger fraction of MHC II$^{hi}$CD11c$^+$CD11b$^{high}$SIRPα$^{high}$ DC2 (~23%), to a dominant but heterogenous mix of CD11b$^{high}$ and largely MHC II$^+$ monocytes and macrophages with variable expression of SIRPα, CD64, Ly6C and F4/80 (Fig.5k-m). Thus, multiple types of MHC II$^+$ APCs ingested tumour debris and thus had the potential to interact with CD4$^+$ T cells in the TME.

Multiplex fluorescent immunohistochemistry on human melanoma tissue[49,50] confirmed colocalization of CD4$^+$ T cells and APCs, the latter identified by expression of CD11c, CD68 or FXIIIA (Fig.5n). Analysis of an additional 25-28 samples from a separate cohort of patients diagnosed with primary cutaneous melanoma[51] estimated that 14.1% of APCs (HLA-DR$^+$ SOX10$^-$) associated with CD3$^+$CD8$^-$ T cells (corresponding to CD4$^+$ T cells; Fig.S7i,j) while an additional 2.6% associated with both CD3$^+$CD8$^-$ and CD3$^+$CD8$^+$ T cells simultaneously (Fig.S7k,l). Furthermore, in this cohort, 10.3% of melanoma cells (SOX10$^+$) expressed HLA-DR$^+$ and 10.9% of these associated with CD3$^+$CD8$^-$ T cells (Fig.S7m-o), reminiscent of our results from the murine TME (Fig.4).

### ***Tumour-specific CD4$^+$ T cells control tumours in lymphocyte-deficient hosts.***

Having illustrated multiple modes of CD4$^+$ T cell activation by melanoma cells or host APCs in the TME, we sought to determine effector pathways involved in antitumoural immunity. To this end, we performed ACT with activated gDT-II in B16.gD-challenged *Rag2*$^{-/-}$;*Il2rg*$^{-/-}$ mice, which allowed us to interrogate gDT-II effector functions in the absence of endogenous lymphocytes[52]. We inoculated B16.gD and 7d later, when tumours first became visible, transferred *in vitro* activated gDT-II (Fig.6a). Intravenous transfer of $1\times10^5$ gDT-II completely protected mice from tumour outgrowth, whereas a 10-fold lower dose achieved control in around 40% of mice (Fig.S8a). Thus, we chose an intermediate number of $5\times10^4$ gDT-II for subsequent experiments, which achieved control of tumour outgrowth in >90% of mice (Fig.6b,c). Whereas all control mice developed tumours within the first 4wks, the few tumours in gDT-II recipients only progressed later (>6wks p.i.) (Fig.6b,d). Of note, some small lesions persisted throughout the observation period (Fig.6b–d). Intravital imaging confirmed early gDT-II infiltration of melanomas (Fig.6e). While many gDT-II navigated rapidly through the TME, others moved slowly or arrested in proximity to melanoma cells, illustrating productive antitumoural CD4$^+$ T cell immunity in the TME (Movie S12). Significant protection resulted from challenge with MHC II-deficient B16.gD.*Ciita*$^{KO}$ (Fig. 6f), indicating that host APCs were sufficient to drive gDT-II immunity.

### *Multiple mechanistic layers of CD4$^+$ T cell tumour control in vivo.*

To interrogate mechanisms of CD4$^+$ T cell-mediated tumour control, we focused on mediators that were involved in killing in our *in vitro* assays (Fig.3) and expressed in tumour-infiltrating CD4$^+$ T cells, as revealed by our transcriptional analysis (Fig.2h). Thus, we interfered with IFNɣ, TNFα, FasL and perforin-dependent pathways using genetic deletions or blocking Abs, the latter of which were administered from the time of gDT-II transfer for 4wks (Fig.7a). We extended the observation period to 10-12wks p.i. to track persisting lesions for potential late outgrowth. Perforin-deficient gDT-II afforded efficient protection indistinguishable from WT cells (Fig.7b). Blocking either TNFα or FasL did not result in increased tumour outgrowth, however it did lead to elevated incidences of small lesions that persisted in skin and underwent subtle changes in morphology over time (Fig.7c,d and Fig.S8b). Combined blockade of TNFα and FasL triggered slightly more outgrowth early during treatment and led to increased rates of persisting lesions, some of which grew out late after cessation of treatment (Fig.7e and Fig.S8b). Blocking IFNɣ almost completely abolished protection and caused early outgrowth in almost all mice (Fig.7f). Experiments with IFNɣ-deficient gDT-II revealed comparable results, confirming that gDT-II were indeed the source of protective IFNɣ (Fig.7g).

We next tested if IFNɣ signalling was required in the melanoma cells given its essential role in MHC II induction and its known cytotoxic and cytostatic activities towards cancer cells[53]. We deleted the IFNɣ receptor, IFNɣR1, in B16.gD (B16.gD.*Ifngr1*$^{KO}$), rendering them unresponsive to IFNɣ. Despite this, gDT-II could suppress tumour outgrowth in the majority (69%) of mice (Fig.7h). While this level of protection was slightly lower than what we observed for WT B16.gD (91%, Fig.6b), these results indicated part of the protective function of IFNɣ was through signalling in host cells. Given previous reports that IFNɣ mediates tumour control via induction of inducible nitric oxide synthase (iNOS) and NO production in myeloid cells[8,24,25,27], we used flow cytometry to measure iNOS induction in host cells in the TME. Transfer of WT gDT-II resulted in appearance of iNOS$^{hi}$MHC II$^+$Ly6C$^+$Ly6G$^-$ monocytic cells in the majority of mice (Fig.7i,j). Given the skin was analysed when melanomas were still very small, it was not surprising that the frequency of iNOS$^{hi}$ was low (on average 1.7%). Transfer of IFNɣ-deficient gDT-II resulted in roughly 10-fold lower frequencies of iNOS$^{hi}$ myeloid cells (on average 0.18%) and virtually none of these were observed in control mice that did not receive gDT-II (Fig.7i,j).

To address the potential role of NO production in tumour control, we used the iNOS inhibitor N6-(1-iminoethyl)-L-lysine (L-NIL) to treat tumour-challenged mice from the time of gDT-II transfer for 6wks. In mice challenged with IFNɣR1-competent B16.gD, L-NIL treatment did not impact gDT-II protection with all mice remaining free from progressing tumours (Fig.7k). By contrast, L-NIL treatment of B16.gD.*Ifngr1*$^{KO}$-challenged mice led to tumour outgrowth in 6 of 8 mice despite gDT-II transfer (Fig.7k). Tumours in these mice grew out both during the treatment, as well as in the 3-4wks thereafter. Thus, a significant loss of protection was only observed when melanoma cells were insensitive to IFNɣ and iNOS was blocked simultaneously. Together, these results imply an important role of NO for CD4$^+$ T cell-mediated eradication and suppression of IFNɣ-unresponsive melanoma cells (Fig.7l), and thereby illustrate multifaceted mechanisms of IFNɣ-centred CD4$^+$ T cell antitumoural immunity.

## Discussion

There is growing appreciation for the critical contributions of CD4$^+$ T cells to cancer immunity[11,32,33]. However, how diverse effector functions employed for tumour killing and noncytolytic control cooperate *in vivo* have remained unclear, as have the functional consequences of CD4$^+$ T cell activation by MHC II-expressing cancer or host APCs. In this context, we provide a comprehensive account of CD4$^+$ T cell responses in an orthotopic melanoma model that recapitulates immune-dependent outcomes seen in patients including tumour outgrowth, long-term persistence of small or microscopic lesions, and likely also complete eradication[42,43]. Using this model we have dissected several pertinent aspects of CD4$^+$ T cell immunity to cutaneous melanoma, including (i) the definition of transcriptional CD4$^+$ T cell states in TME and LN, (ii) the functional significance of melanoma-intrinsic MHC II expression, (iii) the intimate tripartite interactions between melanoma cells, host APCs and melanoma-specific CD4$^+$ T cells in the TME, and (iv) the molecular mechanisms of CD4$^+$ T cell control, including CD8$^+$ T cell-dependent and -independent functions.

Single-cell sequencing revealed that expanded TCR clones acquired transcriptomes indicative of T$_{REG}$, T$_{FH}$, T$_H$17 and T$_H$1 differentiation. In addition, there was an *Id3*$^{low}$*Bcl6*$^+$ T$_{EFF}$ cluster with mixed T$_H$17/T$_H$1 features, possibly representing a transitional state from the T$_H$17 to T$_H$1 cluster. Consistent with this notion, there was clonal overlap between the T$_H$17/proliferating, T$_H$1 and T$_{EFF}$ clusters. The presence of distinct regulatory, helper and effector subsets resembles CD4$^+$ T cell profiles in cancer patients for which tumour specificity has been inferred by clonal expansion, CXCL13 expression, interaction with APCs, and/or demonstrated by functional TCR validation *ex vivo*[14,15,31,54–56]. While we have not formally tested the antigen specificities of expanded clones, we speculate these include specificities for gD but also other MHC II-restricted antigens previously described for B16.F10 cells[57]. Our assumption that they are indeed tumour-specific is supported by transcriptional evidence for activation, including expression of *Pdcd1* (PD-1), *Icos* and *Cd69*, resembling cancer-specific $CD4^+$ T cells in patients[56]. Interestingly, we noted very little TCR clonal overlap between regulatory versus helper and effector subsets. A similar phenomenon has been reported for human tumour-specific $CD4^+$ T cells, including in melanoma patients[14,15,58], corroborating that the observed phenotype was unlikely a result of sampling bias. Such results have important implications for ACT where inadvertent use of TCRs or $CD4^+$ T cells prone to $T_{REG}$ differentiation could have adverse impacts on outcomes.

While in mice MHC II expression is largely restricted to professional APCs, melanoma cells can express MHC II, generally upon induction by IFNɣ. In patients, MHC II expression is only seen in a third of melanomas and the frequencies of MHC $II^+$ cells are generally low[14,30,59,60], consistent with our own results. In accordance, we observed variable MHC II expression only in small mouse tumours with high $CD4^+$ T cell densities, likely reflecting a degree of ongoing control with elevated levels of IFNɣ. Correspondingly, MHC II expression by cancer cells is associated with favourable outcomes and responses to anti-PD-1/PD-L1 therapy in melanoma and other cancers[14,59–61]. Nevertheless, the functional significance of cancer-intrinsic MHC II expression has remained unclear, with reports showing inefficient presentation of tumour antigens[40], that antigen presentation in the absence of costimulation favours anergy or promotes $T_{REG}$ functions[14], or that MHC II can inhibit activated T cells and NK cells via ligation of Lag-3 or Fc receptor–like 6 (FCRL6)[41]. Our results argue that melanoma-intrinsic MHC II expression can indeed be functional, as we (i) observed less $CD4^+$ T cell infiltration in B16.gD.*Ciita*$^{KO}$ tumours, (ii) demonstrated efficient MHC II-dependent gDT-II killing of MHC $II^+$ B16.gD *in vitro*, (iii) illustrated direct interactions between gDT-II and B16.gD *in vivo*, and (iv) found that MHC II induction in B16.gD can activate a level of protection in *I-Ab*$^{-/-}$ mice. The latter is in line with one study that showed melanoma-specific $CD4^+$ T cells eradicated tumours in MHC II-deficient hosts treated with combined radiotherapy and CTLA-4 blockade[35]. However, while cancer-intrinsic MHC II can promote immunity, gDT-II mediated protection from B16.gD.*Ciita*$^{KO}$ tumours in WT and lymphocyte-deficient mice, indicates it is not required for $CD4^+$ T cell-mediated control, consistent with other models[10,27,62–65].

Intravital 2-photon imaging of the TME revealed intimate tripartite interactions between melanoma cells, host $CD11c^+$ APCs and slow-moving or arresting gDT-II, indicative of *in situ* stimulation[27,47]. The observed interactions of APCs and melanoma cells likely reflect active APC surveillance of, or even attack on, melanoma cells, suggesting that APCs may acquire melanoma antigens via mechanisms other than phagocytic and scavenger functions in the TME. Future studies will be needed to clarify if such APC-melanoma interactions can indeed result in antigen transfer, or even melanoma cell injury. Regardless, the cellular dynamics we observed further implicate APCs as predominant hubs for gDT-II stimulation, consistent also with our observation of APC-$CD4^+$ T cell association in human melanoma samples. In accordance, we noted higher levels of T-bet in $CD4^+$ T cells from skin and tumours compared to LNs. This suggests that antigen encounters in the TME may drive further $CD4^+$ T cell differentiation and cytokine production. Reciprocally, $CD4^+$ T cells have been shown to license APCs in the TME, enhancing their stimulatory capacity for CD8$^+$ T cells[23] and the molecular signature of licensed conventional DC1s correlates with T cell infiltration and predicts responses to PD-1 therapy in a variety of human tumours[23]. Conversely, DCs interacting with CD4$^+$ T cells in human lung cancer express elevated levels of immunoregulatory molecules such as PD-L1 and PD-L2[54], a phenotype linked to DCs that have ingested tumour debris and to reduced antitumoural responses[48]. Thus, the functional consequences of APC-CD4$^+$ T cell interactions in the TME may differ depending on the type of APCs that are involved. In this regard, we observed a broad range of phenotypically distinct APCs that ingested tumour debris, including a small fraction of cDC1s, a larger fraction of cDC2s, as well as a dominant and heterogenous mix of CD11b$^+$MHC II$^+$ myeloid cells with variable expression of monocyte and macrophage associated markers such as SIRPα, CD64, Ly6C and F4/80.

In addition to the flexible activation modes of CD4$^+$ T cells in the TME by either APCs or MHC II$^+$ melanoma cells, we also describe a multitude of protective functions ensuing from such interactions. Protection by transfer of naïve gDT-II into WT mice partly required CD8$^+$ T cells and optimal protection was further contingent on the ability of gDT-II to infiltrate the inoculation site, likely involving CD40L/CD40-dependent licensing of DCs in both tumour-draining LNs and skin. This notion is consistent with earlier observations that CD4$^+$ T cell protection from tumours requires antigen stimulation directly in the TME[9,10]. In addition, enhanced CD8$^+$ T cell infiltration, as seen after gDT-II transfer into B16.gD-challenged *I-Ab*$^{-/-}$ mice where classical DC licensing cannot take place, could be driven by CD4$^+$ T cell production of chemokines such as CCL5/Rantes, or the induction of chemokines in melanoma and stromal cells by gDT-II-derived IFNɣ, as described for viral infection[66].

Importantly, our *in vitro* killing assays and ACT experiments in lymphocyte-deficient mice revealed direct killing and potent protection, respectively, by gDT-II independently of other lymphocytes. Interestingly, perforin-dependent killing was not essential for protection *in vivo* and showed only partial involvement *in vitro*. Consistent with this, we detected very little *Prf1* mRNA in CD4$^+$ T cells in our transcriptional analysis. This is surprising given the clinical significance of human cytotoxic CD4$^+$ T cells[32,33] and prior demonstrations that human and other murine CD4$^+$ T cells can kill tumour cells *in vitro* in a manner at least in part dependent on perforin and granzymes[30,35]. A likely explanation for this discrepancy is the involvement of indirect killing via NO production in myeloid cells as well as various other redundant cytotoxic pathways in addition to granzymes, namely TNFα and FasL. Importantly, endogenous CD4$^+$ T cells responding to B16.gD challenge expressed transcripts for these cytokines. Moreover, our ACT experiments revealed that they were required for optimal eradication of B16.gD *in vivo* as single or combined blockade resulted in increased incidence of persisting, yet often long-term controlled lesions. This nuance is clinically relevant, and may explain why a role for FasL in CD4$^+$ T cells is not apparent in cancer models where tumours grow more aggressively[35,67]. Thus, our ACT model with early intervention emphasizes the contribution of CD4$^+$ T cells and their effector molecules to tumour control in the specific contexts of early forming melanomas and long-term persistence of miniscule lesions.

In line with other reports[35,65], CD4$^+$ T cell-derived IFNɣ was essential for protection *in vivo*. IFNɣ exerts context-specific and pleiotropic effects in tumours, including direct cytostatic and cytotoxic effects on cancer cells, activation and recruitment of innate immune cells, as well as triggering destruction of tumour-supplying blood vessels[11,53]. Accordingly, while IFNɣ signalling in host cells was sufficient for substantial, yet incomplete, control of *Ifngr1*-deficient melanoma cells, pharmacological blockade of NO production in this situation, presumably by targeting iNOS-expressing MHC II$^+$Ly6C$^+$ myeloid cells, caused tumour development and outgrowth in most mice. A similar indirect pathway of NO-dependent tumour killing has been described for CD4$^+$ T cells with antigen specificities distinct to the one studied by us, including in a myeloma model[24,25] and in a melanoma model in which potent CD4$^+$ T cell-mediated control of progressing tumours was achieved by combination therapy with cyclophosphamide, virus-induced activation of transferred T cells and intratumoural application of immunostimulatory adjuvants[27]. Combined, such results argue that CD4$^+$ T cells can maintain partial NO-dependent control of melanoma cells that may have otherwise escaped control by NK and CD8$^+$ T cells and lost responsiveness to direct IFNɣ effects. Of note however, protection from challenge with IFNɣ signalling-competent B16.gD was intact despite NO inhibition, illustrating that direct IFNɣ signalling in melanoma cells alone is sufficient for a level of CD4$^+$ T cell-mediated control.

In summary, we report flexible MHC II-dependent activation of IFNɣ-dependent, multifaceted CD4$^+$ T cell immunity in cutaneous melanoma, which can contain even those melanoma cells that have otherwise escaped a multitude of immune control checkpoints. Such results argue that modulation of CD4$^+$ T cell immunity is an attractive avenue to bolster future immunotherapies.

## Materials & Methods

**Study design.** The study sought to characterise melanoma-specific CD4$^+$ T cells and their tumour-suppressive effects in an orthotopic transplantable melanoma model. We employed single-cell transcriptomics to examine CD4$^+$ T cell differentiation in response to melanoma challenge. We made use of transgenic CD4$^+$ T cells with a known tumour specificity to characterise CD4$^+$ T cell dynamics and interactions with MHC II$^+$ melanoma cells and professional APC using flow cytometry and intravital two-photon microscopy. These transgenic CD4$^+$ T cells were also used in combination with genetic approaches to investigate mechanisms of CD4$^+$ T cell-mediated tumour suppression *in vitro* and *in vivo*, the latter in both immune-competent and immune-deficient mice. Finally, we used immunofluorescence microscopy to investigate the spatial relationship of CD4$^+$ T cells and professional APC in human melanoma.

**Mice.** C57BL/6 (WT), B6.(Cg)-Tyrc-2J/J (B6.albino), gDT-II × SJL-PtprcaPep3b/BoyJ (gDT-II.CD45.1), gDT-II.GFP, gDT-II.CFP, gDT-II.CD45.1 × *Fut7*$^{-/-}$ (gDT-II.*Fut7*$^{-/-}$), gDT-II.CD45.1 × *Prf1*$^{-/-}$ (gDT-II.*Prf1*$^{-/-}$) gDT-II.CD45.1 × *Ifng*$^{-/-}$ (gDT-II.*Ifng*$^{-/-}$), gDT-II × *Tbx21*$^{-/-}$ (gDT-II.*Tbx21*$^{-/-}$) *Cd40*$^{-/-}$,*Rag2*$^{-/-}$;*Il2rg*$^{-/-}$, albino *Rag2*$^{-/-}$;*Il2rg*$^{-/-}$, B6.129S2-H2dlAb1-Ea/J (*I–Ab*$^{-/-}$) and CD11c.YFP mice were bred in the Department of Microbiology and Immunology, the University of Melbourne. gDT-II mice express the transgenic T cell receptor recognizing the herpes simplex virus type 1 (HSV-1)-derived glycoprotein D (gD), epitope gD$_{(315\text{-}327)}$ (IPPNWHIPSIQDA). *Fut7*$^{-/-}$ mice were generated by CRISPR-Cas9 using single guide RNAs targeting two exons of *fucosyltransferase 7*; GAGCTTGCGCAATGCCTAAA and GCAGACTGTACACTGGGCGC. Deleted alleles were fully validated by polymerase chain reaction and next generation sequencing. All animal experiments were conducted with female mice, on the C57BL/6 background, aged between 6–12wks at the beginning of experiments. All animal experiments were approved by the relevant University of Melbourne Animal Ethics Committee.

**B16 melanoma cell lines.** B16F10.gD.GFP (B16.gD) and B16F10.Ova.GFP (B16.Ova) were generated by transduction with retroviral vectors containing full-length gD or a membrane-bound form of chicken ovalbumin, respectively, as well as enhanced GFP (eGFP) as described[42]. B16.gD expressing firefly luciferase (B16.gD.Luc) were generated by retroviral transduction of B16.gD with a vector encoding luciferase (ffluc2) and mScarlet and selected by flow cytometric sorting on mScarlet$^+$ cells using an Aria III (BD). Tyrosinase-deficient, B16.*Tyr*$^{KO}$.mCherry, generated as previously described[43], were transduced with the retroviral vector containing full-length gD and eGFP to yield the B16.gD.*Tyr*$^{KO}$.mCherry cell line. CRISPR-Cas9 was used to generate the polyclonal cell lines B16.gD.*Ciita*$^{KO}$, B16.gD.*Tnfr1*$^{KO}$ and B16.gD.*Ifngr1*$^{KO}$ as described below. All B16 cell lines were cultured and passaged in RP-10 (RPMI medium containing 10% fetal calf serum (FCS), L-glutamine (2 mM), penicillin (100 U/mL), streptomycin (100 µg/mL) and 2-mercaptoethanol (50 µM)) at 37 °C, 5.7–6.5% CO$_2$.

**B16 melanoma inoculation and viral infection.** B16 melanoma inoculation was performed as described[43]. Briefly, melanoma cells were collected in trypsin/EDTA solution (Sigm-Aldrich) and washed 3 times in Hanks' balanced salt solution (HBSS) prior to suspension in HBSS (for subcutaneous, s.c. inoculation) or in Matrigel basement membrane matrix (Corning) (for epicutaneous, e.c. inoculation). Mice were anaesthetised by intraperitoneal (i.p.) injection of a mixture of ketamine (100mg/kg bodyweight) and xylazine (15mg/kg bodyweight) and the left flank skin was exposed by shaving and depilating using Veet cream (Reckitt Benckiser). Mice were inoculated with 1×10$^5$ B16 melanoma cells by injection under the left flank using a 30G needle (s.c.) or by application onto a scarified site on the skin formed by light abrasion with a Dremel power tool (e.c.). Mice e.c. inoculated were bandaged for 4d. Photos of the inoculation site were taken longitudinally using a dermoscopy camera (DermLite). Developing tumours were measured using a digital caliper and volume estimated using the formula: volume = ((width$^2$ × length)/2). HSV-1 infections were performed by scarification of the mouse flank skin and application of $1\times10^6$ plaque-forming units of the KOS strain of HSV-1, as described[68].

**gDT-II enrichment and *in vitro* activation.** gDT-II were enriched from LNs and spleen of gDT-II mice by negative selection as described[69] followed by positive selection using Dynabeads® mouse CD4 positive isolation kit (Invitrogen), according to the manufacturer's instructions. For gDT-II activation, purified gDT-II were mixed with splenocytes from a WT mouse pulsed with 5μM of the $gD_{(315\text{-}327)}$ peptide (IPPNWHIPSIQDA) and Lipopolysaccharides from *Escherichia coli* (0.15μg/mL, Sigm-Aldrich). Cells were cocultured in RP-10 for 6–8d at 37°C, 5.7–6.5% $CO_2$. From 48h post-activation, cells were split 1:2 and recombinant human interleukin (IL)-2 (12.5U/mL, Peprotech) was added every 24h.

**gDT-II cell transfers.** Naïve gDT-II were transferred by i.v. injection via the lateral tail vein 1d prior to tumour challenge, at a purity of 55–70% (Vα3.2$^+$ CD4$^+$). *In vitro*-activated gDT-II were transferred into *Rag2*$^{-/-}$;*Il2rg*$^{-/-}$ mice by i.v. injection via the lateral tail vein (6–7d p.i.) or into *I-Ab*$^{-/-}$ mice by intradermal (i.d.) injections surrounding the inoculation site (4d p.i.). Activated gDT-II were transferred 6–8d post-activation at a purity of >95%.

***In vivo* Ab and L-NIL treatment.** WT mice were i.p. injected with 100µg of anti-CD8 Ab (clone 2.43, Walter and Eliza Hall Institute) diluted in 100µL of PBS for 2 consecutive d prior to tumour inoculation and every 3–4d after first injection until 4wks p.i. *Rag2*$^{-/-}$;*Il2rg*$^{-/-}$ mice were i.p. injected with 200µg anti-IFNɣ (clone R4-6A2, BioXCell), 200µg anti-FasL (clone MFL3, BioXCell) or 500µg anti-TNFα (clone XT3.11, BioXCell) diluted in 100µL of PBS every 3–4d starting 7–8d p.i. (1d after gDT-II cell transfer) until 40d p.i. For iNOS inhibition, *Rag2*$^{-/-}$;*Il2rg*$^{-/-}$ mice were i.p. injected 200µg N6-(1-iminoethyl)-L-lysine (L-NIL, Cayman Chemicals) diluted in 100µL of PBS daily from 7–8d p.i. (1d after gDT-II cell transfer) for 40d. All control mice were i.p. injected with 100µL of PBS at the same time as injections with L-NIL or blocking antibodies.

**Intravital 2-photon microscopy.** Mice were anaesthetized with isoflurane (2.5% for induction, 1–1.5% for maintenance), vaporized in an 80:20 mixture of $O_2$ and air or by intraperitoneal (i.p.) injection of a mixture of ketamine (100mg/kg bodyweight) and xylazine (10mg/kg bodyweight). The flank was shaved and depilated with Veet cream. Two parallel incisions, approximately 20mm apart, were made either side of the melanoma inoculation site on the ipsilateral flank or at the equivalent location on the contralateral flank for HSV-infected mice. The skin was separated from the peritoneum and an 18mm-wide, 1mm-thick piece of stainless steel was inserted under the dermis and adhered using Vetbond tissue adhesive (3M). Vacuum grease (Dow Corning) was applied around the edges of the elevated skin. PBS was used to cover the skin and a glass coverslip was placed over the skin forming a seal with the vacuum grease. Incision sites were regularly irrigated with PBS to prevent dehydration of the peritoneum during imaging. Images were acquired with an upright FVMPE-RS (Olympus) multiphoton microscope with a 25×/1.05NA water-immersion objective enclosed in a heated chamber maintained at 35°C. Fluorescence excitation was provided by Mai Tai DeepSee (690–1040nm) and InSight DeepSee (680–1300nm) lasers (Spectra-Physics). mCherry was excited at 1120nm (InSight laser), and GFP and collagen in the skin dermis (visualized by second harmonic generation, SHG) were excited at 950nm (Mai Tai laser). Alternatively, YFP, CFP and SHG were excited at 850nm simultaneously (Mai Tai laser). For four-dimensional data sets, three-dimensional stacks were captured with a 3µm z-step size every 30–60s over a period of 1–4h. Raw image sequences and imaging data were processed in Imaris image analysis software (Bitplane v9.6 to 10). Colour codes for still images were adjusted using FIJI/ImageJ v2.0.0 (National Institutes of Health). For analysis of T cell migration, image sequences were drift corrected and automatic cell tracking was performed using the Spots function in Imaris aided by manual corrections. CD11c.YFP$^+$ cell surface was identified using the automated Surface tool algorithm, aided by manual corrections. Speed, distance, displacement and track length were calculated in Imaris. Time with APC (%) was defined as the duration when the shortest distance between the centre of mass of a gDT-II was <8µm from the closest CD11c.YFP$^+$ cell surface. Arrest was defined as instantaneous speed of less than 2µm/min. Confinement ratio was defined as the net track displacement divided by the total track length. For the generation of movies, raw image sequences were exported from Imaris and composed in Adobe After Effects (v23.0.0.59). T cell tracks from the total imaging time were superimposed on still images of respective movies.

***In vitro* coculture assays.** For all coculture assays, melanoma cells were plated in triplicate at 1.5×10$^4$ cells/well in 96-well plates with or without IFNɣ (500U/mL) in RP-10 for 3d. Melanoma cell lysate was generated by harvesting rested (not treated with IFNɣ) B16 cells in PBS and subjecting them to three freeze-thaw cycles using dry-ice and a 37°C water bath. BMDCs were pulsed overnight with B16 cell lysate, gD$_{(315\text{-}327)}$ peptide or PBS. Immediately prior to coculture, melanoma cells were gently washed twice to remove IFNɣ. For assessment of cytokine production, 2.5×10$^5$ *in vitro* activated gDT-II were suspended in RP-10 containing 10µg/mL Brefeldin A (BFA, Sigma-Aldrich), with or without 2.5×10$^5$ lysate-pulsed BMDCs, and added to the B16 cells. Cells were cocultured for 5h, during which time the plate was gently agitated twice. Cells were collected for intracellular cytokine staining and analysis by flow cytometry. For killing assays, melanoma cells were plated in 96-well black, clear-bottom microplates (Corning) and cocultured with *in vitro*-activated gDT-II or gDT-II.*Prf1*$^{-/-}$ (2.5×10$^5$) and/or BMDCs (2.5×10$^5$) in RP-10 + 6µg/mL propidium iodide (PI) for 24h. In some experiments blocking antibodies, anti-FasL (2µg/mL, clone MFL3, BioLegend), anti-IFNɣ (10µg/mL, clone R4-6A2, BioXCell), anti-TRAIL (10µg/mL, clone N2B2, eBioscience) or anti-MHC II (20µg/mL, clone M5/114.15.2, eBioscience) were added to the gDT-II or gDT-II.*Prf1*$^{-/-}$ suspensions 20min prior to coculture. As a positive control, paraformaldehyde (PFA, 4% in RP-10 + 6µg/mL PI, ProSciTech) or Triton X-100 (Triton, 0.5% in RP-10 + 6µg/mL PI, Sigm-Aldrich) was added to B16 cells immediately prior to assay. PI fluorescence (535/15nm,617/20nm) was measured every 5min by the CLARIOstar Plus Microplate Reader (BMG Labtech) over 21-

24h. Data (average of triplicates) are either shown as raw fluorescence values or normalised values (Cell death (% norm. PI uptake)). Normalisation was performed by subtracting background fluorescence (lowest PI value at time=0), determining the average maximum PI value of the B16.gD + gDT-II group or the Triton X-100-treated group and converting data to a percentage of this max PI value.

**Preprocessing for single cell RNA sequencing.** Melanoma-challenged skin ($1\times1\text{cm}^2$), brachial LNs and tumours were processed into single-cell suspensions as per protocol for flow cytometry. Cells were stained with antibodies for flow cytometry and, in one experiment, were simultaneously stained with TotalSeq-C hashtag antibodies (BioLegend). Cells were sorted by flow cytometry on an Aria III (BD). LN (d8 and d20 p.i.), skin and tumour samples were sorted on $\text{CD45.2}^{+}\text{CD3}^{+}\text{CD8}^{-}\text{CD4}^{+}\text{CD44}^{hi}$ cells. The brachial LN sample (d8 p.i.) from one experiment was additionally purified by flow cytometry for $\text{CD62L}^{low}$ cells. The naïve LN sample (batch control) was sorted on $\text{CD45.2}^{+}\text{CD3}^{+}\text{CD8}^{-}\text{CD4}^{+}\text{CD44}^{lo}\text{CD62L}^{+}$ cells. Samples were run on a 10X Chromium Controller (in a single lane for one experiment and in three separate lanes for a second experiment) and mRNA, TCR and cell surface protein sequencing libraries were prepared using the 10X Genomics Chromium Next GEM Single cell 5′ platform according to the manufacturer's instructions. Sequencing was performed on an NextSeq 2000 (Illumina) or a MGISEQ-2000RS (MGI Tech) with 100bp read length in paired end mode. Reading depth was calculated to obtain ~20,000 reads per cell for gene expression library, ~5,000 reads per cell for TCR library and ~5,000 reads per cells for cell surface (hashtag) library.

**Single-cell RNA sequencing data processing and analysis.** Sequencing reads were aligned to the mm10 reference genome and T cell receptor reference (VDJ) and counted with Cell Ranger (10x Genomics, version 6.1.2). Hashtag antibodies were demultiplexed with the cellranger multifunction specifying antibodies as "Multiplexing capture". Two batches of single cell data were merged and processed using Seurat (Satija lab, version 4.3.0)[70–72]. Specifically, cells were filtered if they contained fewer than 800 genes, more than 3–4% mitochondrial RNA, or were annotated to have more than 1 beta chain in the VDJ assay (cell doublets). SCTransform was used to normalize the counts data and determine the top 3000 variable genes. T cell receptor components (^Tra/^Trb) and mitochondrial genes (^mt) were excluded from the variable genes as unwanted factors of variance and principal component analysis was performed. Batch effects between the two datasets were removed using Harmony[73]. UMAP reductions and cell neighbours were calculated using 30 dimensions from the Harmony reduction. Clusters were detected with a resolution of 0.8. Cell states within the data were determined by assessing the expression of cluster markers (FindAllMarkers) and comparing them to published markers in the literature (merging or dividing clusters as required). All further analyses and plots were generated in R (version 4.2) using tidyverse[74] functions and ShinyCell[75]. Heatmaps were created with the pheatmap package (version 1.0.12). Differentially expressed genes were determined by pseudo-bulk analysis and the edgeR package[76]. Counts of reads were summed per cell type and batch. Pseudo bulk samples with fewer than 300,000 counts were filtered from the analysis and lowly expressed genes removed using filterByExpr(). The samples were then normalised using TMM and the calcNormFactors() function. To visualise gene expression (scaled expression values) in a dot plot, we used the DotPlot function. With the batch as a covariate, all groups of interest were entered into a design matrix and group-wise dispersion estimated with the estimateDisp() function (setting robust=TRUE). Differential genes were computed using the glmFit() and glmLRT() functions. Gene Set Enrichment analysis was used to compare our dataset to a previously-published human pan-cancer dataset[31]. Human gene signatures were analysed by identifying orthologs from the mouse transcriptome using the gorth function from the gprofiler2 package (v0.2.2), filtering out ribosomal protein transcripts and determining the top 50 differentially expressed genes (sorted by combined ES rank). Differentially expressed genes between datasets were compared using the roast function from the limma package (v3.54.2). Results of the gene set enrichment analysis were visualised by scaled -log10(P values), depicted as dot size, and proportion of the up-regulated genes in the target gene set for each cluster, where colour depicts overlap. Expanded clonotypes were defined as cells that shared the same α and β chains in the TCR assay.

**Statistics and reproducibility.** Statistical differences were calculated using two-tailed Mann–Whitney U-tests, paired t tests, log-rank Mantel–Cox tests and Kruskal-Wallis test with Dunn's test for multiple comparisons. Pooled data are shown as mean ± s.e.m. unless stated otherwise. All statistical analyses were performed using GraphPad Prism (version 9.5.1 or 10.0.3) and were two-sided. The experiments were not randomized and the investigators were not blinded to allocation during experiments and outcome assessment. No statistical methods were used to pre-determine sample size. All experiments were performed at least twice, either with similar results obtained and representative data shown, or with pooled data shown, unless otherwise stated. Pooled data include all experiments performed and no data points were excluded from analysis. Differences were considered statistically significant when P values were less than 0.05.

## References

1. Sharma, P. & Allison, J. P. The future of immune checkpoint therapy. *Science* **348**, 56–61 (2015).
2. Rosenberg, S. A., Parkhurst, M. R. & Robbins, P. F. Adoptive cell transfer immunotherapy for patients with solid epithelial cancers. *Cancer Cell* **41**, 646–648 (2023).
3. Bruni, D., Angell, H. K. & Galon, J. The immune contexture and Immunoscore in cancer prognosis and therapeutic efficacy. *Nat Rev Cancer* **20**, 662–680 (2020).
4. McLane, L. M., Abdel-Hakeem, M. S. & Wherry, E. J. CD8 T Cell Exhaustion During Chronic Viral Infection and Cancer. *Annu. Rev. Immunol.* **37**, 457–495 (2019).
5. Sharma, P., Hu-Lieskovan, S., Wargo, J. A. & Ribas, A. Primary, Adaptive, and Acquired Resistance to Cancer Immunotherapy. *Cell* **168**, 707–723 (2017).
6. Kearney, C. J. *et al.* Tumor immune evasion arises through loss of TNF sensitivity. *Sci. Immunol.* **3**, eaar3451 (2018).
7. Ossendorp, F., Mengedé, E., Camps, M., Filius, R. & Melief, C. J. M. Specific T Helper Cell Requirement for Optimal Induction of Cytotoxic T Lymphocytes against Major Histocompatibility Complex Class II Negative Tumors. *Journal of Experimental Medicine* **187**, 693–702 (1998).
8. Hung, K. *et al.* The central role of CD4(+) T cells in the antitumor immune response. *J Exp Med* **188**, 2357–2368 (1998).
9. Schietinger, A., Philip, M., Liu, R. B., Schreiber, K. & Schreiber, H. Bystander killing of cancer requires the cooperation of CD4+ and CD8+ T cells during the effector phase. *Journal of Experimental Medicine* **207**, 2469–2477 (2010).
10. Alspach, E. *et al.* MHC-II neoantigens shape tumour immunity and response to immunotherapy. *Nature* **574**, 696–701 (2019).

11. Poncette, L., Bluhm, J. & Blankenstein, T. The role of CD4 T cells in rejection of solid tumors. *Current Opinion in Immunology* **74**, 18–24 (2022).

12. Parkhurst, M. R. *et al.* Unique Neoantigens Arise from Somatic Mutations in Patients with Gastrointestinal Cancers. *Cancer Discovery* **9**, 1022–1035 (2019).

13. Marty Pyke, R. *et al.* Evolutionary Pressure against MHC Class II Binding Cancer Mutations. *Cell* **175**, 416-428.e13 (2018).

14. Oliveira, G. *et al.* Landscape of helper and regulatory antitumour CD4+ T cells in melanoma. *Nature* **605**, 532–538 (2022).

15. Veatch, J. R. *et al.* Neoantigen-specific CD4+ T cells in human melanoma have diverse differentiation states and correlate with CD8+ T cell, macrophage, and B cell function. *Cancer Cell* **40**, 393-409.e9 (2022).

16. Ferris, S. T. *et al.* cDC1 prime and are licensed by CD4+ T cells to induce anti-tumour immunity. *Nature* **584**, 624–629 (2020).

17. Borst, J., Ahrends, T., Bąbała, N., Melief, C. J. M. & Kastenmüller, W. CD4+ T cell help in cancer immunology and immunotherapy. *Nat Rev Immunol* **18**, 635–647 (2018).

18. Marzo, A. L. *et al.* Tumor-Specific CD4 $^+$ T Cells Have a Major “Post-Licensing” Role in CTL Mediated Anti-Tumor Immunity. *J Immunol* **165**, 6047–6055 (2000).

19. Zander, R. *et al.* CD4+ T Cell Help Is Required for the Formation of a Cytolytic CD8+ T Cell Subset that Protects against Chronic Infection and Cancer. *Immunity* **51**, 1028-1042.e4 (2019).

20. Cui, W., Liu, Y., Weinstein, J. S., Craft, J. & Kaech, S. M. An Interleukin-21- Interleukin-10-STAT3 Pathway Is Critical for Functional Maturation of Memory CD8+ T Cells. *Immunity* **35**, 792–805 (2011).

21. Bos, R. & Sherman, L. A. CD4 $^{+}$ T-Cell Help in the Tumor Milieu Is Required for Recruitment and Cytolytic Function of CD8 $^{+}$ T Lymphocytes. *Cancer Res* **70**, 8368–8377 (2010).

22. Martin-Orozco, N. *et al.* T Helper 17 Cells Promote Cytotoxic T Cell Activation in Tumor Immunity. *Immunity* **31**, 787–798 (2009).

23. Lei, X. *et al.* CD4+ helper T cells endow cDC1 with cancer-impeding functions in the human tumor micro-environment. *Nat Commun* **14**, 217 (2023).

24. Bogen, B., Fauskanger, M., Haabeth, O. A. & Tveita, A. CD4+ T cells indirectly kill tumor cells via induction of cytotoxic macrophages in mouse models. *Cancer Immunol Immunother* **68**, 1865–1873 (2019).

25. Fauskanger, M., Haabeth, O. A. W., Skjeldal, F. M., Bogen, B. & Tveita, A. A. Tumor Killing by CD4+ T Cells Is Mediated via Induction of Inducible Nitric Oxide Synthase-Dependent Macrophage Cytotoxicity. *Front. Immunol.* **9**, 1684 (2018).

26. Corthay, A. *et al.* Primary Antitumor Immune Response Mediated by CD4+ T Cells. *Immunity* **22**, 371–383 (2005).

27. Kruse, B. *et al.* CD4+ T cell-induced inflammatory cell death controls immune-evasive tumours. *Nature* **618**, 1033–1040 (2023).

28. Xie, Y. *et al.* Naive tumor-specific CD4+ T cells differentiated in vivo eradicate established melanoma. *Journal of Experimental Medicine* **207**, 651–667 (2010).

29. Hirschhorn-Cymerman, D. *et al.* Induction of tumoricidal function in CD4+ T cells is associated with concomitant memory and terminally differentiated phenotype. *Journal of Experimental Medicine* **209**, 2113–2126 (2012).

30. Cachot, A. *et al.* Tumor-specific cytolytic CD4 T cells mediate immunity against human cancer. *Sci. Adv.* **7**, eabe3348 (2021).

31. Zheng, L. *et al.* Pan-cancer single-cell landscape of tumor-infiltrating T cells. *Science* **374**, abe6474 (2021).

32. Oh, D. Y. & Fong, L. Cytotoxic CD4+ T cells in cancer: Expanding the immune effector toolbox. *Immunity* **54**, 2701–2711 (2021).

33. Cenerenti, M., Saillard, M., Romero, P. & Jandus, C. The Era of Cytotoxic CD4 T Cells. *Front. Immunol.* **13**, 867189 (2022).

34. Oh, D. Y. *et al.* Intratumoral CD4+ T Cells Mediate Anti-tumor Cytotoxicity in Human Bladder Cancer. *Cell* **181**, 1612-1625.e13 (2020).

35. Quezada, S. A. *et al.* Tumor-reactive CD4+ T cells develop cytotoxic activity and eradicate large established melanoma after transfer into lymphopenic hosts. *Journal of Experimental Medicine* **207**, 637–650 (2010).

36. Kitano, S. *et al.* Enhancement of Tumor-Reactive Cytotoxic CD4 $^+$ T-cell Responses after Ipilimumab Treatment in Four Advanced Melanoma Patients. *Cancer Immunol Res* **1**, 235–244 (2013).

37. Tran, E. *et al.* Cancer Immunotherapy Based on Mutation-Specific CD4+ T Cells in a Patient with Epithelial Cancer. *Science* **344**, 641–645 (2014).

38. Hunder, N. N. *et al.* Treatment of Metastatic Melanoma with Autologous CD4+ T Cells against NY-ESO-1. *N Engl J Med* **358**, 2698–2703 (2008).

39. Melenhorst, J. J. *et al.* Decade-long leukaemia remissions with persistence of CD4+ CAR T cells. *Nature* **602**, 503–509 (2022).

40. Brightman, S. E. *et al.* Tumor cells fail to present MHC-II-restricted epitopes derived from oncogenes to CD4+ T cells. *JCI Insight* **8**, e165570 (2023).

41. Johnson, D. B. *et al.* Tumor-specific MHC-II expression drives a unique pattern of resistance to immunotherapy via LAG-3/FCRL6 engagement. *JCI Insight* **3**, e120360 (2018).

42. Wylie, B. *et al.* Cross-presentation of cutaneous melanoma antigen by migratory XCR1 $^+$ CD103 $^-$ and XCR1 $^+$ CD103 $^+$ dendritic cells. *OncoImmunology* **4**, e1019198 (2015).

43. Park, S. L. *et al.* Tissue-resident memory CD8+ T cells promote melanoma–immune equilibrium in skin. *Nature* **565**, 366–371 (2019).

44. Gebhardt, T. *et al.* Different patterns of peripheral migration by memory CD4+ and CD8+ T cells. *Nature* **477**, 216–219 (2011).

45. Erdmann, I. *et al.* Fucosyltransferase VII-Deficient Mice with Defective E-, P-, and L-Selectin Ligands Show Impaired CD4 $^+$ and CD8 $^+$ T Cell Migration into the Skin, but Normal Extravasation into Visceral Organs. *J Immunol* **168**, 2139–2146 (2002).

46. Harpur, C. M. *et al.* Classical Type 1 Dendritic Cells Dominate Priming of Th1 Responses to Herpes Simplex Virus Type 1 Skin Infection. *The Journal of Immunology* **202**, 653–663 (2019).

47. Marangoni, F. *et al.* Expansion of tumor-associated Treg cells upon disruption of a CTLA-4-dependent feedback loop. *Cell* **184**, 3998-4015.e19 (2021).

48. Maier, B. *et al.* A conserved dendritic-cell regulatory program limits antitumour immunity. *Nature* **580**, 257–262 (2020).

49. Hayward, N. K. *et al.* Whole-genome landscapes of major melanoma subtypes. *Nature* **545**, 175–180 (2017).

50. Edwards, J. *et al.* Tumor Mutation Burden and Structural Chromosomal Aberrations Are Not Associated with T-cell Density or Patient Survival in Acral, Mucosal, and Cutaneous Melanomas. *Cancer Immunology Research* **8**, 1346–1353 (2020).

51. Attrill, G. H. *et al.* Detailed spatial immunophenotyping of primary melanomas reveals immune cell subpopulations associated with patient outcome. *Front. Immunol.* **13**, 979993 (2022).

52. Colucci, F. *et al.* Dissecting NK cell development using a novel alymphoid mouse model: investigating the role of the c-abl proto-oncogene in murine NK cell differentiation. *J Immunol* **162**, 2761–2765 (1999).

53. Ikeda, H., Old, L. J. & Schreiber, R. D. The roles of IFN gamma in protection against tumor development and cancer immunoediting. *Cytokine Growth Factor Rev* **13**, 95–109 (2002).

54. Cohen, M. *et al.* The interaction of CD4+ helper T cells with dendritic cells shapes the tumor microenvironment and immune checkpoint blockade response. *Nat Cancer* **3**, 303–317 (2022).

55. Lowery, F. J. *et al.* Molecular signatures of antitumor neoantigen-reactive T cells from metastatic human cancers. *Science* **375**, 877–884 (2022).

56. Duhen, R. *et al.* PD-1 and ICOS coexpression identifies tumor-reactive CD4+ T cells in human solid tumors. *Journal of Clinical Investigation* **132**, e156821 (2022).

57. Kreiter, S. *et al.* Mutant MHC class II epitopes drive therapeutic immune responses to cancer. *Nature* **520**, 692–696 (2015).

58. Ahmadzadeh, M. *et al.* Tumor-infiltrating human CD4 $^+$ regulatory T cells display a distinct TCR repertoire and exhibit tumor and neoantigen reactivity. *Sci. Immunol.* **4**, eaao4310 (2019).

59. Axelrod, M. L., Cook, R. S., Johnson, D. B. & Balko, J. M. Biological Consequences of MHC-II Expression by Tumor Cells in Cancer. *Clin Cancer Res* **25**, 2392–2402 (2019).

60. Rodig, S. J. *et al.* MHC proteins confer differential sensitivity to CTLA-4 and PD-1 blockade in untreated metastatic melanoma. *Sci. Transl. Med.* **10**, eaar3342 (2018).

61. Johnson, D. B. *et al.* Melanoma-specific MHC-II expression represents a tumour-autonomous phenotype and predicts response to anti-PD-1/PD-L1 therapy. *Nat Commun* **7**, 10582 (2016).

62. Haabeth, O. A. W. *et al.* CD4+ T-cell–Mediated Rejection of MHC Class II–Positive Tumor Cells Is Dependent on Antigen Secretion and Indirect Presentation on Host APCs. *Cancer Research* **78**, 4573–4585 (2018).

63. Shklovskaya, E. *et al.* Tumour-specific CD4 T cells eradicate melanoma via indirect recognition of tumour-derived antigen. *Immunol Cell Biol* **94**, 593–603 (2016).

64. Perez-Diez, A. *et al.* CD4 cells can be more efficient at tumor rejection than CD8 cells. *Blood* **109**, 5346–5354 (2007).

65. Mumberg, D. *et al.* CD4+ T cells eliminate MHC class II-negative cancer cells in vivo by indirect effects of IFN-. *Proceedings of the National Academy of Sciences* **96**, 8633–8638 (1999).

66. Nakanishi, Y., Lu, B., Gerard, C. & Iwasaki, A. CD8+ T lymphocyte mobilization to virus-infected tissue requires CD4+ T-cell help. *Nature* **462**, 510–513 (2009).

67. Lundin, K. U. *et al.* CD4+ T cells kill Id+ B-lymphoma cells: FasLigand-Fas interaction is dominant in vitro but is redundant in vivo. *Cancer Immunol Immunother* **53**, 1135–1145 (2004).

68. van Lint, A. *et al.* Herpes Simplex Virus-Specific CD8 $^+$ T Cells Can Clear Established Lytic Infections from Skin and Nerves and Can Partially Limit the Early Spread of Virus after Cutaneous Inoculation. *J Immunol* **172**, 392–397 (2004).

69. Bedoui, S. *et al.* Cross-presentation of viral and self antigens by skin-derived CD103+ dendritic cells. *Nat Immunol* **10**, 488–495 (2009).

70. Satija, R., Farrell, J. A., Gennert, D., Schier, A. F. & Regev, A. Spatial reconstruction of single-cell gene expression data. *Nat Biotechnol* **33**, 495–502 (2015).

71. Butler, A., Hoffman, P., Smibert, P., Papalexi, E. & Satija, R. Integrating single-cell transcriptomic data across different conditions, technologies, and species. *Nat Biotechnol* **36**, 411–420 (2018).

72. Stuart, T. *et al.* Comprehensive Integration of Single-Cell Data. *Cell* **177**, 1888-1902.e21 (2019).

73. Korsunsky, I. *et al.* Fast, sensitive and accurate integration of single-cell data with Harmony. *Nat Methods* **16**, 1289–1296 (2019).

74. Wickham, H. *et al.* Welcome to the Tidyverse. *JOSS* **4**, 1686 (2019).

75. Ouyang, J. F., Kamaraj, U. S., Cao, E. Y. & Rackham, O. J. L. ShinyCell: simple and sharable visualization of single-cell gene expression data. *Bioinformatics* **37**, 3374–3376 (2021).

76. Robinson, M. D., McCarthy, D. J. & Smyth, G. K. edgeR : a Bioconductor package for differential expression analysis of digital gene expression data. *Bioinformatics* **26**, 139–140 (2010).

**Acknowledgements**: We thank the patients and families involved in this study for their contributions to our research. Support from the MIA Biospecimen Bank Team is gratefully acknowledged. We are also grateful for continued support from colleagues at Melanoma Institute Australia, Royal Prince Alfred Hospital, and the Charles Perkins Centre, the University of Sydney.

**Funding**: T.G. is supported by an Investigator Fellowship from the National Health and Medical Research Council Australia (NHMRC, APP1194482). This work was further supported by research grants from the NHMRC (APP1187068, APP1124815, APP2008408) and the Cancer Council Victoria (APP1163465), a 350th Anniversary Research Grant from Merck KgGA and the International Research Training Group (IRTG2168) funded by the German Research Council and the University of Melbourne. The project was also supported by the Deutsche Forschungsgemeinschaft (DFG, German Research Foundation) within GRK 2168 and the Germany's Excellence Strategy–EXC2151–390873048. J.W. was supported by the Cancer Council Western Australia. K.H. was supported by the Rhian and Paul Brazis fellowship in Translational Melanoma Immunology, administered by the Peter MacCallum Cancer Foundation. This work was supported by a National Health and Medical Research Council of Australia (NHMRC) Program Grant (APP1093017) to R.A.S. G.H.A. was supported by scholarships from the University of Sydney and by the Janet Ferguson MIA PhD Scholarship. P.M.F. was supported by the McMurtrie Cancer Pathology Fellowship and the Melanoma Institute Australia. J.S.W. is supported by an NHMRC Investigator fellowship (APP1174325), Melanoma Research Alliance Young Investigator Fellowship (#700455), Cancer Institute NSW (TPG2114) and the University of Sydney. R.A.S. is supported by a National Health and Medical Research Council of Australia (NHMRC) Investigator Grant (2022/GNT2018514). Support from The Ainsworth Foundation, The CLEARbridge Foundation, Cameron Family and Lady Mary Fairfax Charitable Trust to the Melanoma Institute Australia are also gratefully acknowledged.

**Author contributions:** E.G.B., M.H., K.H., and T.G conceived the study with input from all authors on project design. Data curation and formal analysis was performed by E.G.B., T.W., J.S., G.A., J.J.E., T.G. Funding was acquired by A.H., R.A.S., D.E.G., U.P., S.B., J.W., M.H., T.G. Investigation was performed by E.G.B., T.W., J.S., M.E., D.H., L.N., G.H.A., A.R.L., S.E., D.F., M.d.L., E.G., N.M., R.D., A.L.F., J.J.E., P.M.F., J.S.W., C.M.J., K.H., and validation experiments performed by T.W., A.R.L., S.E. Resources were provided by P.M.F., R.A.S., J.S.W., A.G.B., U.P., S.B., J.W., M.H., T.G. The project was supervised by K.H., M.H., T.G. The original draft was written by E.G.B. and T.G. and all authors contributed to reviewing and editing the manuscript.

**Competing interests:** T.G. is scientific advisory board member of oNKo Innate Pty. Ltd and with S.B has received research funding from Merck Healthcare KGaA. C.M.J is an employee of the VA Maryland Health Care System. The views reported in this paper do not reflect the views of the Department of Veterans Affairs or the United States Government. C.M.J has an equity position with Cartesian Therapeutics. D.E.G has received honoraria from Bristol Myers Squibb and Merck Sharp & Dohme and is on an Advisory Board at Q Biotics, Provectus, Amgen and Bayer. R.A.S. has received fees for professional services from F. Hoffmann-La Roche Ltd, Evaxion, Provectus Biopharmaceuticals Australia, Qbiotics, Novartis, Merck Sharp & Dohme, NeraCare, AMGEN Inc., Bristol-Myers Squibb, Myriad Genetics, GlaxoSmithKline. D.H. is currently an employee of LAMPseq Diagnostics GmbH, Bonn, Germany.

**Data and Materials availability**: Single-cell RNA sequencing data have been deposited in the Gene Expression Omnibus under accession number GSE232063. Tabulated underlying data are available in Data file S1. All other data needed to support the conclusions of the paper are present in the paper or the Supplementary Materials. Materials generated as part of this study mice can be shared upon completion of standard material transfer agreements with the University of Melbourne.

## Figure captions

**Figure 1: CD4$^+$ T cells protect against epicutaneous melanoma challenge. a–c,** Characterisation of tumour development in WT mice inoculated with B16.gD. **a,** Proportion of tumour-free mice or mice with a lesion ≤1mm$^3$ and **b,** tumour growth kinetics following e.c. (epicut.) or s.c. (subcut.) inoculation. Data pooled from 22 independent experiments (e.c.; 148 mice) or a single experiment (s.c.; 5 mice). **c,** Incidence of progressing tumours after e.c. B16.gD inoculation in individual experiments. Data pooled from 22 independent experiments with ≥5 mice per experiment. **d,** Schematic of experiments in **e**+**f**. WT mice were infected with HSV-1 on skin and e.c. inoculated with B16.gD or B16.Ova on ipsilateral flanks >16wks later. **e,** Proportion of tumour-free mice or mice with a lesion ≤1mm$^3$ amongst HSV-memory (HSV) or naïve aged-matched mice (Ctrl) challenged with B16.gD. Pooled data from 4 independent experiments with 27 (Ctrl) or 31 (HSV) mice. **f,** Proportion of tumour-free mice or mice with a lesion ≤1mm$^3$ for HSV-memory mice e.c. challenged with B16.gD or B16.Ova. Data pooled from 2 independent experiments with 15 (B16.gD) or 16 (B16.Ova) mice. **g,** Schematic of experiments in **h**+**i**. WT mice were i.v. transferred 1×10$^4$ naïve gDT-II 1d prior to e.c. inoculation with B16.gD. **h,** Proportion of tumour-free mice or mice with a lesion ≤1mm$^3$ for gDT-II-recipient (gDT-II) or naïve control (Ctrl) mice. Data pooled from 7 independent experiments with 42 (gDT-II) or 37 (Ctrl) mice. **i,** Incidence of mice with outgrowing tumours in individual experiments depicted in (**h**). Data pooled from 7 independent experiments with ≥5 mice per group. **j,** Proportion of tumour-free WT mice or mice with a lesion ≤1mm$^3$ that were i.v. transferred 1×10$^4$ naïve gDT-II, inoculated e.c. with B16.gD and treated i.p. with anti-CD8 Ab (gDT-II + αCD8) or PBS (gDT-II), or did not receive gDT-II but were treated with anti-CD8 Ab (αCD8). Shaded area indicates duration of i.p. injections. Data pooled from 4 independent experiments with 20 (gDT-II and gDT-II + αCD8) or 18 (αCD8) mice. **k,** Proportion of tumour-free WT mice or mice with a lesion ≤1mm$^3$ that were i.v. transferred 5×10$^4$ naïve gDT-II.WT or gDT-II.*Fut7*$^{–/–}$ or not transferred gDT-II (Ctrl), and e.c. inoculated with B16.gD. Data pooled from 3 independent experiments with 21 mice per group. **l,** Proportion of WT or *Cd40*$^{–/–}$ tumour-free (or radiance signal ≤3×10$^5$ p/s) mice after e.c. inoculation with B16.gD.Luc. Data pooled from 3 experiments with 19 (WT) or 17 (*Cd40*$^{–/–}$*)* mice. All statistics by Log-rank Mantel–Cox test. **m–o,** Representative 2-photon microscopy of skin inoculation sites in B6.albino 6–9d p.i.. Mice were i.v. transferred with 1–5×10$^4$ naive gDT-II.GFP (green) 1d prior to e.c. inoculation with B16.gD.*Tyr*$^{KO}$.mCherry (magenta). Second harmonic generation (SHG) signal, white. Images from three individual mice representative of 5 independent experiments with 11 mice. Time stamps represent h:min:s.

**Figure. 2: Transcriptional profiles of CD4$^+$ T cells after epicutaneous B16.gD challenge. a,** Schematic for single-cell RNA sequencing experiments. WT mice were e.c. inoculated with B16.gD. CD45.2$^+$CD3$^+$CD8$^–$CD4$^+$CD44$^+$ cells were isolated from melanoma-challenged skin (d8), progressing tumours (d20) and ipsilateral brachial LNs (d8, d20). CD45.2$^+$CD3$^+$CD8$^–$CD4$^+$CD44$^{low}$ cells were isolated from brachial LNs of naïve mice. Data from 2 independent experiments analysed and integrated using Seurat clustering and Harmony. **b–h,** Analysis of

13900 CD4$^+$ T cells. Data pooled from 2792 (inoculation site skin d8), 2638 (LN d8), 907 (tumour d20), 3327 (LN d20) and 4236 cells (naïve LN) from 2 independent experiments (skin, LN d8; naïve LN) and a single experiment (tumour d20 and LN d20) with 32 (skin and LN d8), 4 (tumour and LN d20) and 2 (naïve LN) mice. **b,** Samples superimposed on uniform manifold approximation and projection (UMAP). **c,** Seurat clusters on UMAP, annotated based on expression of CD4$^+$ T cell subset-associated signature genes. Peri, peripheral. **d,** Top 20 expanded clones (≥8 cells) determined by single-cell TCR sequencing projected onto UMAP. Data pooled from 386 cells. **e,** Cluster distribution of the top 20 expanded TCR clonotypes, ranked by abundance, showing cell numbers (left) or frequencies (right) per cluster. **f,** Examples of individual TCR clonotypes superimposed on UMAP (n, cell number). **g+h,** Normalised log2 expression values for genes associated with activation (**g**) or effector function (**h**) superimposed on UMAP.

**Figure 3: gDT-II directly kill B16.gD *in vitro*. a,** Schematic of *in vitro* killing assay measuring cell death via propidium iodide (PI) uptake (fluorescence). **b,** Fluorescence (raw values) measured during coculture of B16.gD, pretreated (right) or not (left) with IFNɣ, with different numbers of activated gDT-II as indicated. Pos. ctrl; B16.gD cells treated with 4% paraformaldehyde. Data pooled from 4 independent experiments. **c–l,** Cell death of IFNɣ-treated B16 cell lines calculated as a percentage of the average maximum PI value of IFNɣ-treated B16.gD + gDT-II. All statistics by paired t test at final timepoint (21h). Data pooled from 3 (d,e,j,l) or 4 (c,f,g,h,i,k) independent experiments. **c,** Coculture of B16.gD with gDT-II, with or without anti-MHC II blocking Ab. **d,** Coculture of B16.gD.*Ciita*$^{\mathrm{WT}}$ or B16.gD.*Ciita*$^{\mathrm{KO}}$ with gDT-II. **e,** Coculture of B16.gD or B16.Ova with gDT-II. **f,** Coculture of B16.gD with gDT-II, with or without anti-TRAIL blocking Ab. **g,** Coculture of B16.gD with gDT-II, with or without anti-IFNɣ blocking Ab. **h,** Coculture of B16.gD with gDT-II or gDT-II.*Prf1*$^{-/-}$. **i,** Coculture of B16.gD or B16.gD.*Tnfr1*$^{\mathrm{KO}}$ with gDT-II. **j,** Coculture of B16.gD with gDT-II or B16.gD.*Tnfr1*$^{\mathrm{KO}}$ with gDT-II.*Pfr1*$^{-/-}$. **k,** Coculture of B16.gD with gDT-II with or without anti-FasL blocking Ab. **l,** Coculture of B16.gD with gDT-II or B16.gD.*Tnfr1*$^{\mathrm{KO}}$ with gDT-II.*Pfr1*$^{-/-}$ and an anti-FasL blocking Ab. **m,** Cartoon depicting mechanisms of CD4$^+$ T cell killing of melanoma cells *in vitro.*

**Figure. 4: MHC II-expressing melanoma cells activate CD4$^+$ T cell immunity. a–d,** Flow cytometric analysis of tumours from WT mice (naïve or i.v. transferred 1×10$^4$ naïve gDT-II) e.c. challenged with B16.gD.*Ciita*$^{\mathrm{WT}}$ or B16.gD.*Ciita*$^{\mathrm{KO}}$. **a,** Percentage of MHC II-expressing B16.gD.*Ciita*$^{\mathrm{WT}}$ cells versus tumour volume. Data pooled from 8 independent experiment with 33 mice. **b,** Number of intratumoural CD4$^+$ T cells (CD45$^+$CD8$^-$CD4$^+$) versus tumour volume in B16.gD.*Ciita*$^{\mathrm{WT}}$ tumours. Data pooled from 8 independent experiments with 36 mice. **c,** Number of intratumoural CD4$^+$ T cells (for tumours <70 mm$^3$) stratified by B16.gD.*Ciita*$^{\mathrm{WT}}$ MHC II expression (MHC II$^{\mathrm{neg}}$ <2% MHC II$^+$ cells; MHC II$^{\mathrm{hi}}$ >28% MHC II$^+$). Data pooled from 8 independent experiments with 10 (MHC II$^{\mathrm{neg}}$) and 7 (MHC II$^{\mathrm{hi}}$) mice. Statistics by two-sided Mann–Whitney test; bars display means. **d,** CD4$^+$ T cell number in tumours from WT mice e.c. challenged with B16.gD.*Ciita*$^{\mathrm{WT}}$ or B16.gD.*Ciita*$^{\mathrm{KO}}$. Data pooled from 24 (B16.gD.*Ciita*$^{\mathrm{WT}}$) or 15 (B16.gD.*Ciita*$^{\mathrm{KO}}$) mice from 5 independent experiments. Boxes depict percentage of tumours with ≥100 CD4$^+$ T cell/mm$^3$. **e,** Schematic for experiments in **f–k**. *I-Ab*$^{-/-}$ mice e.c. inoculated with B16.gD.*Ciita*$^{\mathrm{WT}}$ or B16.gD.*Ciita*$^{\mathrm{KO}}$ received intradermal (i.d.) transfer of 4×10$^6$ activated gDT-II (gDT-II) or i.d. injection of an equivalent volume of PBS (Ctrl) 4d later. **f+g,** Proportion of tumour-free mice or mice with tumours <20 mm$^3$ inoculated with B16.gD.*Ciita*$^{\mathrm{WT}}$ (**f**) or B16.gD.*Ciita*$^{\mathrm{KO}}$ (**g**). Statistics by Log-rank Mantel–Cox test. **h**–**k**, Flow cytometric analysis of B16.gD *Ciita*$^{\mathrm{WT}}$ (orange) or B16.gD.*Ciita*$^{\mathrm{KO}}$ (red) tumours (volume >20mm$^3$). Statistics by two-sided Mann–Whitney test; bars display means. **h,** MHC II expression by B16.gD.*Ciita*$^{\mathrm{WT}}$ and B16.gD.*Ciita*$^{\mathrm{KO}}$. Data pooled from 4 independent experiments with 8 (B16.gD.*Ciita*$^{\mathrm{WT}}$ Ctrl and B16.gD.*Ciita*$^{\mathrm{WT}}$ gDT-II), 4 (B16.gD.*Ciita*$^{\mathrm{KO}}$ Ctrl) and 9 (B16.gD.*Ciita*$^{\mathrm{KO}}$ gDT-II) mice. **i+j,** PD-1 (**i**) and CD127 (**j**) expression by gDT-II. Data pooled from 8 mice per group from 4 independent experiments. **k,** Number of intratumoural CD8$^+$ T cells (CD45$^+$CD4$^-$CD8$^+$). Data pooled from 8 (B16.gD.*Ciita*$^{\mathrm{WT}}$ Ctrl and B16.gD.*Ciita*$^{\mathrm{WT}}$ gDT-II), 4 (B16.gD.*Ciita*$^{\mathrm{KO}}$ Ctrl) and 9 (B16.gD.*Ciita*$^{\mathrm{KO}}$ gDT-II) mice from 4 independent experiments. **l,** Representative 2-photon microscopy analysis of the skin inoculation site in *I-Ab*$^{-/-}$ mice challenged with B16.gD.*Tyr*$^{\mathrm{KO}}$.mCherry (red) and i.d. transferred activated gDT-II.CFP (cyan). Images corresponding to movies (left, Movie S4; right, Movie S5). gDT-II tracks from total imaging time (left, 1h 40min; right, 1h 14min) superimposed on images. Time stamps represent h:min:s. Arrows point to tracks of slow moving or arrested gDT-II. SHG signal, white; autofluorescent hair, cyan. Representative of 2 independent experiments with 7 mice including transfer of gDT-II.CFP or gDT-II.GFP. **m,** Cartoon depicting direct interaction between CD4$^+$ T cells and melanoma cells *in vivo* in the absence of host MHC II.

**Figure. 5: Host APCs are sufficient to activate CD4$^+$ T cell immunity to cutaneous melanoma.** **a,** Cell death measured by PI uptake (fluorescence) during coculture of B16.gD.*Ciita*$^{\mathrm{KO}}$ (pre-treated, right, or not, left, with IFNɣ) with activated gDT-II and DCs pulsed with gD$_{(315\text{-}327)}$ peptide (orange) or DCs pulsed with gD$_{(315\text{-}327)}$ peptide without gDT-II (maroon). Positive control (Pos. ctrl) represents B16.gD treated with 0.5% Triton X-100. Cell death calculated as a percentage of the average maximum PI value of Pos. ctrl. Statistics by paired t test at final timepoint (22h). Data pooled from 3 independent experiments. **b,** Proportion of WT tumour-free mice or mice with a lesion ≤1 mm$^3$ following e.c. inoculation with B16.gD.*Ciita*$^{\mathrm{KO}}$, comparing mice i.v. transferred 1×10$^4$ naïve gDT-II prior to tumour challenge (gDT-II) or naïve control (Ctrl) mice. Data pooled from 4 independent experiments with 30 (gDT-II) or 31 (Ctrl) mice. Statistics by Log-rank Mantel–Cox test. **c,** Cartoon depicting indirect killing of melanoma cells by CD4$^+$ T cells stimulated by APCs presenting melanoma-derived antigen. **d–g,** 2-photon microscopy of the skin inoculation site of CD11c.YFP or CD11c.YFP→B6.albino chimeric mice that were i.v. transferred naïve gDT-II.CFP (1×10$^4$) 1d prior to e.c. inoculation with B16.gD.*Tyr*$^{\mathrm{KO}}$.mCherry or HSV-1, and imaged d7-10 p.i. **d,** Representative 2-photon microscopy image depicting gDT-II.CFP (cyan), CD11c.YFP (yellow) and B16.gD.*Tyr*$^{\mathrm{KO}}$.mCherry (red) cells in a melanoma-challenged CD11c.YFP mouse. SHG signal, white; autofluorescent hairs, cyan/white. Tracks of gDT-II from the total imaging time superimposed on image (corresponding to Movie S8). Time stamp represents h:min:s. Arrows indicate examples of arrested gDT-II. **e,** Sequences of 3µm-thick slices from two individual Z-stacks from melanoma-challenged CD11c.YFP→B6.albino chimeric mice depicting gDT-II.CFP (cyan), CD11c.YFP (yellow) and B16.gD.*Tyr*$^{\mathrm{KO}}$.mCherry cells (red) cells. SHG signal, white. Arrows point to cell-cell contacts between gDT-II and CD11c.YFP$^+$ cells (lower panels), including CD11c.YFP$^+$ cells that contain tumour-derived debris (upper panels). **d+e,** Data representative of 4 independent experiments with 15 mice (CD11c.YFP or CD11c.YFP→B6.albino). **f+g,** Analysis of gDT-II motility in ipsilateral flanks of melanoma-challenged mice (TME) or contralateral flanks of HSV-1-challenged mice (HSV) d7-9 p.i. Data pooled from 2 independent experiments with 4 mice from 5 videos (TME) or one experiment with 2 mice from 3 videos (HSV). Statistics by two-sided Mann–Whitney test; red lines display means. **f,** Percentage of time in which a gDT-II was <8µm from the closest surface of a CD11c.YFP$^+$ cell. Grey box depicts gDT-II closely associated with CD11c.YFP$^+$ cells (time with APC ≥80%). Data from 163 (TME) or 606 (HSV) gDT-II. **g,** Speed, confinement ratio and percentage of time in arrest of gDT-II closely associated with APC (time with APC ≥ 80%). Data from 60 (TME) or 39 (HSV) gDT-II. **h-m,** Flow cytometric analysis of tumours from WT mice e.c. inoculated with B16.gD. **h,** Representative flow cytometry plot from B16.gD tumour pregated on live (DAPI-negative), single cells. **i**+**j,** Representative flow cytometry plots (**i**) and pooled flow cytometric analysis (**j**) of coreceptor molecules on CD45.2$^+$MHC II$^+$GFP$^{\mathrm{int}}$ cells or CD45$^-$GFP$^+$ cells (B16.gD). Data pooled from 2 independent experiments with 7 mice. Bars display means. **k-m,** Flow cytometric analysis of GFP$^{\mathrm{int}}$CD45.2$^+$ cells, clustered by FlowSOM and visualised as a UMAP. Data shown are pooled from 6 mice from one of 2 independent experiments. **k,** Expression of APC markers overlayed on UMAP. **l,** Manually annotated cell types based on makers shown in (**k**). **m,** Cell density visualised on UMAP. **n,** Multiplex fluorescent IHC of human melanoma. Arrows point to examples of close associations between CD4$^+$ T cells and APC, the latter identified by expression of combinations of CD11c, CD68 and FXIIIA.

**Figure 6: Activated gDT-II protect against B16.gD challenge in absence of other lymphocytes.** **a,** Schematic for experiments in **b–d**. *Rag2*$^{-/-}$;*Il2rg*$^{-/-}$ mice were e.c. inoculated with B16.gD and i.v. transferred or not 5×10$^4$ activated gDT-II 1wk p.i. **b**+**c,** Tumour outcomes depicted as (**b**) proportion of tumour-free mice or mice with tumours <20mm$^3$ or as (**c**) proportion of mice with outgrowing tumours (shaded), persisting lesions (striped) or visibly free from tumour (white) at experiment endpoint (>10wks p.i.), for gDT-II-recipient mice (gDT-II) or mice not transferred gDT-II (Ctrl). Data pooled from 5 independent experiments with 17 (Ctrl) and 23 (gDT-II) mice. **d,** Representative dermoscopic photographs taken longitudinally (wks p.i.) depicting different tumour outcomes from two gDT-II-recipient mice (top and middle) or a control mouse (Ctrl, bottom). Scale bar, 1mm. **e,** 2-photon microscopy images of the skin inoculation site d15 p.i., from an albino *Rag2*$^{-/-}$;*Il2rg*$^{-/-}$mouse challenged with B16.gD.*Tyr*$^{\mathrm{KO}}$.mCherry (magenta) and i.v. transferred 5×10$^4$ activated gDT-II.GFP (green) 1wk p.i. Image from Movie S12, showing entire Z-stack (left) and 3µm-thick zoomed-in slices from the same region 30µm apart. SHG signal, white. Data representative of 7 mice from 2 independent experiments. **f,** Proportion of *Rag2*$^{-/-}$;*Il2rg*$^{-/-}$ tumour-free mice or mice with

tumours <20mm$^{3}$ following inoculation with B16.gD.*Ciita*$^{WT}$ (left) or B16.gD.*Ciita*$^{KO}$ (right) and i.v. transferred (gDT-II) or not (Ctrl) 5×10$^{4}$ activated gDT-II 1wk p.i. Data pooled from 2 independent experiments with 9 (B16.gD.*Ciita*$^{WT}$ Ctrl) or 10 (all other groups) mice. Statistics by Log-rank Mantel–Cox test (**b,f**).

**Figure 7: Mechanisms of gDT-II protection from melanoma challenge. a,** Schematic for experiments in **b–h**. *Rag2*$^{-/-}$;*Il2rg*$^{-/-}$ mice were e.c. inoculated with B16.gD (**b–g**) or B16.gD.*Ifngr1*$^{KO}$ (**h**) and i.v. transferred 5×10$^{4}$ activated gDT-II (WT, **b-h**), gDT-II.*Prf1*$^{-/-}$ (**b**) or gDT-II.*Ifng*$^{-/-}$ (**g**) 1wk p.i. or did not receive gDT-II (Ctrl, grey). Mice were injected every 3–4d from 1–5wks p.i. with anti-TNFα (**c**), anti-FasL (**d**) combined anti-FasL and anti-TNFα (**e**) or anti-IFNɣ Abs (**f**). **b–h,** Survival curves depict proportion of tumour-free mice or mice with tumours <20mm$^{3}$ (left) and corresponding pie charts indicate the proportion of mice with outgrowing tumours (shaded), persisting lesions (striped) or visibly free from tumour (white) at experiment endpoint (>10wks p.i., right). Pie charts colours correspond to legends for survival curves. Statistics by Log-rank Mantel–Cox test comparing experimental groups to gDT-II (black) in **b-g** or to control (Ctrl, grey) in **h**. **b,** Data pooled from 3 independent experiments with 10 (Ctrl), 14 (gDT-II) or 13 (gDT-II.*Prf1*$^{-/-}$) mice. **c,** Data pooled from 2 independent experiments with 7 (Ctrl) and 9 (gDT-II and gDT-II + αTNF) mice. **d**, Data pooled from 4 independent experiments with 14 (Ctrl), 18 (gDT-II) or 19 (gDT-II + αFasL) mice. **e**, Data pooled from 3 independent experiments with 10 (Ctrl) and 13 (gDT-II and gDT-II + αFasL + αTNF) mice. **f**, Data pooled from 2 independent experiments with 7 (Ctrl), 9 (gDT-II) or 10 (gDT-II + αIFNɣ) mice. **g**, Data pooled from 2 independent experiments with 7 (Ctrl) or 9 (gDT-II and gDT-II.*Ifng*$^{-/-}$) mice. **h**, Data pooled from 3 independent experiments with 10 (Ctrl) or 13 (gDT-II) mice. **i+j,** Flow cytometric analysis of intracellular iNOS expression in MHC II$^{+}$Ly6C$^{+}$Ly6G$^{-}$ cells isolated from the skin (d12 p.i.) of *Rag2*$^{-/-}$;*Il2rg*$^{-/-}$ mice inoculated with B16.gD that received 5×10$^{4}$ activated gDT-II.WT or gDT-II.*Ifng*$^{-/-}$ 1 wk p.i., or did not receive gDT-II (Ctrl) **i,** Representative flow cytometry plots where gates depict fraction of iNOS$^{hi}$ cells and **j,** pooled analysis of the percentage of iNOS$^{hi}$ cells from 3 independent experiments with 14 (gDT-II.WT), 15 (gDT-II.*Ifng*$^{-/-}$) and 10 (Ctrl) mice. Statistics by Kruskal-Wallis test with Dunn's test for multiple comparisons. **k,** *Rag2*$^{-/-}$;*Il2rg*$^{-/-}$ mice were e.c. inoculated with B16.gD (WT) or B16.gD.*Ifngr1*$^{KO}$ and i.v. transferred 5×10$^{4}$ activated gDT-II 1wk p.i. Mice were i.p. injected daily with iNOS inhibitor, L-NIL, for 40d following gDT-II cell transfer, or injected with PBS (B16.gD). Survival curves depict proportion of tumour-free mice or mice with tumours <20mm$^{3}$ and pie charts indicate the proportion of mice with outgrowing tumours (shaded), persisting lesions (striped) or visibly free from tumour (white) at experiment endpoint (12wks p.i.). Data pooled from 2 independent experiments with 8 (B16.gD and B16.gD.*Ifngr1*$^{KO}$ + L-NIL) or 9 (B16.gD.*Ifngr1*$^{KO}$ and B16.gD + L-NIL) mice. Statistics calculated by Log-rank Mantel–Cox test. **l,** Cartoon depicting the role of IFNɣ in CD4$^{+}$ T cell-mediated control of IFNɣ-responsive (right) and IFNɣ-unresponsive (left) melanoma cells. The latter involves IFNɣ-dependent activation of iNOS and NO production in host myeloid cells.

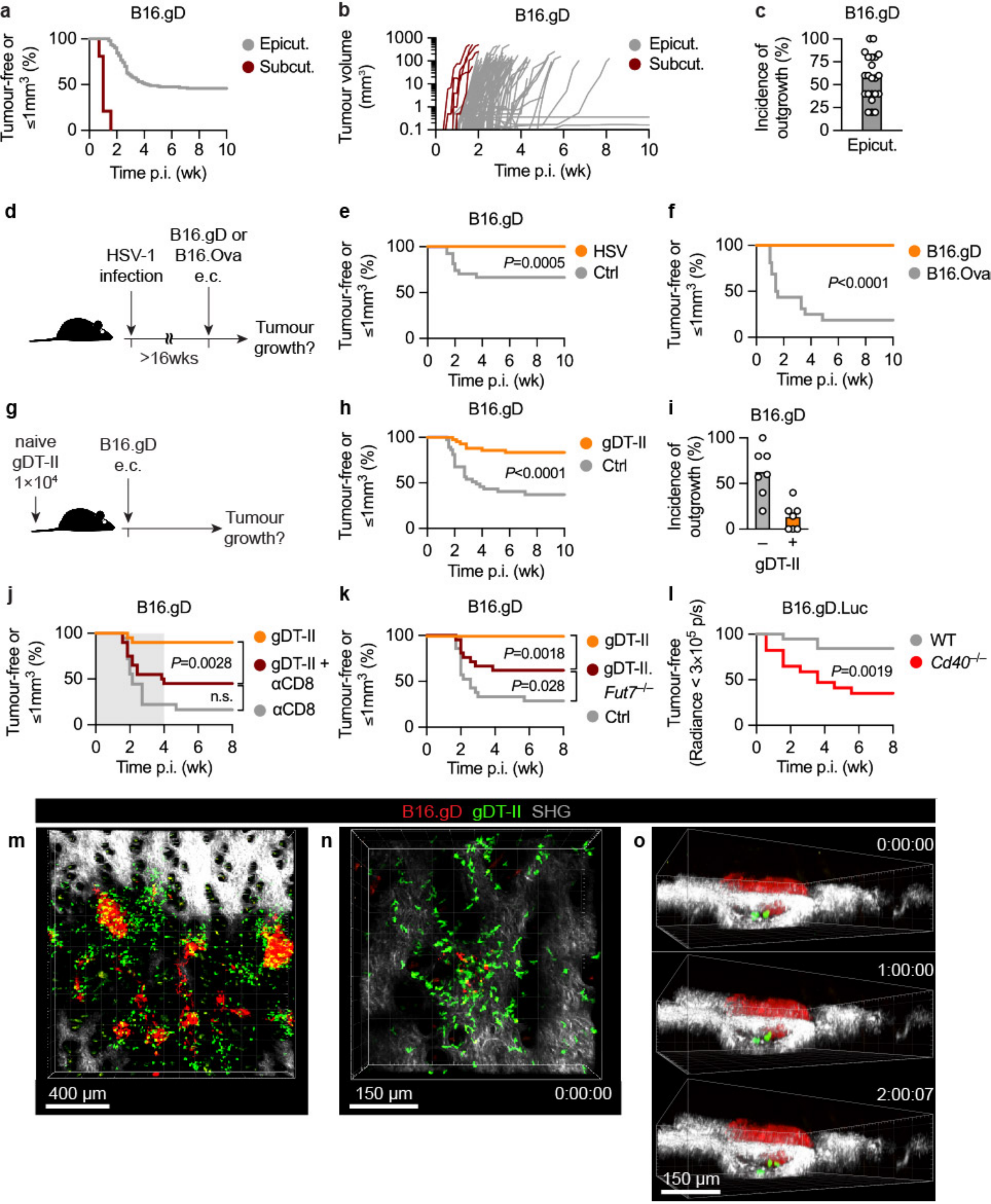
a
B16.gD
Tumour-free or ≤1mm³ (%)
Time p.i. (wk)
Epicut.
Subcut.
b
B16.gD
Tumour volume (mm³)
Time p.i. (wk)
Epicut.
Subcut.
c
B16.gD
Incidence of outgrowth (%)
Epicut.
d
HSV-1 infection
B16.gD or B16.Ova e.c.
>16wks
Tumour growth?
e
B16.gD
HSV
Ctrl
P=0.0005
f
B16.gD
B16.Ova
P<0.0001
g
naive gDT-II 1×10⁴
B16.gD e.c.
Tumour growth?
h
B16.gD
gDT-II
Ctrl
P<0.0001
i
B16.gD
gDT-II
j
B16.gD
gDT-II
gDT-II + αCD8
αCD8
P=0.0028
n.s.
k
B16.gD
gDT-II
gDT-II.Fut7⁻/⁻
Ctrl
P=0.0018
P=0.028
l
B16.gD.Luc
Tumour-free (Radiance < 3x10⁵ p/s)
WT
Cd40⁻/⁻
P=0.0019
B16.gD gDT-II SHG
m
400 µm
n
150 µm
0:00:00
o
0:00:00
1:00:00
2:00:07
150 µm

Figure 1

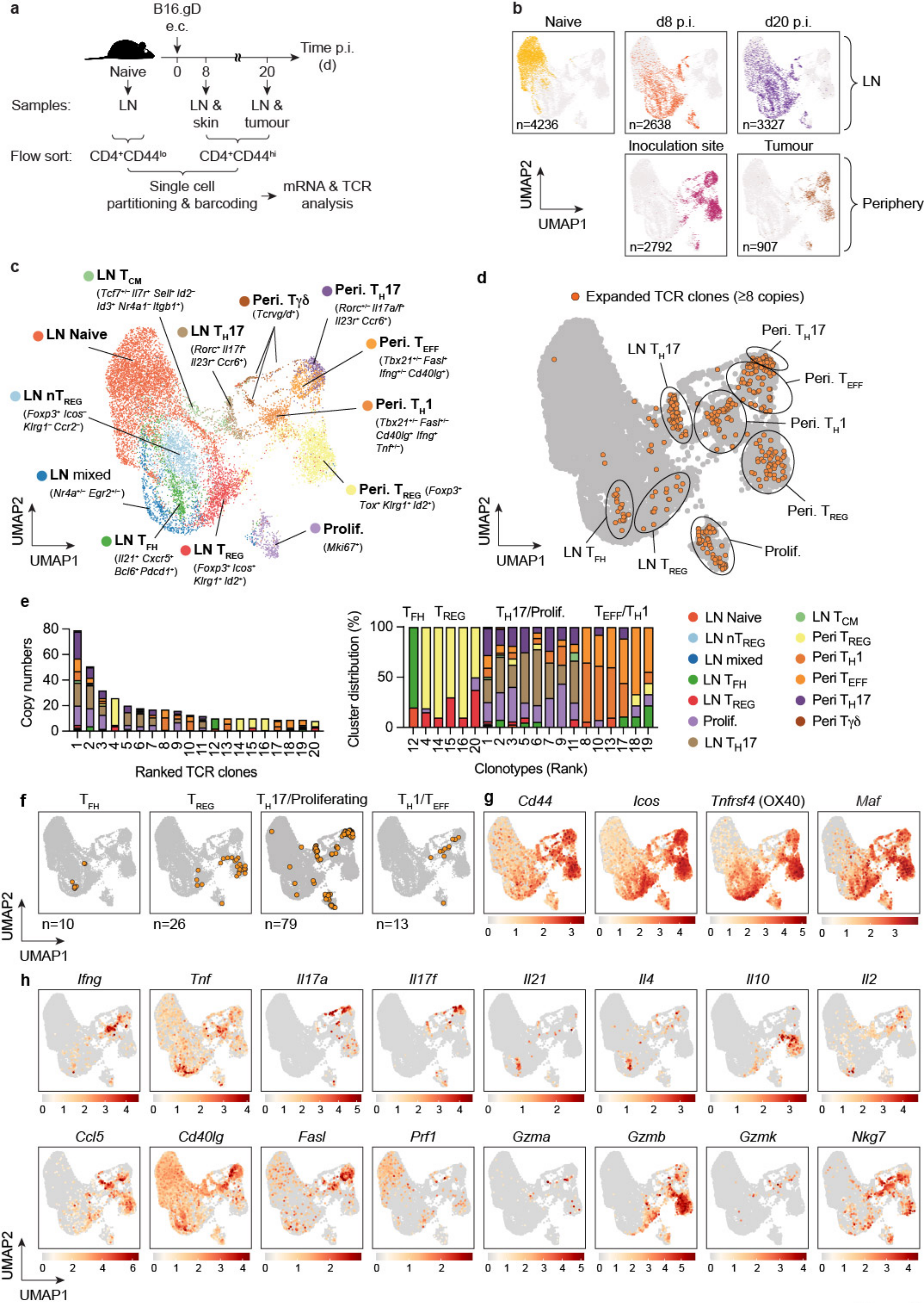
a
B16.gD
e.c.
Time p.i. (d)
Naive
0
8
20
Samples:
LN
LN & skin
LN & tumour
Flow sort:
CD4+CD44lo
CD4+CD44hi
Single cell partitioning & barcoding
mRNA & TCR analysis
b
Naive
d8 p.i.
d20 p.i.
n=4236
n=2638
n=3327
LN
Inoculation site
Tumour
n=2792
n=907
Periphery
UMAP2
UMAP1
c
LN TCM (Tcf7+/– Il7r+ Sell+ Id2– Id3+ Nr4a1– Itgb1+)
LN Naive
LN TH17 (Rorc+ Il17f+ Il23r+ Ccr6+)
Peri. Tγδ (Tcrvg/d+)
Peri. TH17 (Rorc+/– Il17a/f+ Il23r+ Ccr6+)
Peri. TEFF (Tbx21+/– Fasl+ Ifng+/– Cd40lg+)
LN nTREG (Foxp3+ Icos– Klrg1– Ccr2–)
Peri. TH1 (Tbx21+/– Fasl+/– Cd40lg+ Ifng+ Tnf+/–)
LN mixed (Nr4a+/– Egr2+/–)
Peri. TREG (Foxp3+ Tox+ Klrg1+ Id2+)
Prolif. (Mki67+)
LN TFH (Il21+ Cxcr5+ Bcl6+ Pdcd1+)
LN TREG (Foxp3+ Icos+ Klrg1+ Id2+)
UMAP2
UMAP1
d
Expanded TCR clones (≥8 copies)
Peri. TH17
LN TH17
Peri. TEFF
Peri. TH1
Peri. TREG
LN TFH
LN TREG
Prolif.
UMAP2
UMAP1
e
Copy numbers
0
20
40
60
80
1 2 3 4 5 6 7 8 9 10 11 12 13 14 15 16 17 18 19 20
Ranked TCR clones
Cluster distribution (%)
0
50
100
TFH
TREG
TH17/Prolif.
TEFF/TH1
12 4 14 15 16 20 1 2 3 5 6 7 9 11 8 10 13 17 18 19
Clonotypes (Rank)
LN Naive
LN nTREG
LN mixed
LN TFH
LN TREG
Prolif.
LN TH17
LN TCM
Peri TREG
Peri TH1
Peri TEFF
Peri TH17
Peri Tγδ
f
TFH
TREG
TH17/Proliferating
TH1/TEFF
n=10
n=26
n=79
n=13
UMAP2
UMAP1
g
Cd44
Icos
Tnfrsf4 (OX40)
Maf
0 1 2 3
0 1 2 3 4
0 1 2 3 4 5
0 1 2 3
h
Ifng
Tnf
Il17a
Il17f
Il21
Il4
Il10
Il2
0 1 2 3 4
0 1 2 3 4
0 1 2 3 4 5
0 1 2 3 4
0 1 2
0 1 2 3
0 1 2 3
0 1 2 3 4
Ccl5
Cd40lg
Fasl
Prf1
Gzma
Gzmb
Gzmk
Nkg7
0 2 4 6
0 1 2 3 4
0 1 2
0 1 2
0 1 2 3 4 5
0 1 2 3 4 5
0 1 2 3 4
0 1 2 3 4
UMAP2
UMAP1

**Figure 2**

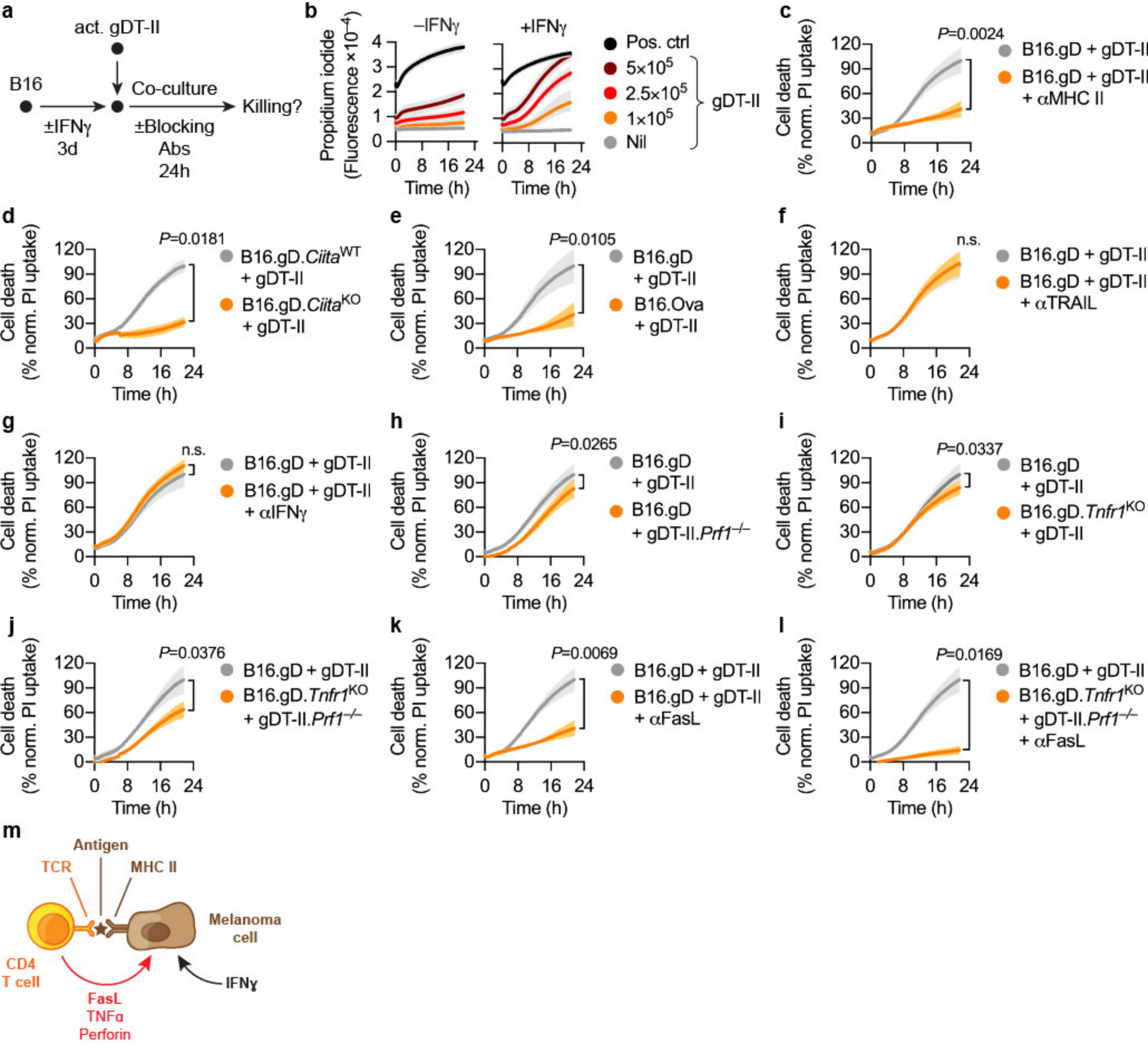
a
act. gDT-II
B16
±IFNγ
3d
Co-culture
±Blocking
Abs
24h
Killing?
b
−IFNγ
+IFNγ
Propidium iodide
(Fluorescence ×10−4)
Time (h)
Pos. ctrl
5×10⁵
2.5×10⁵
1×10⁵
Nil
gDT-II
c
P=0.0024
Cell death
(% norm. PI uptake)
B16.gD + gDT-II
B16.gD + gDT-II
+ αMHC II
d
P=0.0181
B16.gD.Ciita WT
+ gDT-II
B16.gD.Ciita KO
+ gDT-II
e
P=0.0105
B16.gD
+ gDT-II
B16.Ova
+ gDT-II
f
n.s.
B16.gD + gDT-II
B16.gD + gDT-II
+ αTRAIL
g
n.s.
B16.gD + gDT-II
B16.gD + gDT-II
+ αIFNγ
h
P=0.0265
B16.gD
+ gDT-II
B16.gD
+ gDT-II.Prf1−/−
i
P=0.0337
B16.gD
+ gDT-II
B16.gD.Tnfr1 KO
+ gDT-II
j
P=0.0376
B16.gD + gDT-II
B16.gD.Tnfr1 KO
+ gDT-II.Prf1−/−
k
P=0.0069
B16.gD + gDT-II
B16.gD + gDT-II
+ αFasL
l
P=0.0169
B16.gD + gDT-II
B16.gD.Tnfr1 KO
+ gDT-II.Prf1−/−
+ αFasL
m
Antigen
TCR
MHC II
Melanoma
cell
CD4
T cell
FasL
TNFα
Perforin
IFNγ

Figure 3

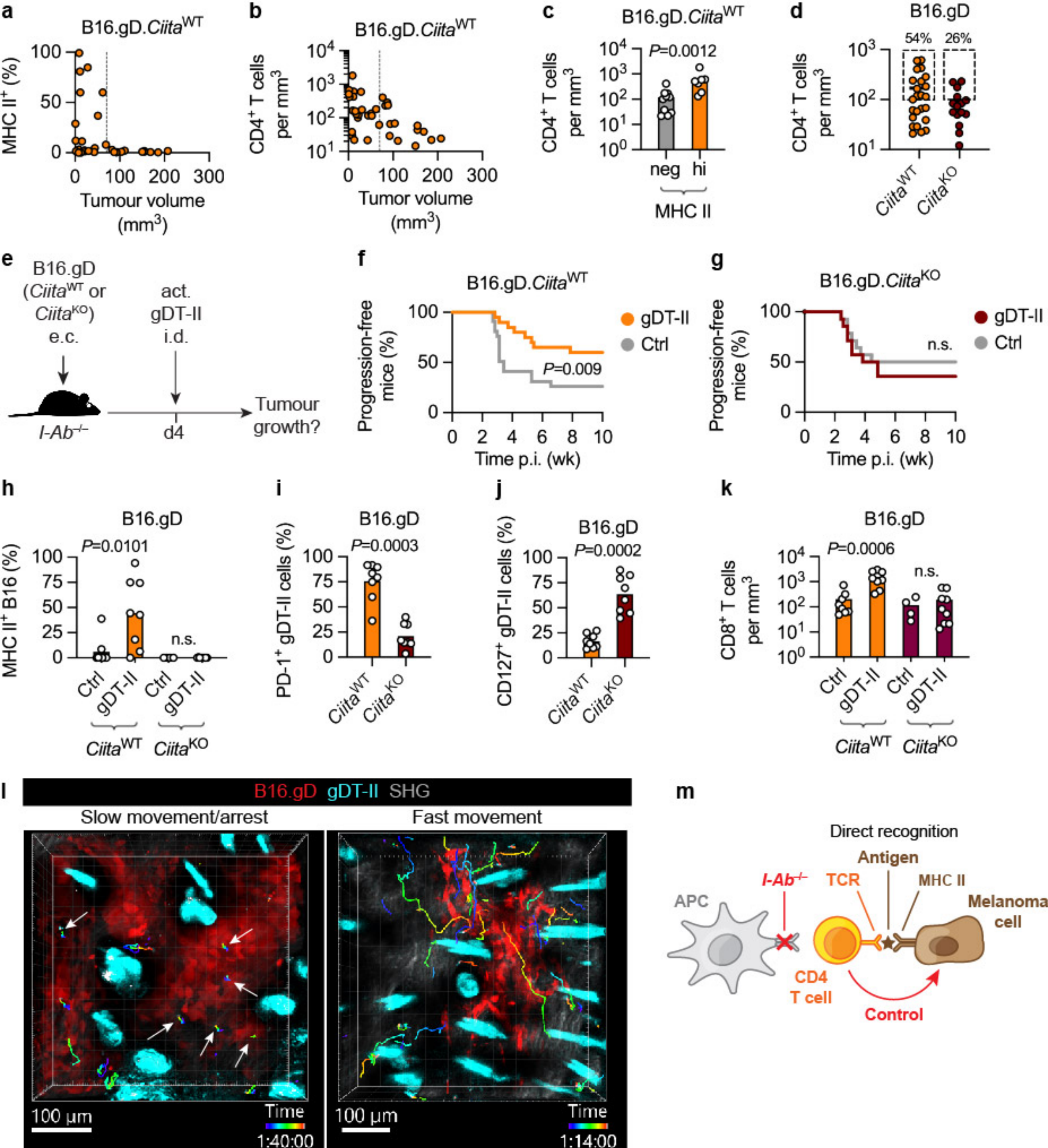
a
B16.gD.$Ciita^{WT}$
MHC II+ (%)
100
50
0
0
100
200
300
Tumour volume (mm3)
b
B16.gD.$Ciita^{WT}$
CD4+ T cells per mm3
$10^4$
$10^3$
$10^2$
$10^1$
0
100
200
300
Tumor volume (mm3)
c
B16.gD.$Ciita^{WT}$
CD4+ T cells per mm3
$P$=0.0012
$10^4$
$10^3$
$10^2$
$10^1$
$10^0$
neg
hi
MHC II
d
B16.gD
CD4+ T cells per mm3
54%
26%
$10^3$
$10^2$
$10^1$
$Ciita^{WT}$
$Ciita^{KO}$
e
B16.gD ($Ciita^{WT}$ or $Ciita^{KO}$) e.c.
act. gDT-II i.d.
$I\text{-}Ab^{-/-}$
d4
Tumour growth?
f
B16.gD.$Ciita^{WT}$
Progression-free mice (%)
100
50
0
gDT-II
Ctrl
$P$=0.009
0
2
4
6
8
10
Time p.i. (wk)
g
B16.gD.$Ciita^{KO}$
Progression-free mice (%)
100
50
0
gDT-II
Ctrl
n.s.
0
2
4
6
8
10
Time p.i. (wk)
h
B16.gD
MHC II+ B16 (%)
$P$=0.0101
100
75
50
25
0
n.s.
Ctrl
gDT-II
Ctrl
gDT-II
$Ciita^{WT}$
$Ciita^{KO}$
i
B16.gD
PD-1+ gDT-II cells (%)
$P$=0.0003
100
75
50
25
0
$Ciita^{WT}$
$Ciita^{KO}$
j
B16.gD
CD127+ gDT-II cells (%)
$P$=0.0002
100
75
50
25
0
$Ciita^{WT}$
$Ciita^{KO}$
k
B16.gD
CD8+ T cells per mm3
$P$=0.0006
n.s.
$10^4$
$10^3$
$10^2$
$10^1$
$10^0$
Ctrl
gDT-II
Ctrl
gDT-II
$Ciita^{WT}$
$Ciita^{KO}$
l
B16.gD gDT-II SHG
Slow movement/arrest
Fast movement
100 µm
Time
1:40:00
100 µm
Time
1:14:00
m
Direct recognition
Antigen
$I\text{-}Ab^{-/-}$
TCR
MHC II
APC
Melanoma cell
CD4 T cell
Control

Figure 4

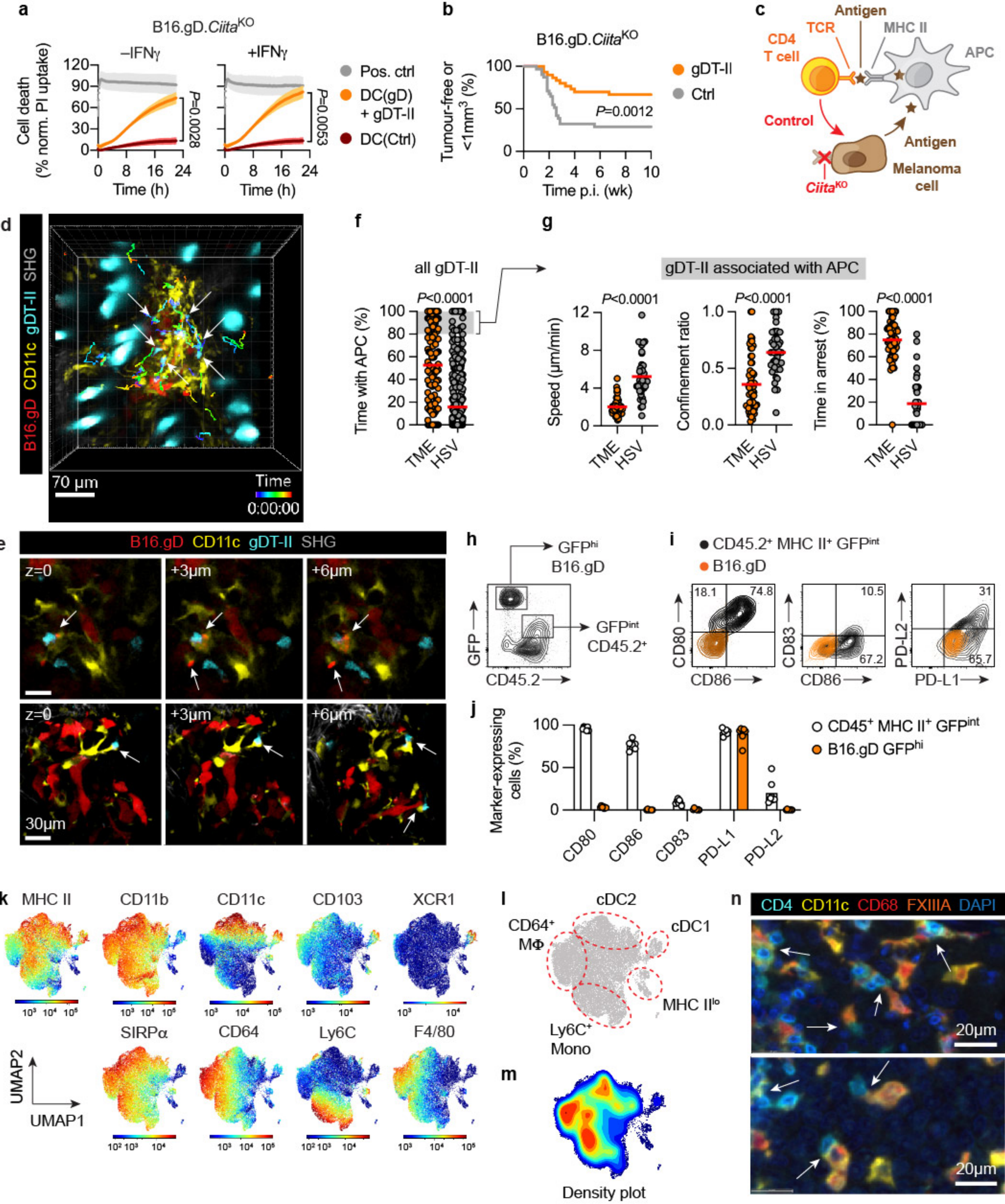
a
B16.gD.CiitaKO
–IFNγ
+IFNγ
Cell death (% norm. PI uptake)
120
90
60
30
0
0 8 16 24
Time (h)
P=0.0028
P=0.0053
Pos. ctrl
DC(gD) + gDT-II
DC(Ctrl)
b
B16.gD.CiitaKO
Tumour-free or <1mm3 (%)
100
50
0
0 2 4 6 8 10
Time p.i. (wk)
P=0.0012
gDT-II
Ctrl
c
Antigen
TCR
MHC II
CD4 T cell
APC
Control
Antigen
Melanoma cell
CiitaKO
d
B16.gD CD11c gDT-II SHG
70 µm
Time
0:00:00
e
B16.gD CD11c gDT-II SHG
z=0
+3µm
+6µm
30µm
f
all gDT-II
P<0.0001
Time with APC (%)
100
80
60
40
20
0
TME HSV
g
gDT-II associated with APC
P<0.0001
Speed (µm/min)
12
8
4
0
TME HSV
P<0.0001
Confinement ratio
1.0
0.5
0.0
TME HSV
P<0.0001
Time in arrest (%)
100
80
60
40
20
0
TME HSV
h
GFPhi B16.gD
GFPint CD45.2+
GFP
CD45.2
i
CD45.2+ MHC II+ GFPint
B16.gD
18.1
74.8
CD80
CD86
10.5
67.2
CD83
CD86
31
65.7
PD-L2
PD-L1
j
Marker-expressing cells (%)
100
50
0
CD80
CD86
CD83
PD-L1
PD-L2
CD45+ MHC II+ GFPint
B16.gD GFPhi
k
MHC II
CD11b
CD11c
CD103
XCR1
SIRPα
CD64
Ly6C
F4/80
UMAP2
UMAP1
10³ 10⁴ 10⁵
10² 10³ 10⁴
l
cDC2
CD64+ MΦ
cDC1
MHC IIlo
Ly6C+ Mono
m
Density plot
n
CD4 CD11c CD68 FXIIIA DAPI
20µm
20µm

Figure 5

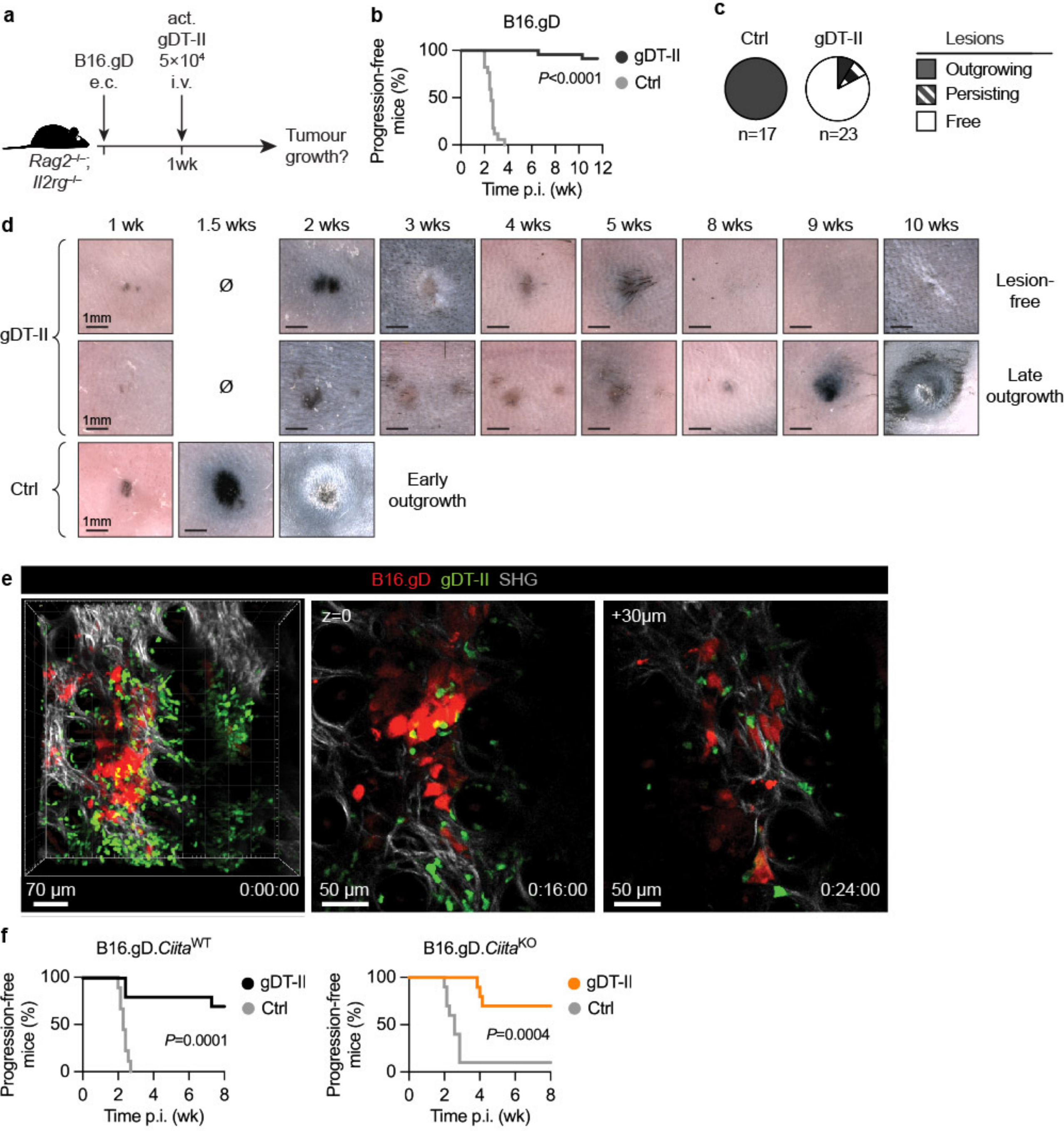
a
B16.gD
e.c.
act.
gDT-II
5×10⁴
i.v.
Rag2−/−;
Il2rg−/−
1wk
Tumour
growth?
b
B16.gD
Progression-free mice (%)
100
50
0
0 2 4 6 8 10 12
Time p.i. (wk)
P<0.0001
● gDT-II
● Ctrl
c
Ctrl
gDT-II
n=17
n=23
Lesions
Outgrowing
Persisting
Free
d
1 wk
1.5 wks
2 wks
3 wks
4 wks
5 wks
8 wks
9 wks
10 wks
gDT-II
Ctrl
Ø
1mm
Lesion-free
Late outgrowth
Early outgrowth
e
B16.gD gDT-II SHG
z=0
+30μm
70 μm
0:00:00
50 μm
0:16:00
50 μm
0:24:00
f
B16.gD.Ciita^WT
B16.gD.Ciita^KO
Progression-free mice (%)
100
50
0
0 2 4 6 8
Time p.i. (wk)
● gDT-II
● Ctrl
P=0.0001
P=0.0004

Figure 6

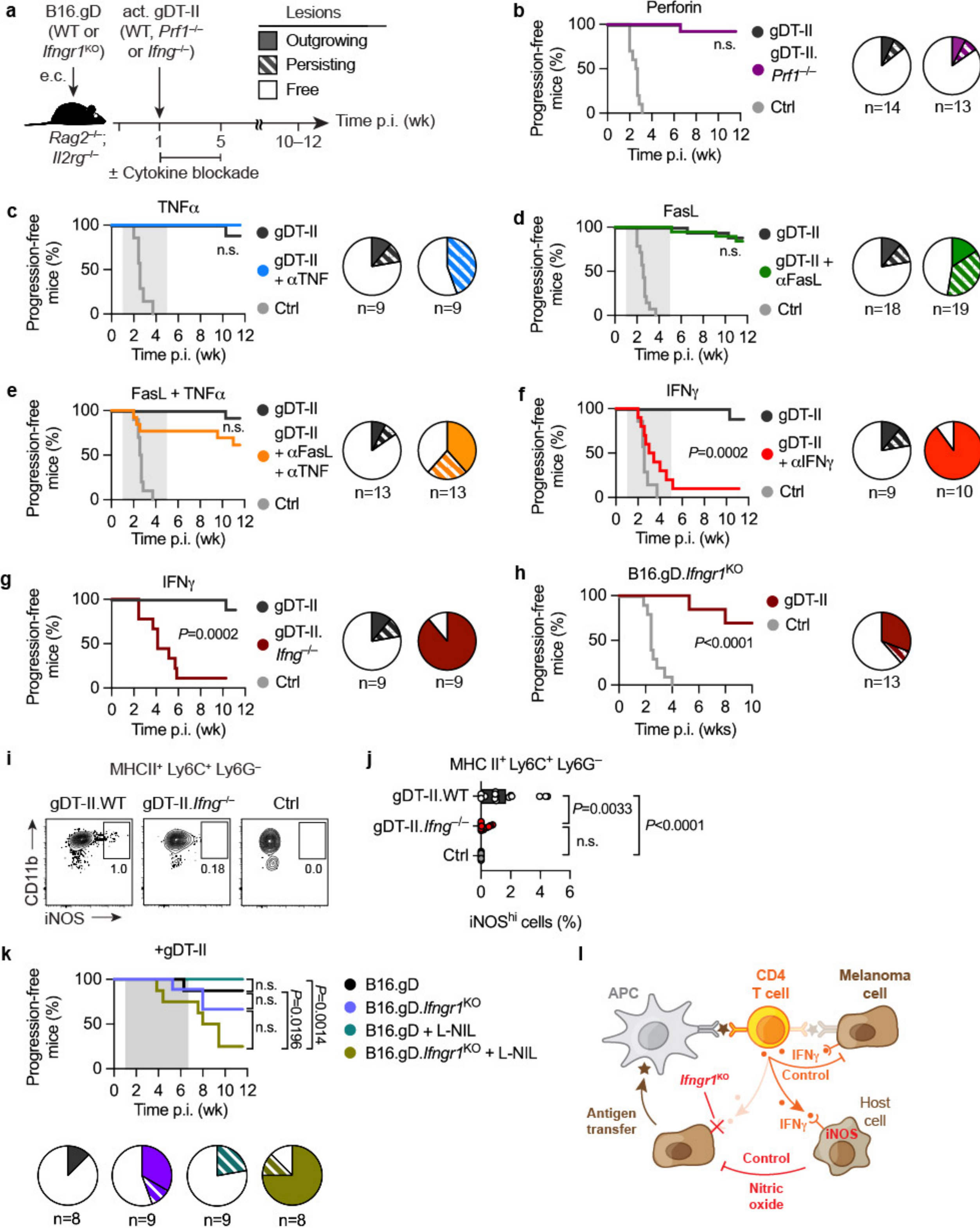
a
B16.gD (WT or Ifngr1KO)
e.c.
act. gDT-II (WT, Prf1−/− or Ifng−/−)
Lesions
Outgrowing
Persisting
Free
Rag2−/−; Il2rg−/−
1
5
10–12
Time p.i. (wk)
± Cytokine blockade
b
Perforin
Progression-free mice (%)
n.s.
gDT-II
gDT-II. Prf1−/−
Ctrl
Time p.i. (wk)
n=14
n=13
c
TNFα
n.s.
gDT-II
gDT-II + αTNF
Ctrl
n=9
n=9
d
FasL
n.s.
gDT-II
gDT-II + αFasL
Ctrl
n=18
n=19
e
FasL + TNFα
n.s.
gDT-II
gDT-II + αFasL + αTNF
Ctrl
n=13
n=13
f
IFNγ
P=0.0002
gDT-II
gDT-II + αIFNγ
Ctrl
n=9
n=10
g
IFNγ
P=0.0002
gDT-II
gDT-II. Ifng−/−
Ctrl
n=9
n=9
h
B16.gD.Ifngr1KO
P<0.0001
gDT-II
Ctrl
Time p.i. (wks)
n=13
i
MHCII+ Ly6C+ Ly6G−
gDT-II.WT
gDT-II.Ifng−/−
Ctrl
1.0
0.18
0.0
CD11b
iNOS
j
MHC II+ Ly6C+ Ly6G−
gDT-II.WT
gDT-II.Ifng−/−
Ctrl
P=0.0033
n.s.
P<0.0001
iNOShi cells (%)
k
+gDT-II
n.s.
n.s.
n.s.
P=0.0196
P=0.0014
B16.gD
B16.gD.Ifngr1KO
B16.gD + L-NIL
B16.gD.Ifngr1KO + L-NIL
n=8
n=9
n=9
n=8
l
APC
CD4 T cell
Melanoma cell
IFNγ
Control
Ifngr1KO
Antigen transfer
Host cell
IFNγ
iNOS
Control
Nitric oxide

**Figure 7**

## List of Supplementary Materials

1. Supplementary Materials & Methods
2. Supplementary Figures
3. Supplementary Tables
4. Movie legends

## Supplementary Materials & Methods

**Cell engineering with CRISPR-Cas9.** DNA sequences targeting the genes *Ciita* (CACCGACTGGATGAAGAGACCCGGG) or *Tnfr1* (CACCGATGGGGATACATCCATCAG) were cloned into the plasmid pSpCas9(BB)-2A-Puro (PX459) version 2.0 (Addgene plasmid #62988, a gift from Feng Zhang) to generate plasmids, PX459-*Ciita* and PX459-*Tnfr1*, respectively. To generate the B16.gD.*Ciita*$^{KO}$ cell line and the respective control cell line, B16.gD.*Ciita*$^{WT}$, B16.gD were transfected using FuGENE® HD transfection reagent according to the manufacturer's instructions with either PX459-*Ciita* or PX459, respectively. Cells were selected by puromycin (2µg/mL) for 3d and subsequently treated with IFNɣ (1000U/mL) for 3d and sorted on MHC II-negative cells (B16.gD.*Ciita*$^{KO}$) or total cells (B16.gD.*Ciita*$^{WT}$) by flow cytometry using an Aria III (BD). Routine functional validation with IFNɣ treatment demonstrated <6% of cells in the B16.gD.*Ciita*$^{KO}$ cell line expressed MHC II when >98% of B16.gD.*Ciita*$^{WT}$ expressed MHC II under the same culture conditions. To generate B16.gD.*Tnfr1*$^{KO}$, the B16.gD cell line was transfected using FuGENE® HD transfection reagent according to the manufacturer's instructions with the PX459-*Tnfr1* plasmid. Cells were selected by puromycin (2µg/mL) for 3d. Cells with successful *Tnfr1* gene disruption were further enriched through combined treatment of IFNɣ (500U/mL) and TNFα (1000U/mL) for 3d, which was sufficient to kill all mock-transfected cells. Next generation sequencing (MiSeq) validated that out-of-frame genetic disruption of *Tnfr1* occurred in 94% of cells in the B16.gD.*Tnfr1*$^{KO}$ cell line.

The B16.gD.*Ifngr1*$^{KO}$ cell line was generated using the 4D-Nucleofector system (Lonza) with single guide RNA targeting murine *Ifngr1* (AUUAGAACAUUCGUCGGUAC). RNA was purchased from Synthego and reconstituted in nuclease-free water (Synthego). Nucleofection was performed using the P3 Primary Cell 4D-Nucleofector X Kit S (Lonza) according to the manufacturer's recommended protocol for mouse T cells. Briefly, B16.gD were harvested using 1 × trypsin/EDTA solution (Sigma), washed twice in phosphate buffered saline (PBS) and $1\times10^5$ cells and were resuspended in reaction buffer (P3 Primary Cell Nucleofector solution + Supplement 1 (4.5:1), Lonza). Single guide RNA (~0.3nmol) and 10µg of Recombinant S. pyogenes Cas9 nuclease (Integrated DNA Technologies) were added to the suspension and cells were transfected in one well of a 16-well Nucleocuvette Strip (Lonza) using the program CM 137 on a 4D-Nucleofector X Unit (Lonza). Cells with successful *Ifngr1* gene deletion were purified by sorting on MHC I-negative cells by flow cytometry on an Aria III (BD) following treatment with IFNɣ (500U/mL) for 2d (at which time >99% of the parental cell line expressed MHC I).

**Flow cytometry.** Single-cell suspensions from spleens or LNs were generated by pressing organs through a fine metal sieve. Tumours or skin ($1\times1cm^2$) were finely chopped, incubated in 3mg/mL Collagenase Type III (Worthington) for 90min in a 37°C water bath and further homogenised by pipetting up and down in RP-10. Cell suspensions were filtered through 70µm mesh and stained for

45min on ice with anti-mouse antibodies. All antibodies used for staining are listed in Supplementary Table S1. For intracellular staining, cells were fixed and permeabilized using a Foxp3/transcription-factor-staining buffer kit (eBioscience) according to the manufacturer's instructions. For assessment of cell proliferation, naïve gDT-II were stained using Life Technologies CellTrace Violet cell proliferation kit (Invitrogen) according to the manufacturer's instructions. DAPI (4',6-diamidino-2-phenylindole, dihydrochloride, Invitrogen) or fixable LIVE/DEAD near-infrared or blue cell-staining kit (BD Biosciences) or Zombie Aqua fixable viability kit (Biolegend) were used to determine cell viability. SPHERO blank calibration particles (BD pharmingen) were used for calculation of cell numbers. Samples were run on a BD Fortessa (BD Biosciences) or an NL3000 Aurora (Cytek). Fluorescence-activated cell sorting was performed with an Aria III (BD Biosciences). Data was analysed using FlowJo v10.8.2 (BD Biosciences) and in OMIQ (Dotmatics). For analysis in OMIQ, populations of interest were first exported as FCS files from FlowJo, subsampling was performed using a maximum equal distribution, dimension reduction was executed using FlowSOM with the following parameters; xdim 10, ydim 10, number of iterations 10, Euclidean distance metric, Random seed 2332 and UMAP was run with the following parameters; neighbours 15, minimum distance 0.4, components 2, Euclidean distance metric, learning rate 1, epochs 200, random seed 2000, spectral embedding initialisation.

**Histology on mouse tissue.** Skin was harvested from mice and fixed for 24h in IHC zinc-fixative (BD Pharmingen). The fixed tissue was paraffin embedded and the tissue was cut into 4µm sections onto glass slides. Haematoxylin and Eosin (H&E) staining was carried out using a Leica AutoStainer XL. Coverslips were added (Leica CV5030 Coverslipper) and tissue sections were scanned using the Pannoramic SCAN II scanner (3DHISTECH Ltd.).

***In vitro* differentiation of bone marrow-derived DCs.** Bone marrow was collected from WT mice. Following red blood cell lysis (Sigma), cells were resuspended and cultured at $1.5\times10^6$ cells/mL in RPMI supplemented with 10% FCS, 0.2g/L streptomycin, 100U/mL penicillin, 90µM 2-β-mercaptoethanol, 1.32mM L-glutamine and 150ng/mL of human Flt3L (BioXCell) for 8d at 37 °C, 5.2% $CO_2$. Bone marrow-derived DCs (BMDCs) were ~50% MHC II$^+$, ~95% CD11b$^+$ and ~80% CD11c$^+$ (determined by flow cytometry) when used in *in vitro* assays.

***In vivo* bioluminescence imaging.** For *in vivo* bioluminescence imaging mice were e.c. inoculated with B16.gD.Luc and injected i.p. with 150mg/kg of D-luciferin potassium salt (VivoGlo, Promega) dissolved in PBS. Mice were anaesthetized with isoflurane (3.5%) vaporized at an 80:20 mixture of $O_2$ and air. The left flank of the mice was shaved and depilated using Veet. Five min after injection of D-luciferin, mice were imaged at an exposure time of 300s. Bioluminescence was measured using the IVIS Lumina XRMS Series III imaging system (PerkinElmer). Images were analysed with Living Image (v4.4.5) software. Bioluminescence signals were measured at the site of tumour inoculation and calculated as total flux (photons [p]/s).

**Human melanoma cohorts.** Samples analyzed in this study were obtained from previously published cohorts[49–51]. Samples shown in Fig.5n were from immunotherapy treatment naïve patients whose melanoma tissues were obtained for the Australian Melanoma Genome Project (AMGP) (n=183) (refs[49,50]). Samples shown in Fig.S7i,k,m results were obtained from primary melanoma excisions, [51] comprised of treatment naïve patients diagnosed with primary melanoma between 2003 and 2007 (n=28). Tissue for both cohorts was sourced from the Melanoma Institute Australia Biospecimen bank. All tissue was acquired for research with approval from the Sydney Local Health District Human Ethics Review Committee (protocol no X15-0454 & 2019/ETH06874), and informed consent from each patient and from the MIA Biospecimen Tissue Bank.

**Multiplex fluorescent immunohistochemistry (mIHC) on human tissue.** FFPE tissue sections were stained utilizing mIHC panels that were optimized according to the protocol detailed by Yaseen et al. ([77]). Multiplex fluorescent immunohistochemistry was performed as previously described for two separate panels (CD103, FoxP3, CD8, CD3, HLA-DR, SOX10) and (FXIIIA, CD11c, CD20, CD68, SOX10, CD4) [49–51]. Detailed staining information is available in Supplementary Tables S2 and S3. Single color control, multiplex control and unstained control slides were stained alongside patient samples to determine background staining and create a spectral library for imaging and spectral unmixing.

**Multispectral imaging of human tissue.** Whole tissue sections and tumour microarray cores were imaged at 20× resolution (0.5µm/pixel) using the DAPI, FITC, Cy3, Texas Red and Cy5 channels on a Vectra 3.0.5 Automated Quantitative Pathology Imaging system (Akoya Biosciences). Inform v2.4.2 (Akoya Biosciences) was used for spectral unmixing based on a library created from single color controls. For the primary cohort, 20× resolution images were aligned and stitched into a single image for each patient's tumor.

**Image analysis for mIHC.** Tissue and cell segmentation image analysis was performed using HALO v3.0.1 (Indica Labs). Tissue classification was performed using a trained Random Forest algorithm to classify tissue as either tumor, stroma, or empty slide. Cell segmentation detected cell nuclei using an algorithm trained based on the intensity of DAPI or SOX10 staining. Positivity thresholds were set and reviewed individually for each sample based on cytoplasmic or nuclear staining intensity for each marker. Data for each cell's marker expression and X, Y location were stored in HALO and exported for phenotyping and, for the primary cohort, further spatial analysis in SPIAT. In the primary cohort APCs were defined as HLA-DR$^{+}$SOX10$^{-}$CD3$^{-}$, CD8$^{+}$ T cells were defined as CD3$^{+}$CD8$^{+}$SOX10$^{-}$, CD8$^{-}$ T cells were defined as CD3$^{+}$CD8$^{-}$SOX10$^{-}$, and melanoma cells were defined as SOX10$^{+}$. All phenotypes were additionally defined as DAPI$^{+}$, and cells in both the tumor and stroma were analyzed. Nearest neighbor spatial analysis for mIHC was performed for the 25 (of 28) samples for which spatial data was generated, using the SPIAT package v.1.2.3 in R v.4.3.1 (ref[78]). Nearest neighbor distances between APC/CD8$^{-}$ T cells, HLA-DR$^{+}$ melanoma/CD8$^{-}$ T cells, and simultaneous APC/CD8$^{-}$ & APC/CD8$^{+}$ were calculated using the *calculate_minimumdistances_between_cell_types* function in SPIAT (Fig. S7j,l,o). Cells within 20 µm of each other were defined as interacting. The 20 µm cutoff for cellular interaction was selected based on analysis from previous studies[51,79] and visual inspection. All spatial analysis data was exported for statistical analysis.

**Generation of bone-marrow chimeric mice.** B6.albino mice were lethally irradiated (2×550rad, 3h), transferred T cell depleted bone marrow cells from CD11c.YFP mice (1–4×$10^6$ i.v.) and allowed to reconstitute for at least 8wks prior to experiments.

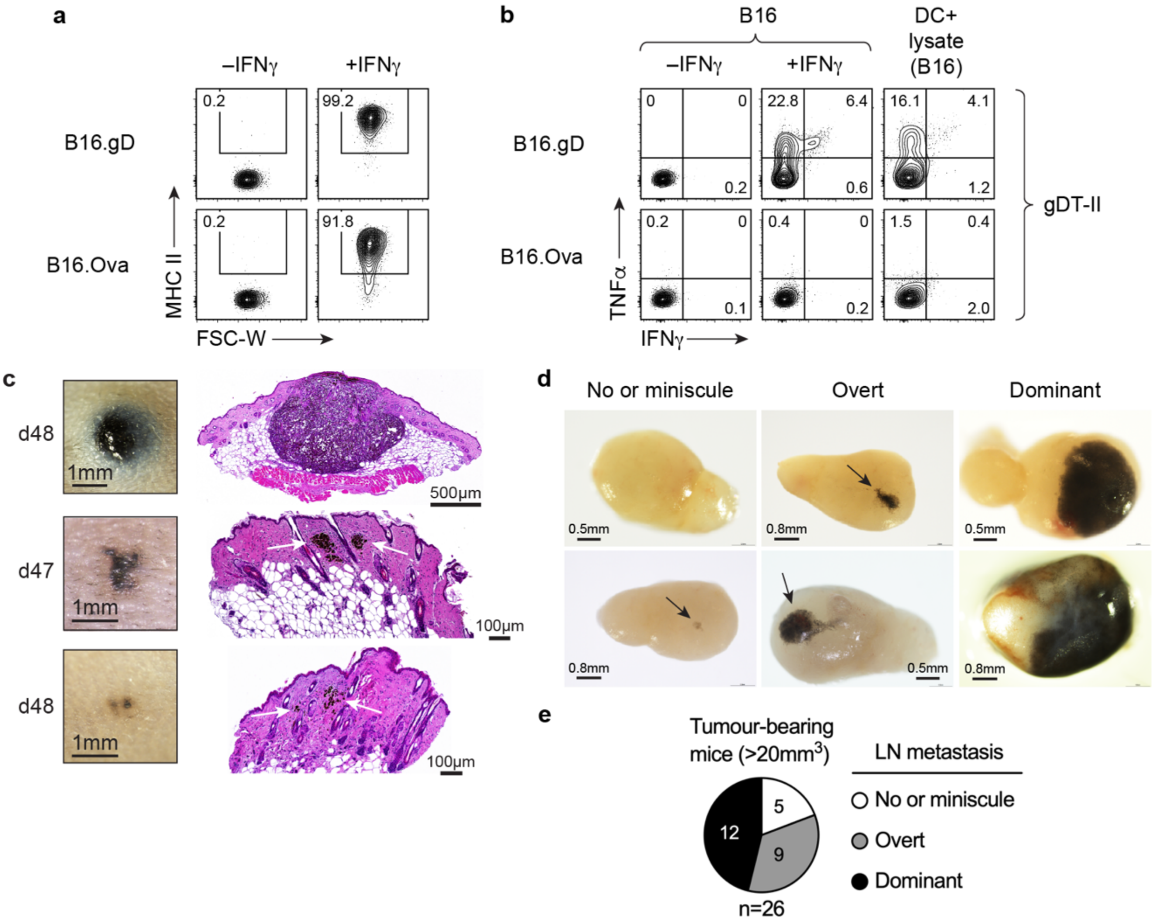

**Figure S1. B16 cell lines, tumour outcomes and LN metastasis. a,** Representative flow cytometry plots of MHC II expression by B16.gD or B16.Ova with (right) or without (left) treatment with IFNɣ for 3d *in vitro*. **b,** Production of IFNɣ and TNFα by *in vitro* activated gDT-II following 5h coculture with either B16.gD or B16.Ova cells alone (with or without IFNɣ pretreatment) or with BMDC pulsed with corresponding B16 cell lysates. **a**+**b**, Data from a single experiment, representative of 3 independent experiments. **c,** Dermoscopic photos and corresponding H&E staining of tumours from WT mice e.c. inoculated with B16.gD. **d+e,** Incidence of metastasis in tumour-draining (brachial) LNs of WT mice e.c. inoculated with B16.gD bearing tumours >20mm$^3$. Metastases graded based on approximation of the surface area of black pigment observed; No or miniscule, <0.5mm$^2$; overt, 0.5–1.5mm$^2$; dominant >1.5mm$^2$. Representative photos (**d**) and pooled analysis (**e**) of metastasis from 8 independent experiments with 26 mice.

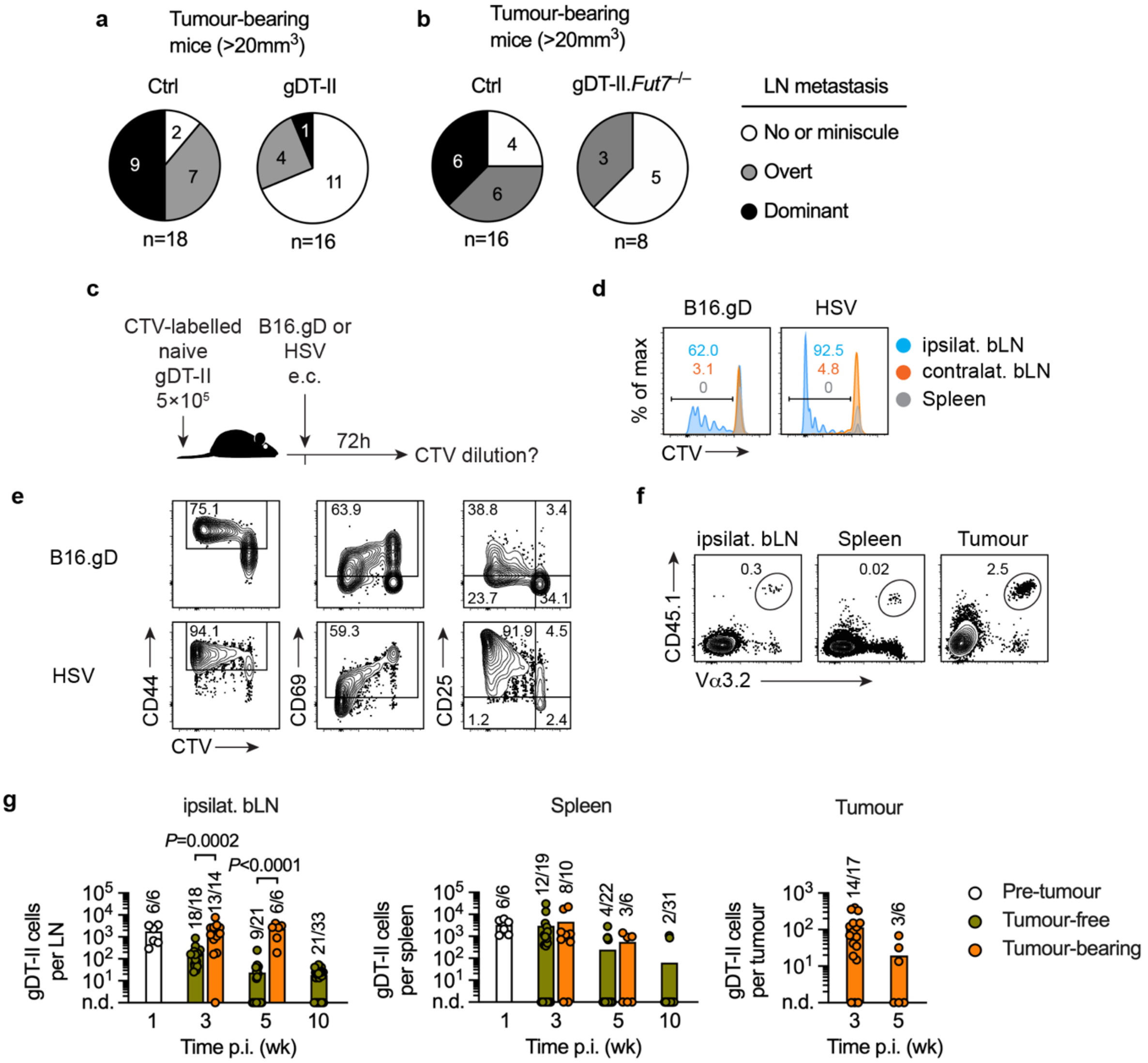

**Figure S2**

**Figure S2. gDT-II responses to B16.gD challenge. a+b,** Incidence of metastasis in the tumour-draining (brachial) LNs of WT mice bearing B16.gD tumours >20mm$^3$. Metastases graded based on approximation of the surface area of black pigment observed; no or miniscule, <0.5 mm$^2$; overt, 0.5–1.5 mm$^2$; dominant, >1.5 mm$^2$. **a**, Metastasis in mice that were i.v. transferred 1×10$^4$ naïve gDT-II (gDT-II), or did not receive gDT-II (Ctrl), prior to tumour challenge. Data pooled from 8 independent experiments with 18 (Ctrl) or 16 (gDT-II) mice. **b,** Metastasis in mice that were i.v. transferred 5×10$^4$ naïve gDT-II.*Fut7*$^{-/-}$(gDT-II.*Fut7*$^{-/-}$), or did not receive gDT-II (Ctrl), prior to tumour challenge. Data pooled from 3 independent experiments with 16 (Ctrl) or 8 (gDT-II.*Fut7*$^{-/-}$) mice. **c,** Schematic for experiments in **d**+**e**. WT mice received naïve CellTrace Violet (CTV)-labelled gDT-II (5×10$^5$, i.v.) 1d prior to e.c. inoculation with B16.gD or HSV-1. The ipsilateral (ipsilat. bLN) and contralateral (contralat. bLN) brachial LNs and spleens were harvested 72h p.i. and gDT-II analysed by flow cytometry. Data depicts individual mice, representative of 3 (HSV) or 8 (B16.gD) mice from 2 independent experiments. **d,** Histograms of CTV-labelled gDT-II from ipsilateral bLNs (blue), contralateral bLNs (orange) and spleens (grey). **e,** Analysis of CD44, CD69 and CD25 expression by CTV-labelled gDT-II from ipsilateral bLN. **f,** Representative flow cytometry plots depicting gating strategy for isolating gDT-II (Vα3.2$^+$CD45.1$^+$) pregated on single, DAPI$^-$CD45.2$^+$CD4$^+$ cells. **g,** Enumeration of gDT-II in indicated organs at different time points (wks p.i.) determined by flow cytometry. Fractions depict number of mice in which gDT-II were detected in the specified organ at each timepoint; n.d., not detected. Comparison of gDT-II numbers in bLN between tumour-free and tumour-bearing mice by Mann Whitney test.

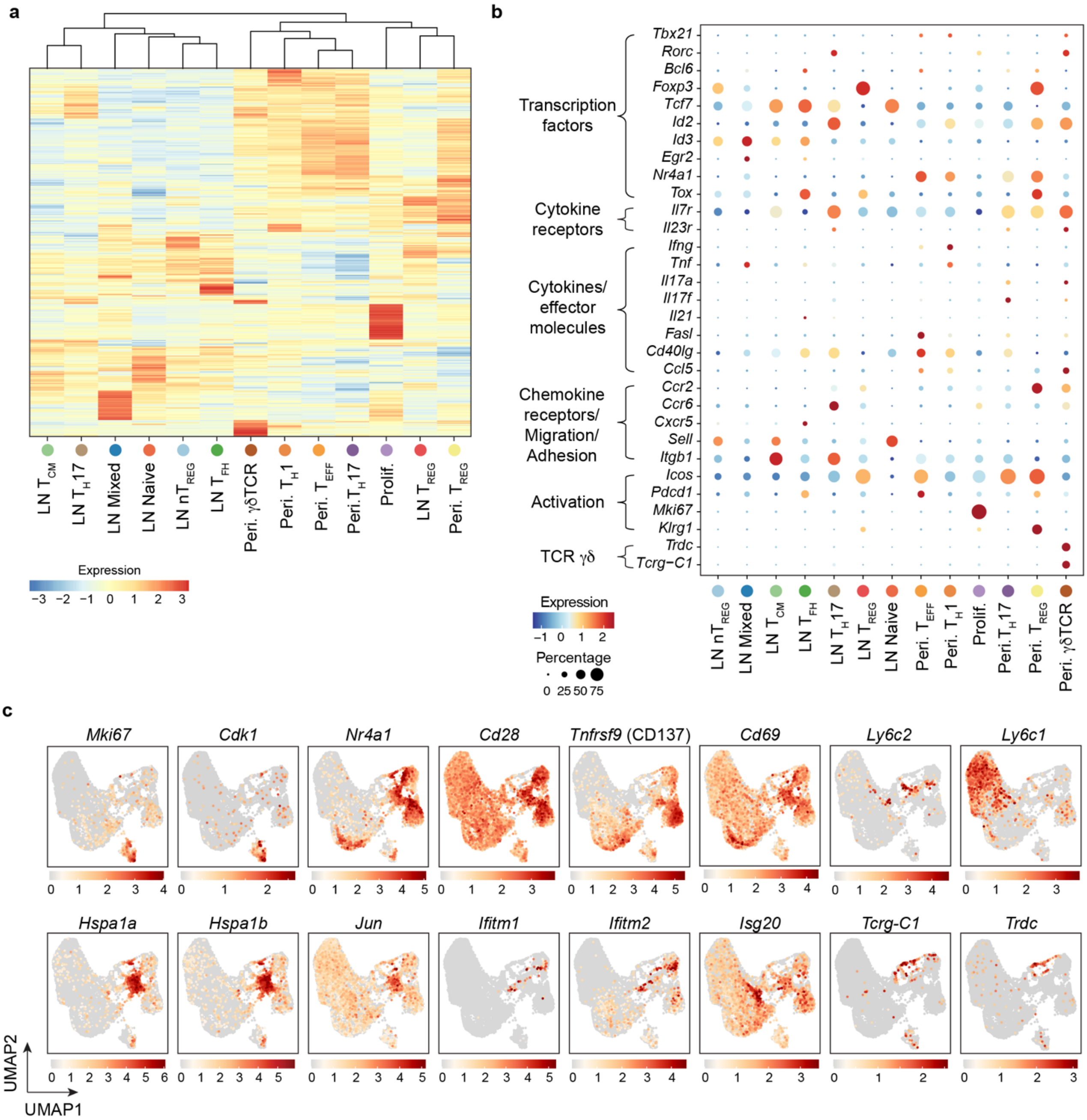

**Figure S3. Transcriptional analysis of CD4$^{+}$ T cells by single-cell RNA sequencing. a,** Heatmap of mean cluster relative expression (Z-score) of top 50 differentially expressed genes per cluster. **b,** Dot plot depicting mean cluster relative expression levels (Z-score) and percentage of cells expressing genes indicated. **c,** Normalised log2 expression values for indicated genes superimposed on UMAP described in Fig.2.

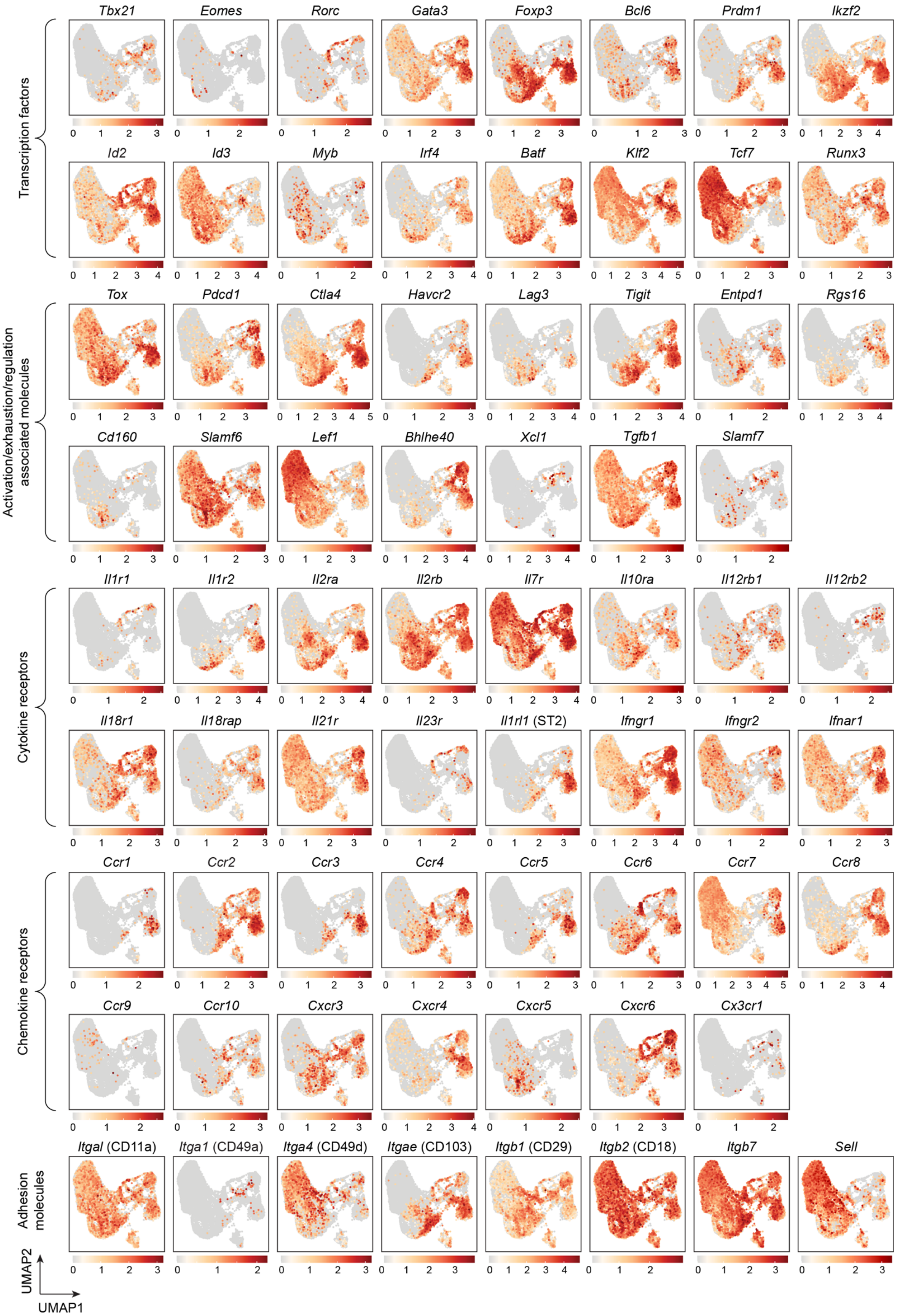
Transcription factors
Tbx21
Eomes
Rorc
Gata3
Foxp3
Bcl6
Prdm1
Ikzf2
Id2
Id3
Myb
Irf4
Batf
Klf2
Tcf7
Runx3
Activation/exhaustion/regulation associated molecules
Tox
Pdcd1
Ctla4
Havcr2
Lag3
Tigit
Entpd1
Rgs16
Cd160
Slamf6
Lef1
Bhlhe40
Xcl1
Tgfb1
Slamf7
Cytokine receptors
Il1r1
Il1r2
Il2ra
Il2rb
Il7r
Il10ra
Il12rb1
Il12rb2
Il18r1
Il18rap
Il21r
Il23r
Il1rl1 (ST2)
Ifngr1
Ifngr2
Ifnar1
Chemokine receptors
Ccr1
Ccr2
Ccr3
Ccr4
Ccr5
Ccr6
Ccr7
Ccr8
Ccr9
Ccr10
Cxcr3
Cxcr4
Cxcr5
Cxcr6
Cx3cr1
Adhesion molecules
Itgal (CD11a)
Itga1 (CD49a)
Itga4 (CD49d)
Itgae (CD103)
Itgb1 (CD29)
Itgb2 (CD18)
Itgb7
Sell
UMAP2
UMAP1

**Figure S4. Transcriptional analysis of $CD4^+$ T cells by single-cell RNA sequencing.** Normalised log2 expression values for indicated genes superimposed on UMAP described in Fig.2.

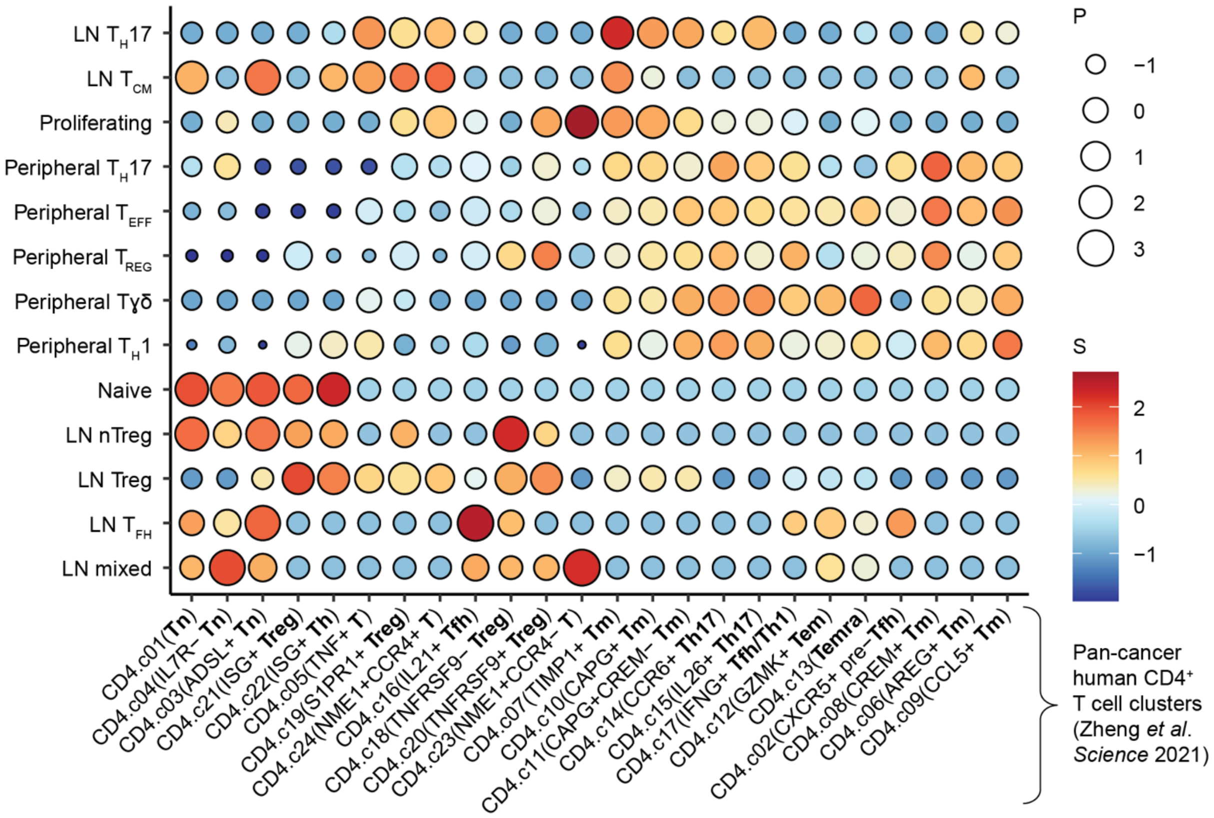

**Figure S5. Comparison of murine and human CD4⁺ T cell transcriptional signatures.** Heatmap of gene set enrichment analysis using differentiation states in Fig.2 and 24 gene signatures from human cancers published by Zheng *et al.* (ref[31]). Dot size depicts scaled -log10(*P* values) and fill colour depicts the proportion of signature genes in up-regulated genes (per differentiation state using roast rotation gene set test).

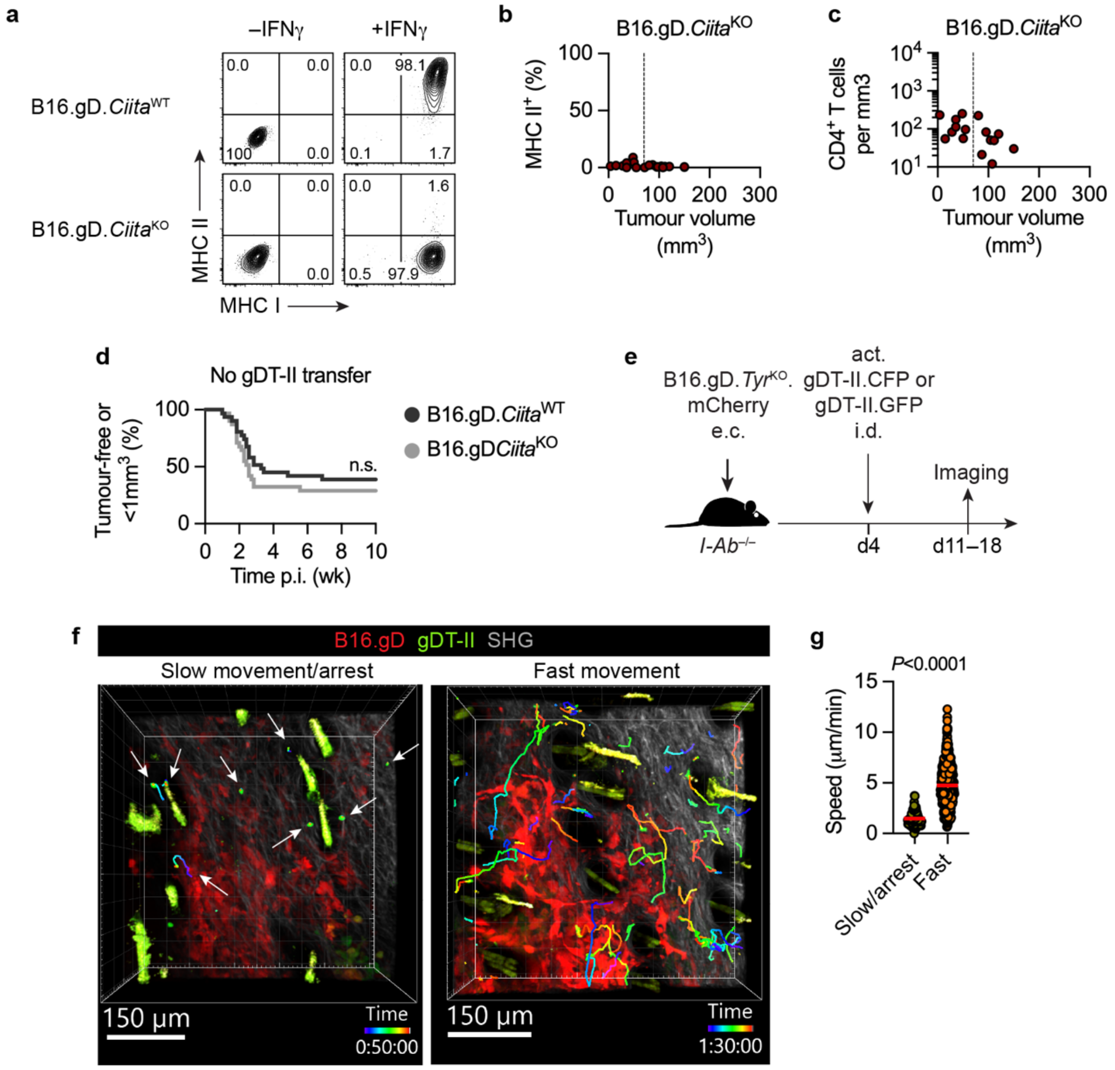

**Figure S6. Role of MHC II expression by melanoma cells for CD4$^+$ T cell immunity. a,** Representative flow cytometry plots of MHC I and MHC II expression by B16.gD.*Ciita*$^{\mathrm{WT}}$ or B16.gD.*Ciita*$^{\mathrm{KO}}$ with or without IFNɣ treatment for 3d *in vitro*. Data representative of >10 independent experiments. **b+c,** Flow cytometric analysis of tumours from WT mice (naïve or i.v. transferred 1×10$^4$ naïve gDT-II) e.c. inoculated with B16.gD.*Ciita*$^{\mathrm{KO}}$. **b,** Percentage of B16.gD.*Ciita*$^{\mathrm{KO}}$ that expressed MHC II versus tumour volume. **c,** Numbers of intratumoural CD4$^+$ T cells (CD45$^+$CD8$^-$CD4$^+$) versus tumour volume. Data pooled from 5 independent experiments with 20 (**b**) or 16 (**c**) mice. **d,** Proportion of tumour-free WT mice or mice with a lesion <1mm$^3$ e.c. challenged with B16.gD.*Ciita*$^{\mathrm{WT}}$ or B16.gD.*Ciita*$^{\mathrm{KO}}$. Data pooled from 4 independent experiments with 31 mice per group. Statistics by Log-rank Mantel–Cox test. **e,** Schematic of intravital 2-photon microscopy experiments with *I-Ab*$^{-/-}$ mice. *I-Ab*$^{-/-}$ mice were e.c. inoculated with B16.gD.*Tyr*$^{\mathrm{KO}}$.mCherry and i.d. transferred activated gDT-II.GFP or gDT-II.CFP (4×10$^6$) and imaged by 2-photon microscopy 11–18d p.i. **f,** Representative 2-photon microscopy images from the skin inoculation site in *I-Ab*$^{-/-}$ mice challenged with B16.gD.*Tyr*$^{\mathrm{KO}}$.mCherry e.c. (red) and i.d. transferred activated gDT-II.GFP (green). Images from movies (left, Movie S6; right, Movie S7) of 2 individual mice where gDT-II were either observed to move slowly or be arrested (left) or move quickly (right). Representative of 2 independent experiments with 7 mice. gDT-II tracks from the total imaging time (left, 50min; right, 1h 30min) of respective movies are superimposed on images. Time stamps represent h:min:s. Arrows point to tracks of cells which appear slow moving/arrested. SHG signal, white; autofluorescent hair, yellow/green. **g,** Average speed of gDT-II in 2-photon movies of *I-Ab*$^{-/-}$ mice stratified by movies in which gDT-II appear to be slow-moving/arrested or fast-moving. Data pooled from 2 independent experiments with 3 (slow/arrest) or 4 (fast) mice with n=71 (slow) and n=643 cells (fast). Statistics by two-sided Mann–Whitney test. Red lines depict means.

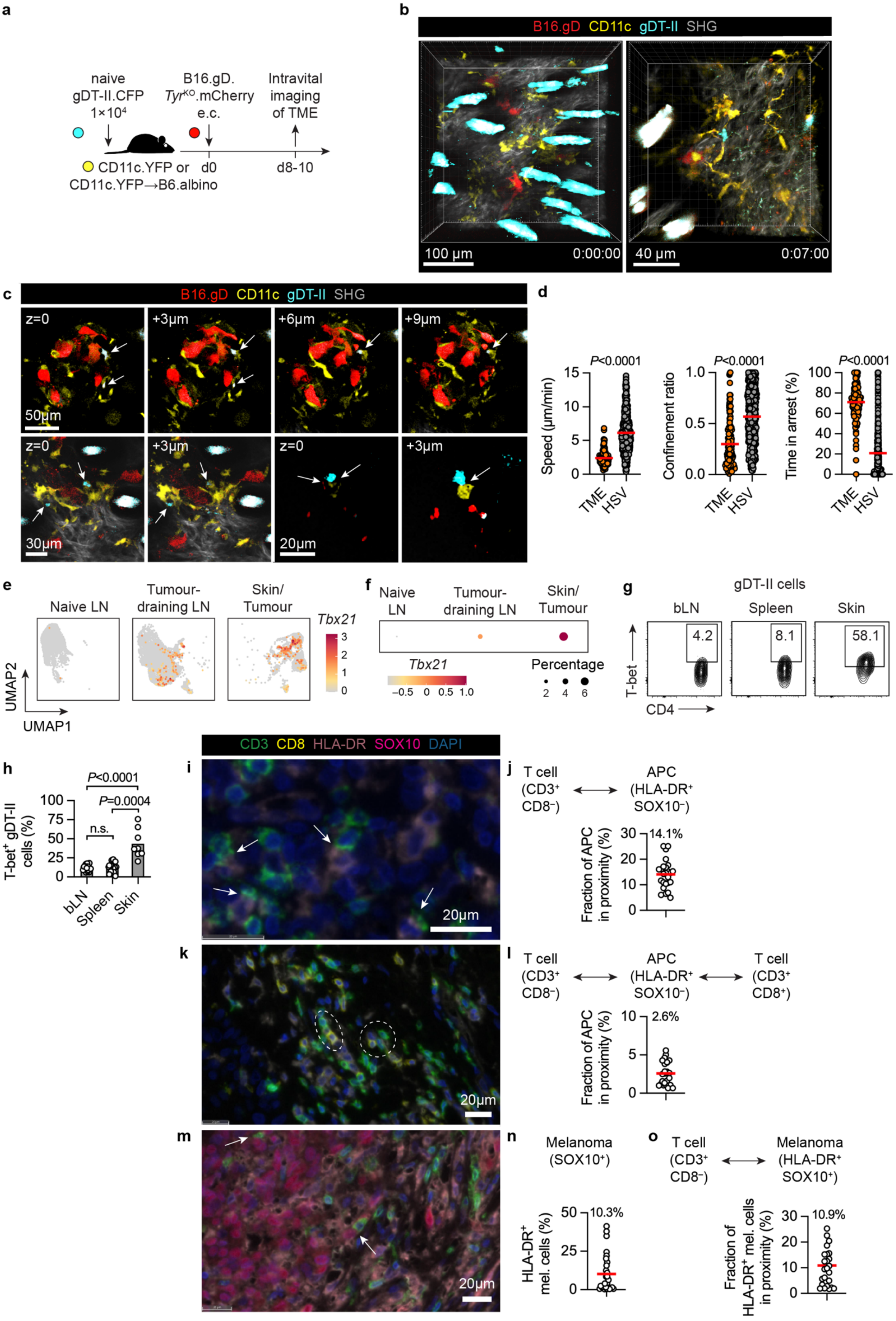
a
naive gDT-II.CFP 1×10⁴
CD11c.YFP or CD11c.YFP→B6.albino
B16.gD. TyrKO.mCherry e.c.
d0
Intravital imaging of TME
d8-10
b
B16.gD CD11c gDT-II SHG
100 µm
0:00:00
40 µm
0:07:00
c
B16.gD CD11c gDT-II SHG
z=0
+3µm
+6µm
+9µm
50µm
30µm
20µm
d
P<0.0001
Speed (µm/min)
Confinement ratio
Time in arrest (%)
TME
HSV
e
Naive LN
Tumour-draining LN
Skin/Tumour
Tbx21
UMAP2
UMAP1
f
Naive LN
Tumour-draining LN
Skin/Tumour
Tbx21
Percentage
g
gDT-II cells
bLN
Spleen
Skin
4.2
8.1
58.1
T-bet
CD4
h
T-bet⁺ gDT-II cells (%)
P<0.0001
P=0.0004
n.s.
bLN
Spleen
Skin
i
CD3 CD8 HLA-DR SOX10 DAPI
20µm
j
T cell (CD3⁺ CD8⁻)
APC (HLA-DR⁺ SOX10⁻)
Fraction of APC in proximity (%)
14.1%
k
20µm
l
T cell (CD3⁺ CD8⁻)
APC (HLA-DR⁺ SOX10⁻)
T cell (CD3⁺ CD8⁺)
Fraction of APC in proximity (%)
2.6%
m
20µm
n
Melanoma (SOX10⁺)
HLA-DR⁺ mel. cells (%)
10.3%
o
T cell (CD3⁺ CD8⁻)
Melanoma (HLA-DR⁺ SOX10⁺)
Fraction of HLA-DR⁺ mel. cells in proximity (%)
10.9%

**Figure S7. Interaction between APC and CD4$^+$ T cells in the TME. a,** Schematic for 2-photon imaging experiments of the TME in **b**–**d** and Fig.5d–g. CD11c.YFP or CD11c.YFP→B6.albino chimeric mice were i.v. transferred naïve gDT-II.CFP (1×10$^4$) 1d prior to e.c. inoculation with B16.gD.*Tyr*$^{KO}$.mCherry and skin inoculation sites imaged by 2-photon microscopy 7–10d p.i. **b**+**c,** Representative 2-photon microscopy images depicting gDT-II.CFP (cyan), CD11c.YFP (yellow) and B16.gD.*Tyr*$^{KO}$.mCherry (red) cells. SHG signal, white; autofluorescent hair, white/cyan. Data representative of 4 independent experiments with 15 mice (CD11c.YFP or CD11c.YFP→B6.albino chimeric). **b**, Images from CD11c.YFP→B6.albino chimeric mice corresponding to Movie S9 (left) and Movie S10 (right). Time stamps represent h:min:s. **c**, Sequences of 3µm-thick slices from 3 individual 2-photon Z-stacks from CD11c.YFP mice (mouse 1, top row; mouse 2, bottom two left panels; mouse 3, bottom two right panels). Relative depths (µm) within Z-stacks indicated. Arrows point to close interactions between cells. **d**, Analysis of gDT-II cell motility from intravital imaging of the ipsilateral flank of melanoma-challenged mice (TME) or the contralateral flank of HSV-1-challenged mice (HSV) d7-9 p.i. Speed, confinement ratio, and percentage of time in arrest of total gDT-II. Data pooled from 2 experiments with 4 mice (TME) or one experiment with two mice (HSV) with 163 (TME) or 606 (HSV) gDT-II. Statistics by two-sided Mann–Whitney test. Red lines depict means. **e**+**f,** Expression of *Tbx21* in CD4$^+$ T cells across different anatomical locations from single-cell RNA sequencing experiments described in Fig.2. **e,** Normalised log2 expression of *Tbx21* superimposed on UMAP. **f**, Relative gene expression levels (Z-score) and percentage of cells (shown by dot size) expressing *Tbx21*. **g**+**h,** Flow cytometric analysis of T-bet expression in gDT-II from WT mice that were i.v. transferred 1×10$^4$ naïve gDT-II prior to e.c. inoculation with B16.gD. gDT-II analysed 8d p.i. from ipsilateral brachial LN (bLN), spleen and inoculation site skin (skin). **g,** Representative flow cytometry plots and **h,** pooled analysis showing proportion of gDT-II expressing T-bet. Gates defined using gDT-II.*Tbx21*$^{-/-}$ from respective organs. Data pooled from 4 independent experiments with 8 mice. Statistics by Kruskal-Wallis test with Dunn's test for multiple comparisons. Bars depict means. **i-o**, Spatial analysis of multiplex fluorescent IHC of 25-28 human primary cutaneous melanoma samples. **i+j,** Representative image (**i**) and quantification (**j**) of the association of APCs (HLA–DR$^+$SOX10$^-$CD3$^-$) with CD3$^+$CD8$^-$T cells (corresponding to CD4$^+$ T cells) (n=25). **k+l,** Representative image (**k**) and quantification (**l**) of the association of APCs (HLA-DR$^+$SOX10$^-$CD3$^-$) with both CD3$^+$CD8$^-$ and CD3$^+$CD8$^+$ T cells (n=25). **m-o,** Representative image (**m**) and quantification (**n**) of HLA-DR expression by melanoma (SOX10$^+$) cells (n=28), and quantification (**o**) of the association of HLA-DR$^+$SOX10$^+$ melanoma cells with CD3$^+$CD8$^-$ T cells (n=25). White arrows or dashed circle in imagers indicate the respective cell-cell associations. Red lines depict means (**j,l,n,o**).

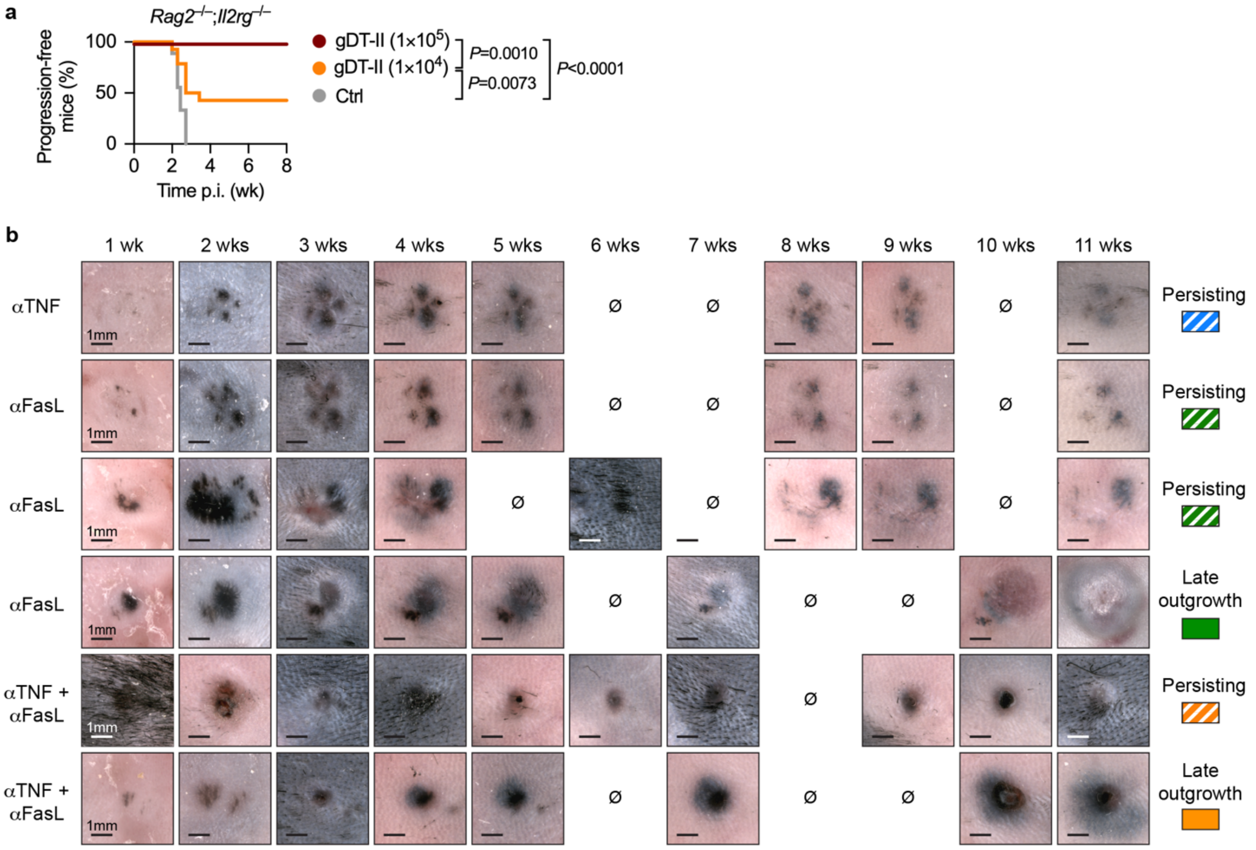

**Figure S8. Mechanisms of gDT-II protection from melanoma challenge. a,** Proportion of *Rag2*$^{-/-}$;*Il2rg*$^{-/-}$ tumour-free mice or mice with tumours <20mm$^3$ following e.c. inoculation with B16.gD and transfer of 1×10$^4$ (orange) or 1×10$^5$ (red) activated gDT-II 1 wk p.i., or mice that did not receive gDT-II (Ctrl). Statistics by Log-rank Mantel–Cox test. **b**, Representative dermoscopic photographs taken longitudinally (wks p.i.) depicting persisting lesions or tumours that exhibit late outgrowth from *Rag2*$^{-/-}$;*Il2rg*$^{-/-}$ mice e.c. inoculated with B16.gD, i.v. transferred 5×10$^4$ activated gDT-II 1wk p.i. and injected with blocking anti-TNFα and/or anti-FasL Abs, as indicated. Scale bar, 1mm.

| **Name** | **Conjugate** | **Clone** | **Source** | **Cat. Number** | **Dilution** |
|---|---|---|---|---|---|
| CD103 | BV510 | M290 | BD Horizon™ | 563087 | 1:200 |
| CD103 | PerCP-Cy5.5 | 2 E7 | BioLegend | 121416 | 1:200 |
| CD11b | BUV496 | M1/70 | BD Optibuild | 749864 | 1:400 |
| CD11b | BV711 | M1/70 | BioLegend | 101242 | 1:300 |
| CD11c | BV650 | N418 | Biolegend | 117339 | 1:200 |
| CD11c | PE-Cy7 | N418 | eBioscience™ | 25-0114-82 | 1:200 |
| CD19 | BV605 | 6D5 | BioLegend | 115540 | 1:200 - 1:400 |
| CD127 | APC | A7R34 | eBioscience™ | 17-1271-82 | 1:200 |
| CD25 | BV605 | PC61 | BD Horizon™ | 563061 | 1:300 |
| CD3e | APC | 17A2 | eBioscience™ | 17-0032-82 | 1:200 |
| CD3e | BUV395 | 145-2C11 | BD Horizon™ | 563565 | 1:200 |
| CD3e | BV711 | 17A2 | BioLegend | 100241 | 1:200 |
| CD4 | BUV805 | GK1.5 | BD Horizon™ | 612900 | 1:200 |
| CD4 | PeCy5 | RM4-5 | BD Pharmingen | 553050 | 1:2400 |
| CD4 | BUV563 | H129.19 | BD Horizon | 741255 | 1:400 |
| CD4 | BV786 | RM4-5 | BD Horizon™ | 563727 | 1:200 |
| CD44 | PerCP-Cy5.5 | IM7 | eBioscience™ | 45-0441-82 | 1:200 |
| CD45.1 | FITC | A20 | BD Pharmingen™ | 553775 | 1:100 |
| CD45.1 | BV785 | A20 | BioLegend | 110743 | 1:100 |
| CD45.1 | BUV395 | A20 | BD Horizon™ | 565212 | 1:100 |
| CD45.1 | BV605 | A20 | BioLegend | 110737 | 1:100 |
| CD45.2 | BUV737 | 104 | BD Horizon™ | 612778 | 1:100 |
| CD45.2 | BUV395 | 104 | BD Horizon | 564616 | 1:100 |
| CD45.2 | BV786 | 104 | BD Horizon™ | 563686 | 1:100 |
| CD62L | PE-Cy7 | MEL-14 | eBioscience™ | 25-0621-82 | 1:200 |
| CD62L | BV605 | MEL-15 | BD Horizon™ | 563252 | 1:200 |
| CD64 | PE | X54-5/7.1 | BioLegend | 139304 | 1:300 |
| CD69 | BV421 | H1.2F3 | BioLegend | 104528 | 1:200 |
| CD8 | BV711 | 53-6.7 | BioLegend | 100748 | 1:200 |
| CD8 | APC | 53-6.7 | eBioscience™ | 17-0081-82 | 1:200 |
| CD80 | Percp710 | 16-10A1 | eBioscience™ | 46-0801-82 | 1:200 |
| CD83 | BUV395 | Michel-19 | BD OptiBuild™ | 740323 | 1:200 |
| CD86 | BV510 | GL1 | BD Horizon™ | 563077 | 1:200 |
| F4/80 | BUV805 | T45-2342 | BD Optibuild | 749282 | 1:200 |
| FoxP3 | eFluor 450 | FJK-16s | eBioscience™ | 48-5773-82 | 1:200 |
| IFNg | PE-Cy7 | XMG1.2 | BD Pharmingen™ | 557649 | 1:200 |
| iNOS | APC | CXNFT | eBioscience™ | 17-5920-82 | 1:100 |
| Ly6C | APC-eFluor 780 | HK1.4 | eBioscience™ | 47-5932-82 | 1: 300 - 1:400 |
| Ly6G | PE | 1A8-Ly6g | eBioscience™ | 12-9668-82 | 1:300 |
| MHC II (I-A/I-E) | Alexa Fluor (AF) 700 | M5/114.15.2 | eBioscience™ | 56-5321-82 | 1:300 |
| MHC II (I-A/I-E) | APC | M5/114.15.2 | eBioscience™ | 17-5321-82 | 1:300 |
| MHC I (H2-Kb) | PE | AF6-88.5 | eBioscience™ | 12-5958-82 | 1:200 |
| PD-1 | PE-Cy7 | J43 | eBioscience™ | 25-9985-82 | 1:200 |
| PD-L1 | PE | 10F.9G2 | BioLegend | 124308 | 1:400 |
| PD-L2 | APC | TY25 | Biolegend | 107210 | 1:200 |
| SIRPa | APC | P84 | eBioscience™ | 17-1721-82 | 1:200 |
| T-bet | BV786 | O4-46 | BD Horizon™ | 564141 | 1:100 |

| | | | | | |
|---|---|---|---|---|---|
| TNF | APC | MP6-XT22 | BD Pharmingen™ | 554420 | 1:200 - 1:400 |
| Va3.2 | PE | RR3-16 | BioLegend | 135406 | 1:200 |
| XCR1 | BV510 | ZET | Biolegend | 148218 | 1:200 |
| CD16/CD32 | Unconjugated | 2.4G2 | BD Biosciences | 553142 | 1:200 |

**Supplementary Table S1. List of anti-mouse antibodies**

| **Order** | **Antibody** | **Source** | **Clone** | **Manufacturer** | **Dilution** | **Diluent** | **AR pH** | **Detection Kit** | **Opal** |
|---|---|---|---|---|---|---|---|---|---|
| **1** | FXIIIA | Sheep | polyclonal | Affinity Biologicals | 1:5000 | Antibody Diluent/Block (Akoya Biosciences) | 9 | Donkey anti-Sheep IgG Secondary Antibody HRP (Thermo Fisher Scientific) | 520 |
| **2** | CD11c | Mouse | Leu-M5 | Biocare Medical | 1:1000 | Antibody Diluent/Block | 9 | Opal Polymer HRP Ms + Rb | 650 |
| **3** | CD20 | Mouse | L26 | Biocare Medical | 1:250 | Da Vinci Green | 9 | Opal Polymer HRP Ms + Rb | 570 |
| **4** | CD68 | Mouse | KP-1 | Cell Marque | 1:2000 | Antibody Diluent/Block | 9 | Opal Polymer HRP Ms + Rb | 620 |
| **5** | SOX10 | Mouse | BC34 | Biocare Medical | 1:300 | Renoir Red | 9 | Opal Polymer HRP Ms + Rb | 690 |
| **6** | CD4 | Mouse | 4B12 | Biocare Medical | 1:500 | Renaissance Background Reducing Diluent (Biocare Medical) | 9 | Opal Polymer HRP Ms + Rb | 540 |

**Supplementary Table S2: Detailed mIHC staining conditions for T cells in AMGP melanoma.**

| **Order** | **Antibody** | **Source** | **Clone** | **Manufacturer** | **Dilution** | **Diluent** | **AR pH** | **Detection Kit** | **Opal** |
|---|---|---|---|---|---|---|---|---|---|
| **1** | CD103 | Rabbit | EP206 | Biocare Medical | 1:100 | Da Vinci Green (Biocare Medical) | 9 | Mach 4 Universal HRP-Polymer (Biocare Medical) | 520 |
| **2** | FoxP3 | Mouse | 236A1E7 | Abcam | 1:6000 | Da Vinci Green | 9 | Mach 3 Mouse HRP-polymer (Biocare Medical) | 540 |
| **3** | CD8 | Rabbit | SP-16 | Cell Marque | 1:200 | Da Vinci Green | 9 | Opal Polymer HRP Ms + Rb (Akoya Biosciences) | 570 |
| **4** | CD3 | Rabbit | MRQ-39 | Cell Marque | 1:2000 | Da Vinci Green | 9 | Opal Polymer HRP Ms + Rb | 620 |
| **5** | HLA-DR | Mouse | TAL-1B5 | Abcam | 1:60000 | Da Vinci Green | 9 | Opal Polymer HRP Ms + Rb | 650 |
| **6** | SOX10 | Mouse | BC34 | Biocare Medical | 1:200 | Renoir Red (Biocare Medical) | 9 | Opal Polymer HRP Ms + Rb | 690 |

**Supplementary Table 3: Detailed mIHC staining conditions for T cells in primary melanoma.**

**Supplementary Movie 1.** 2-photon microscopy of the skin inoculation site of a B6.albino mouse 7d p.i. Image rotated to show localisation of gDT-II.GFP (green) around B16.gD.*Tyr*$^{\mathrm{KO}}$.mCherry (red). SHG signal, white; autofluorescent hair, yellow/green. Data representative of 5 independent experiments with 11 B6.albino mice that were i.v. transferred 1–5×10$^{4}$ naive gDT-II.GFP 1d prior to e.c. inoculation with B16.gD.*Tyr*$^{\mathrm{KO}}$.mCherry and imaged 7–9d p.i.

**Supplementary Movie 2.** 2-photon microscopy of the skin inoculation site of a B6.albino mouse 8d p.i., depicting gDT-II.GFP (green) and partly destroyed and scattered B16.gD.*Tyr*$^{\mathrm{KO}}$.mCherry (red). SHG signal, white. Data representative of 5 independent experiments with 11 B6.albino mice that were i.v. transferred 1–5×10$^{4}$ naive gDT-II.GFP 1d prior to e.c. inoculation with B16.gD.*Tyr*$^{\mathrm{KO}}$.mCherry and imaged 7–9d p.i.

**Supplementary Movie 3.** 2-photon microscopy of the skin inoculation site of a B6.albino mouse 8d p.i. depicting surveillance of B16.gD.*Tyr*$^{\mathrm{KO}}$.mCherry (red) by gDT-II.GFP (green). SHG signal (white) removed as movie zooms in on gDT-II.GFP. Autofluorescent hair, yellow/green. Data representative of 5 independent experiments with 11 B6.albino mice that were i.v. transferred 1–5×10$^{4}$ naive gDT-II.GFP 1d prior to e.c. inoculation with B16.gD.*Tyr*$^{\mathrm{KO}}$.mCherry and imaged 7–9d p.i.

**Supplementary Movie 4.** 2-photon microscopy of the skin inoculation site of an *I-Ab*$^{-/-}$ mouse 11d p.i., depicting gDT-II.CFP (cyan) that appear spherical and are moving slow/arrested within B16.gD.*Tyr*$^{\mathrm{KO}}$.mCherry (red). SHG signal, white; autofluorescent hair, cyan/white. Representative of 2 independent experiments with 7 *I-Ab*$^{-/-}$ mice that were e.c. inoculated with B16.gD.*Tyr*$^{\mathrm{KO}}$.mCherry, i.d. transferred activated gDT-II.GFP or gDT-II.CFP (4×10$^{6}$) 4d p.i. and imaged 11–18d p.i.

**Supplementary Movie 5.** 2-photon microscopy of the skin inoculation site of an *I-Ab*$^{-/-}$ mouse 11d p.i., depicting gDT-II.CFP (cyan) that are fast-moving within a mass of B16.gD.*Tyr*$^{\mathrm{KO}}$.mCherry (red). SHG signal, white; autofluorescent hair, cyan. Representative of 2 independent experiments with 7 *I-Ab*$^{-/-}$ mice e.c. that were inoculated with B16.gD.*Tyr*$^{\mathrm{KO}}$.mCherry, i.d. transferred activated gDT-II.GFP or gDT-II.CFP (4 × 10$^{6}$) 4d p.i. and imaged 11–18d p.i.

**Supplementary Movie 6.** 2-photon microscopy of the skin inoculation site of an *I-Ab*$^{-/-}$ mouse 17d p.i., depicting gDT-II.GFP (green) that appear spherical and are moving slow/arrested within a mass of B16.gD.*Tyr*$^{\mathrm{KO}}$.mCherry (red). SHG signal, white; autofluorescent hair, yellow/green. Representative of 2 independent experiments with 7 *I-Ab*$^{-/-}$ mice that were e.c. inoculated with B16.gD.*Tyr*$^{\mathrm{KO}}$.mCherry, i.d. transferred activated gDT-II.GFP or gDT-II.CFP (4×10$^{6}$) 4d p.i. and imaged 11–18d p.i.

**Supplementary Movie 7.** 2-photon microscopy of the skin inoculation site of an *I-Ab*$^{-/-}$ mouse 12d p.i. depicting gDT-II.GFP (green) that are fast-moving within a mass of B16.gD.*Tyr*$^{\mathrm{KO}}$.mCherry (red). SHG signal, white; autofluorescent hair, yellow/green. Representative of 2 independent experiments with 7 *I-Ab*$^{-/-}$ mice that were e.c. inoculated with B16.gD.*Tyr*$^{\mathrm{KO}}$.mCherry, i.d. transferred activated gDT-II.GFP or gDT-II.CFP (4×10$^{6}$) 4d p.i. and imaged 11–18d p.i.

**Supplementary Movie 8.** 2-photon microscopy of the skin inoculation site of a CD11c.YFP mouse 8d p.i. depicting gDT-II.CFP (cyan), CD11c.YFP (yellow) and B16.gD.*Tyr*$^{KO}$.mCherry (red). SHG signal, white; autofluorescent hair, cyan. Representative of 4 independent experiments with 15 mice (CD11c.YFP or CD11c.YFP→B6.albino bone-marrow chimeric mice) that were i.v. transferred naïve gDT-II.CFP ($1\times10^4$) 1d prior to e.c. inoculation with B16.gD.*Tyr*$^{KO}$.mCherry and imaged 7–10d p.i.

**Supplementary Movie 9.** 2-photon microscopy of the skin inoculation site of a CD11c.YFP→B6.albino bone-marrow chimeric mouse 9d p.i. depicting gDT-II.CFP (cyan), CD11c.YFP (yellow) and B16.gD.*Tyr*$^{KO}$.mCherry (red). SHG signal, white; autofluorescent hair, cyan/white. Representative of 4 independent experiments with 15 mice (CD11c.YFP or CD11c.YFP→B6.albino bone-marrow chimeric) that were i.v. transferred naïve gDT-II.CFP ($1\times10^4$) 1d prior to e.c. inoculation with B16.gD.*Tyr*$^{KO}$.mCherry and imaged 7–10d p.i.

**Supplementary Movie 10.** 2-photon microscopy of the skin inoculation site of a CD11c.YFP→B6.albino bone marrow chimeric mouse 8d p.i., depicting gDT-II.CFP (cyan), CD11c.YFP (yellow) and B16.gD.*Tyr*$^{KO}$.mCherry (red). SHG signal, white; autofluorescent hair, cyan. Representative of 4 independent experiments with 15 mice (CD11c.YFP or CD11c.YFP→ B6.albino bone marrow chimeric) that were i.v. transferred naïve gDT-II.CFP ($1\times10^4$) 1d prior to e.c. inoculation B16.gD.*Tyr*$^{KO}$.mCherry and imaged 7–10d p.i.

**Supplementary Movie 11.** 2-photon microscopy of the skin from the contralateral flank of a CD11c.YFP mouse 8d after infection with HSV-1, depicting gDT-II.CFP (cyan) and CD11c.YFP (yellow). SHG signal, white; autofluorescent hair in white/cyan. Representative of 5 mice from one experiment imaged 7–8d post-HSV.

**Supplementary Movie 12.** 2-photon microscopy of the skin inoculation site of an albino *Rag2*$^{-/-}$;*Il2rg*$^{-/-}$ mouse 15d p.i. depicting gDT-II.GFP (green) and B16.gD.*Tyr*$^{KO}$.mCherry (red). SHG signal, white. Representative of 2 independent experiments with 7 albino *Rag2*$^{-/-}$;*Il2rg*$^{-/-}$ mice that were e.c. inoculated with B16.gD.*Tyr*$^{KO}$.mCherry, i.v. transferred activated gDT-II.GFP or gDT-II.CFP ($5\times10^4$) 7d p.i. and imaged 14–17d p.i.